Mon. Not. R. Astron. Soc. **000**, 1–?? (2015) Printed 9 February 2016 (MN LATEX style file v2.2)

The ESO UVES Advanced Data Products Quasar Sample – VI. Sub-Damped Lyman-α Metallicity Measurements and the Circum-Galactic Medium*

S. Quiret[1]†, C. Péroux[1], T. Zafar[2], V. P. Kulkarni[3], E. B. Jenkins[4], B. Milliard[1], H. Rahmani[1], A. Popping[5], S. M. Rao[6], D. A. Turnshek[6] and E. M. Monier[7]

[1] *Aix Marseille Université, CNRS, LAM (Laboratoire d'Astrophysique de Marseille) UMR 7326, 13388, Marseille, France*
[2] *European Southern Observatory, Karl-Schwarschild-Strasse 2, 85748, Garching, Germany*
[3] *University of South Carolina, Dept. of Physics & Astronomy, Columbia, USA*
[4] *Princeton University Observatory, Princeton, NJ 08544-1001, USA*
[5] *International Centre for Radio Astronomy Research (ICRAR), The University of Western Australia, 35 Stirling Hwy, 6009 Crawley WA, Australia*
[6] *Department of Physics and Astronomy and PITTsburgh Particle physics, Astrophysics, and Cosmology Center (PITT PACC), University of Pittsburgh, Pittsburgh, PA 15260, USA*
[7] *Department of Physics, The College at Brockport, State University of New York, Brockport, NY 14420, USA*

arXiv:1602.02564v1 [astro-ph.GA] 8 Feb 2016

9 February 2016

ABSTRACT

The Circum-Galactic Medium (CGM) can be probed through the analysis of absorbing systems in the line-of-sight to bright background quasars. We present measurements of the metallicity of a new sample of 15 sub-damped Lyman-α absorbers (sub-DLAs, defined as absorbers with $19.0 < \log \mathrm{N(H\,I)} < 20.3$) with redshift $0.584 \leqslant \mathrm{z_{abs}} \leqslant 3.104$ from the ESO Ultra-Violet Echelle Spectrograph (UVES) Advanced Data Products Quasar Sample (EUADP). We combine these results with other measurements from the literature to produce a compilation of metallicity measurements for 92 sub-DLAs as well as a sample of 362 DLAs. We apply a multi-element analysis to quantify the amount of dust in these two classes of systems. We find that either the element depletion patterns in these systems differ from the Galactic depletion patterns or they have a different nucleosynthetic history than our own Galaxy. We propose a new method to derive the velocity width of absorption profiles, using the modeled Voigt profile features. The correlation between the velocity width $\Delta \mathrm{V_{90}}$ of the absorption profile and the metallicity is found to be tighter for DLAs than for sub-DLAs. We report hints of a bimodal distribution in the [Fe/H] metallicity of low redshift ($\mathrm{z} < 1.25$) sub-DLAs, which is unseen at higher redshifts. This feature can be interpreted as a signature from the metal-poor, accreting gas and the metal-rich, outflowing gas, both being traced by sub-DLAs at low redshifts.

Key words: Galaxies: formation – galaxies: evolution – galaxies: abundances – galaxies: ISM – quasars: absorption lines – intergalactic medium

1 INTRODUCTION

In depth studies of galaxy evolution require an understanding of the complex processes occurring at the interface of the galaxy and its nearby environment, the Circum-Galactic Medium (CGM).

On the one hand, the star formation process is believed to be fed in galaxies via accretion mechanisms (Rees & Ostriker 1977; White & Rees 1978; Prochaska & Wolfe 2009; Bauermeister, Blitz & Ma 2010). For galaxies with masses typically below $\sim 10^{11-12}\mathrm{M_\odot}$, the accreting gas follows cold flows ($\mathrm{T} \sim 10^{4-5}\mathrm{K}$) while for more massive galaxies, a second mode of accretion appears, the "hot mode", where the

* Includes observations collected during programme ESO 91.A-0300 at the European Southern Observatory (ESO) Very Large Telescope (VLT) with UVES on the 8.2 m telescopes operated at the Paranal Observatory, Chile.
† E-mail: samuel.quiret@lam.fr

© 2015 RAS

gas is shock heated near the virial temperature ($T \sim 10^6$K) (Rees & Ostriker 1977; Silk 1977; White & Rees 1978; Birnboim & Dekel 2003; Kereš et al. 2005; Dekel & Birnboim 2006; Ocvirk, Pichon & Teyssier 2008). Simulations show that about 40% of the accretion may be genuinely smooth (Genel et al. 2010). These modes also differ in metallicity (Fumagalli et al. 2011; Shen et al. 2013). Indeed, Ocvirk, Pichon & Teyssier (2008) showed that the "cold mode" accreting gas can reach metallicities up to tenth solar, while the hot mode accreting gas metallicities are usually lower and are highly dependent on the distance to the center of the galaxy and on how well the gas is mixed. These accreting streams may also provide the galaxy with additional angular momentum (Fall & Efstathiou 1980). Observational evidences for accretion have been challenging to gather due to the low surface brightness and low filling factor of the infalling gas and its expected low metallicity. Nevertheless, cold accretion has been recently detected in a few objects (Steidel et al. 2000; Martin et al. 2012; Rubin et al. 2012; Bouché et al. 2013). Similarly, early evidences for cold accretion onto quasars have been recently reported by Cantalupo et al. (2014) and Martin et al. (2014).

On the other hand, galaxies release energy and material in their environment (up to $\sim$ 125kpc) via supernovae (SNe), stellar winds or Active Galactic Nuclei (AGN) activity. These outflows tend to chemically enriched the IGM (Songaila & Cowie 1996; Simcoe, Sargent & Rauch 2004; Adelberger et al. 2005; Ryan-Weber et al. 2009; D'Odorico et al. 2013; Shull, Danforth & Tilton 2014; Shull et al. 2015), and can regulate the star formation process of galaxies. Indeed, as the gas is released, it will starve the galaxy from fresh gas accreting along the galaxy major axis, quenching the star formation. It will also enhanced the star formation by cooling the gas via metal line emissions. Fountains can also be created if the gas does not leave the potential well of the galaxy. In this scenario, the fully metal enriched gas recycles and falls back onto the galactic disk and contribute directly to the star forming processes as it can cool efficiently. Simulations have shown that fountains dominate the global accretion mechanism for $z \lesssim 1$ galaxies (Oppenheimer et al. 2010). Even though outflows are ubiquitous at all redshifts around star forming galaxies (Shapley et al. 2003; Martin 2005; Rubin et al. 2014) and their existence is confirmed by signatures of OVI found within the CGM of low redshift star forming galaxies (Tumlinson et al. 2011), they remain poorly understood in the context of galaxy formation models.

In the context of emission line study, Bertone et al. (2010a,b) argued that the ionization state of elements provides valuable insight on the physical state of the CGM (mainly its temperature but also its ionizing process) and can be used to study the different feedback processes taking place, including metal pollution of accreting gas via galactic fountains. Fumagalli et al. (2011) also argued that kinematic analysis of absorption lines can be used in addition to the metallicity analysis to distinguish metal-rich outflowing material from metal-poor ($\lesssim 0.01 Z_\odot$) accreting gas. Therefore, the study of metal lines (kinematics, line strengths, ionization states) might be the key diagnostic to observationally disentangle outflows from inflows and assess the level of metal enrichment of the CGM and thus galaxy evolution.

Absorbers observed in background quasar spectra are a tool to probe the low density gas and its metallicity. Indeed, simulations predict that cold accretion onto galaxies can be observed in absorption via dense H I absorbing systems with $\log N(H\,I) > 15.5$ (Faucher-Giguere & Kereš 2011; van de Voort et al. 2012; Shen et al. 2013). They predict that the cold streams could be traced with metal-poor H I absorption systems, mostly in the Lyman Limit System (LLS) range $17.2 \leqslant \log N(H\,I) < 19.0$. Recently, Lehner et al. (2013) showed observational evidence for low redshift LLS presenting a bimodal metallicity distribution, which they associated with infalls and outflows. However, the metallicities of LLS depend sensitively on model-dependent ionization corrections, since the LLS gas is highly ionized. This makes it harder to reliably detect the difference between inflows and outflows using the LLS. A more robust way of detecting the metallicity distribution of the gas around galaxies is by using the damped Lyman-α (DLA; $\log N(H\,I) \geqslant 20.3$) and sub-damped Lyman-$\alpha$ (sub-DLA; $19.0 \leqslant \log N(H\,I) < 20.3$) absorbers. These systems are the primary neutral gas reservoir at $0 < z < 5$ (Storrie-Lombardi & Wolfe 2000; Péroux et al. 2005; Prochaska, HerbertFort & Wolfe 2005; Rao, Turnshek & Nestor 2006; Zafar et al. 2013) and offer the most precise element abundance measurements in distant galaxies. In particular, at $z \leqslant 2$, Fumagalli et al. (2011) anticipate that almost half of the cross-section in the sub-DLA H I column density range is due to streams, while at $z \sim 3$, van de Voort et al. (2012) anticipate that it is more than 80%.

In an era of large quasar surveys, with samples of thousands of DLAs available (e.g., Noterdaeme et al. 2012c), sub-DLAs remain little studied. Indeed, at low H I column densities, one requires a high spectral resolution and high signal to noise ratio (SNR) to derive element abundances. The large quasar samples observed with the high resolution spectrographs VLT/UVES (Zafar, Popping & Péroux 2013) and Keck/HIRES (O'Meara et al. 2015) are therefore crucial tools for our understanding of sub-DLA properties. Here, we present a detailed study of the metallicity and kinematics of a large sample of DLAs and sub-DLAs observed at high resolution with UVES.

The paper is organised as follows. In §2 we present the data sample and in §3 we describe the abundance measurements. The results are discussed in §4 followed by conclusions in §5.

2 THE DATA

2.1 New absorbers

In order to put together a significant sample of sub-DLAs observed at high spectral resolution, we make use of the ESO UVES Advanced Data Products (EUADP) sample from Zafar, Popping & Péroux (2013). This sample consists of 250 high-resolution ($R \sim 42,000$) quasars spectra covering a total of 196 damped absorbers (with $\log N(H\,I) > 19.0$).

This dataset has motivated a number of studies including a report of new H I systems (Zafar, Popping & Péroux 2013) and how they can be used to constrained the neutral gas mass density of sub-DLAs in particular (Zafar et al. 2013), the nucleosynthetic history of Nitrogen (Zafar et al. 2014a) and the low Argon abundances observed in DLAs (Zafar et al. 2014b).

Most of the absorbers in the EUADP sample have their metallicity abundances published in the literature (Péroux et al. 2006a,b, 2008; Zafar et al. 2013, and reference therein). We present here the analysis of 14 new EUADP sub-DLAs covering a redshift range $0.584 \leqslant z_{abs} \leqslant 3.104$. We also include 6 new DLAs for completeness. The measurements of HI column densities and redshifts of each system in the EUADP sample are reported in Zafar, Popping & Péroux (2013) and references therein.

In addition to these 14 new sub-DLAs from the EUADP sample, we present the UVES spectra of two other systems: one sub-DLA at $z_{abs} = 0.584$ and one DLA at $z_{abs} = 0.647$. These two low-redshift absorbers have been observed with the HST ACS grism from which an estimate of their H I column densities has been derived (Turnshek et al. 2015). The quasars were subsequently observed with UVES on VLT under the programme 91.A-0300 (PI: C. Péroux) in Service Mode in August and September 2013. Each object was observed using a combined 346+564 nm setting with two different observations with exposure times lasting $4500 + 3600$ sec (QSO J0018−0913) and 2 x 4500 sec (QSO J0132−0823). The data were reduced using the most recent version of the UVES pipeline in MIDAS (uves/5.4.3). Master bias and flat images were constructed using calibration frames taken closest in time to the science frames. The science frames were extracted with the "optimal" option and corrected to the vacuum heliocentric reference. To combine the resulting spectra, we choose to weight them by the signal-to-noise ratio, as for the remaining of the EUADP sample (Zafar, Popping & Péroux 2013), in line with standard practice at this spectral resolution (O'Meara et al. 2015).

The absorption redshifts, which are based on the N(H I) or MgII features, are used to analyse the associated metal lines. Table 1 summarises the properties of the quasars and absorbers in the sample studied here. The two additional objects which were not originally published by Zafar, Popping & Péroux (2013) are shown in bold.

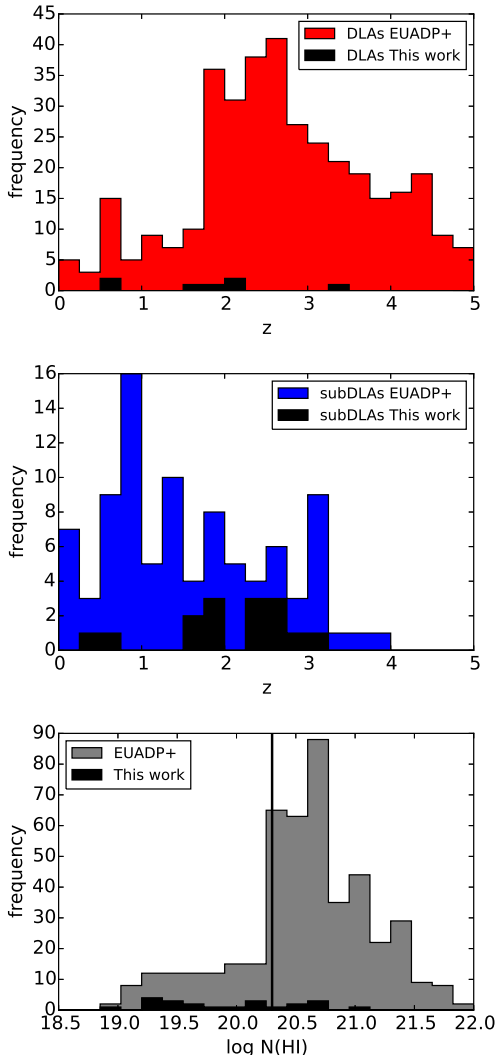

Figure 1. Absorption redshifts and N(H I) distributions of the DLAs and sub-DLAs in our sample compared with the remaining absorbers covered by the EUADP survey and the literature (referred to as EUADP+ sample). The vertical line in the bottom panel indicates the canonical DLA definition. Clearly, the data presented here contribute most in the sub-DLA H I column density range at low redshift where few systems have been studied so far.

2.2 Literature sample

In addition to these 15 new sub-DLA measurements (+7 DLAs), we gather metallicity estimates of sub-DLAs from the remaining part of the EUADP sample as well as other recently published samples (Meiring et al. 2006, 2009a; Dessauges-Zavadsky, Ellison & Murphy 2009; Battisti et al. 2012; Som et al. 2015). In order to compare the properties of sub-DLAs to that of DLAs, we add to the sample a collection of DLA metallicity measurements from the EUADP sample as well as from the literature (see earlier references and Berg et al. 2015a). Altogether, this literature sample is the largest and most up-to-date sub-DLA sample published today.

The table in Appendix B lists the metallicity estimates of the full sample of absorbers and associated references. Fig. 1 illustrates the distribution in redshift of the absorber sample studied for both DLAs and sub-DLAs (top and middle panels respectively). The bottom panel presents the N(H I) distribution of the sample. We stress that the additional systems are consistent with the parent sample as they are not selected on their metal content or redshift but solely on their H I column density (see also Fig. 5).

In conclusion, the final sample, referred to as the EUADP+ sample, contains 92 sub-DLAs (with 15 new measurements) and 362 DLAs (7 new measurements). Clearly, the data presented here contribute most in the sub-DLA H I column density range.

3 ANALYSIS

3.1 Method

The continua of the quasar spectra are fitted using a spline function connecting the regions of the spectrum free from absorption features as described in Zafar et al. (2013). The Voigt profile fits are performed with the FIT/LYMAN package within the MIDAS environment (Fontana & Ballester 1995). The routine calculates a χ^2 Hessian minimization and

Table 1. Properties of the 22 quasar absorbers (15 subDLAs and 7 DLAs) studied here. The majority of these absorbers are from the EUADP sample (Zafar, Popping & Péroux 2013), but for the two systems shown in bold which have been observed recently with VLT/UVES by our group (see text for details).

QSO name	coordinates	z_{em}	z_{abs}	log(N(H I))	wavelength coverage (Å)
QSO J0008-2900	2.219-29.012	2.645	2.254	20.22 ± 0.10	3300-4970,5730-10420
QSO J0008-2901	2.24-29.024	2.607	2.491	19.94 ± 0.11	3300-4970,5730-10420
QSO J0018-0913	4.730-9.231	0.756	0.584	20.11 ± 0.10	3065-3875,4620-5602,5675-6650
QSO J0041-4936	10.381-49.603	3.24	2.248	20.46 ± 0.13	3290-4520,4620-5600,5675-6650
QSO B0128-2150	22.773-21.58	1.9	1.857	20.21 ± 0.09	3045-3868,4785-5755,5830-6810
QSO J0132-0823	23.041-8.397	1.121	0.647	20.60 ± 0.12	3065-3875,4620-5602,5675-6650
QSO B0307-195B	47.538-19.369	2.122	1.788	19.00 ± 0.10	3065-5758,5835-8520,8660-10420
QSO J0427-1302	66.78-13.048	2.166	1.562	19.35 ± 0.10	3285-4515,4780-5760,5835-6810
PKS 0454-220	74.037-21.986	0.534	0.474	19.45 ± 0.03	3050-3870,4170-5162,5230-6210
J060008.1-504036	90.033-50.677	3.13	2.149	20.40 ± 0.12	3300-4520,4620-5600,5675-6650
QSO B1036-2257	159.79-23.224	3.13	2.533	19.30 ± 0.10	3300-5758,5838-8525,8660-10420
J115538.6+053050	178.911+5.514	3.475	3.327	21.00 ± 0.10	3300-5600,5675-7500,7665-9460
LBQS 1232+0815	188.656+7.979	2.57	1.720	19.48 ± 0.13	3285-4520,4620-5600,5675-6650
QSO J1330-2522	202.717-25.372	3.91	2.654	19.56 ± 0.13	3300-4515,4780-5757,5835-6810
QSO J1356-1101	209.195-11.025	3.006	2.397	19.85 ± 0.08	3757-4985,6700-8520,8660-10420
QSO J1621-0042	245.32-0.714	3.7	3.104	19.70 ± 0.20	3300-4515,4780-5757,5835-6810
4C 12.59	247.938+11.934	1.792	0.531	20.70 ± 0.09	3060-3870,4780-5757,5835-6810
LBQS 2114-4347	319.331-43.573	2.04	1.912	19.50 ± 0.10	3050-10420
QSO B2126-15	322.3-15.645	3.268	2.638	19.25 ± 0.15	3300-5600,5675-6650,6695-8520,
...	...	...	2.769	19.20 ± 0.15	8650-10420
LBQS 2132-4321	324.025-43.138	2.42	1.916	20.74 ± 0.09	3290-4530,4620-5600,5675-6650
QSO B2318-1107	350.369-10.856	2.96	1.629	20.52 ± 0.14	3050-4515,4780-5760,5840-6810

enables fits of up to 50 free parameters including the central wavelength, the column density and the Doppler parameter of each component of the fit. This allows fitting several ions simultaneously as well as several transitions of the same species, thus making maximum use of the information available from the velocity profiles. The low-ionization species (OI, FeII, SiII, ...) are fitted as a separate group from the high-ionization species (CIV, SiIV, ...) (e.g., Wolfe, Gawiser & Prochaska 2005; Fox et al. 2007; Milutinovic et al. 2010; Crighton, Hennawi & Prochaska 2013). The intermediate-ionization species AlIII are fitted either on its own, or with the low-ionization or high-ionization species, depending on the similarity in the absorption velocity profiles.

This process allows us to identify possible blends of interloping absorbers at the positions of the features under study. In case of blending, the profiles are fitted using information on central wavelengths and Doppler parameters from other un-blended profiles, thus leading to upper limits in the column density determination. In addition, saturated transitions or components are avoided because the column density information cannot be recovered in that case. The quasar continuum solution is iteratively refined when necessary during the Voigt profile fitting process. The fits are performed minimizing the number of components. In cases where a transition is not detected, we derive a 3-σ upper limit from an estimate of the SNR of the spectra at the expected position of the line. The laboratory wavelengths and oscillator strengths used throughout the fits are taken from Morton (2003)[1].

[1] Recently, a new set of oscillator strengths for SII and ZnII lines has been derived for studies of the Inter-Stellar Medium (ISM), DLAs and sub-DLAs (Kisielius et al. 2014, 2015). A change from Morton (2003) oscillator strengths to this new study would lower [Zn/H] by about 0.1 dex.

We estimate the abundance for various elements of each absorbing system by summing the column densities of the different components found in the velocity profile described above. The metallicity [X/H] of an element X with respect to solar metallicity is derived from the following expression:

$$[\mathrm{X/H}] = \log\left(\frac{\mathrm{N(X)}}{\mathrm{N(H)}}\right) - \log(\mathrm{X/H})_{\odot} \quad (1)$$

where $(\mathrm{X/H})_{\odot}$ is the photospheric solar abundance from Asplund et al. (2009) and N(X) is the column density of element X. The column density of each element is taken to be that of the dominant ion, and ionization correction is ignored here (see section 3.2 for further discussion on this point). The error estimate on the total column density log N is calculated from the error on individual column density log N of each component through the error propagation formula:

$$\sigma_{\log(\mathrm{N(X)})} = \frac{\sqrt{\sum_{\mathrm{i}}(\mathrm{N(X)_i}\sigma_{\log(\mathrm{N(X)})_{\mathrm{i}}})^2}}{\mathrm{N(X)}} \quad (2)$$

The global uncertainty on the abundance determination is then calculated from a quadratic sum of $\sigma_{\log(\mathrm{N(X)})}$ and $\sigma_{\log(\mathrm{N(H)})}$ since the errors in the solar abundances would introduce systematic effects which can be neglected in studies of relative abundances.

The resulting Voigt profile parameters and corresponding velocity plots for the low-, intermediate- and high-ionization species as well as a detailed description of the 22 individual systems mentioned earlier are provided in Appendix C. The column densities and abundances derived for these systems are gathered in tables 2 (for total column densities) and 3 (for abundances).

For the different H I and metals column densities presented in this paper, the associated error on the abundances

are based on χ^2 minimization. The continuum placement error is not taken into account to be consistent with other measurements from the literature.

3.2 The Ionized Fraction of sub-DLAs

Given that observationally we are sensitive to the neutral gas in quasar absorbers, it is important to quantify the fraction of gas ionized in these systems. In the DLA column density range, the ionization corrections are below the typical abundance measurement errors (Vladilo et al. 2001; Dessauges-Zavadsky et al. 2003).

The situation might differ in the sub-DLA H I column density range given that the lower N(H I) might prevent complete self-shielding from the surrounding UV background. To address this issue, Dessauges-Zavadsky et al. (2003); Meiring et al. (2007, 2009a); Som et al. (2013, 2015) among others studied the ionized fraction of sub-DLAs based on photo-ionization CLOUDY modeling of individual systems. These studies show that the ionized fraction of hydrogen varies greatly within the sub-DLA H I column density range (see e.g. Fig 4 of Meiring et al. 2009a and Fig. 10 of Lehner et al. 2014). Nevertheless, while sub-DLAs might have an important fraction of their gas ionized in some cases, the ionization corrections to the measured abundances for sub-DLAs are often low. The large majority of elements require an ionization correction $\epsilon < 0.3$ dex, while it is negligible for FeII but important for ZnII (Dessauges-Zavadsky et al. 2003). Based on these past results and in order to be in line with abundance measurements from the literature reported here, we choose not to apply ionization correction to the new abundances presented. A more statistical approach is now required. To this end, Fumagalli et al. (submitted) have recently built CLOUDY model grids to establish posterior probability distribution functions for different states of the gas with a Bayesian formalism and Markov Chain Monte Carlo algorithm. While such an analysis is beyond the scope of the current paper, we plan to address these issues in further publications.

3.3 Assessing the Dust-Content of Quasar Absorbers: a Multi-Element Analysis

Refractory elements are easily incorporated onto dust (e.g. Fe, Cr, Ni), while volatile elements are less prone to locking up into dust grains (e.g. Zn, S). To estimate the level of depletion of a given line of sight, it is possible to compare the abundance of a volatile element with that of a refractive element. The quantity [Zn/Fe] is therefore an excellent tool to probe the quantity of Fe atoms locked into dust (Vladilo 1998). Indeed, Zn is thought to behave like Fe in different stages of chemical evolution, excluding the effects of dust depletion. From studies of low metallicity stars in our Galaxy, (Saito et al. 2009; Barbuy et al. 2015), [Zn/Fe] stays steady at [Zn/Fe] ~ 0 down to metallicities [Fe/H] $= -3$ and then increases for lower values of [Fe/H]. Hence, [Zn/H] provides a robust metallicity indicator. Unfortunately, its low cosmic abundance and long rest-frame wavelengths make it challenging to measure in sub-DLAs, preventing from a robust dust-metallicity derivation.

Here, we propose a different approach for the study of dust depletion based on the multi-element analysis proposed by Jenkins (2009) to assess the level of dust in a given line of sight. Jenkins (2009) proposed to use the abundances of different elements (namely C, N, O, Mg, Si, P, Cl, Ti, Cr, Mn, Fe, Ni, Cu, Zn, Ge, Kr and S) to compare the dust depletion of dense neutral hydrogen systems to that of the Interstellar Medium (ISM) of our Galaxy. Using a sample of 243 sight lines in our Galaxy, he established a connection between the line of sight depletion factor F_* and the different elements' abundances of each sight line. We refer the reader to Appendix A1 for a mathematical description of the method.

Fig. 2 shows the fit for the line of sight depletion factor F_* (slope) for both populations of quasar absorbers from the EUADP+ sample. For each element, we plot in cyan the median of the detections if there is at least 4 systems measured. The vertical error bars represent the error on the median using a bootstrap technique with a confidence level of 95%.

We are confronted with a large number of non-detections, creating a bias in the sample towards metal-rich systems. A large fraction of these upper (resp. lower) limits falls below (resp. above) the associated median. To address this issue, a survival analysis is considered. A Buckley-James linear regression, from the stsdas.statistics package in IRAF, results in $F_* = -0.34 \pm 0.19$ for sub-DLAs and $F_* = -0.70 \pm 0.06$ for DLAs.

On the one hand, both populations show negative values for F_*, suggesting that sub-DLAs and DLAs arise in galaxies with a lower dust content than the Milky Way. On the other hand, the derived F_* values for both populations are different at the 1.8 σ level. The sub-DLA population is consistent with the Halo like ISM from our Galaxy[2] while the DLAs are described by an F_* value well below the ones measured in the Milky Way. This is counter intuitive as we expect DLAs to be self-shielded from the UV background towards the center of the galaxy. Indeed, numerous cosmological simulations predict DLAs to be closer to the center of the galaxy than sub-DLAs (Fumagalli et al. 2011; Faucher-Giguere et al. 2015). They should therefore exhibit an F_* value corresponding to regions within the halo.

But DLAs and sub-DLAs might not be systematically associated with spiral galaxies. They might arise from a mixture of galaxy types, hence the non-physical values of F_*. In addition, the method described here is based on measurements in our Galaxy at log N(H I) > 19.5 to limit photo-ionization effects, while our quasar absorber sample goes down to log N(H I) $= 19.0$. Furthermore, the ionization levels of the sub-DLAs and DLAs in our EUADP+ sample are higher than in the Milky Way ISM, as F_* is quite different between ionized and neutral gas ($F_* = -0.1$ for the warm ionized medium and $F_* = 0.1$ for the warm neutral medium, e.g. Draine 2011). We derive F_* for log N(H I) > 19.5 sub-DLAs, and find similar results, suggesting that ionization effects do not affect the results much. Moreover, the quasar absorbers trace gas at high redshifts, which may differ from the Milky Way properties as a local galaxy. Overall, these re-

[2] $F_* = -0.28$ for *Halo* like ISM, $F_* = -0.08$ for *Disk+Halo* like ISM, $F_* = 0.12$ for *Warm Disk* like ISM and $F_* = 0.90$ for *Cool Disk* like ISM

Table 2. Total logarithmic column densities of the newly studied systems derived from the Voigt profile fits. In column N(X), (a) refers to ArI, (b) to OI, (c) to NI, (d) to TiII, (e) to CI, and (f) to CII. For PKS 0454-220, the abundances with the asterisk have been derived by Som et al. 2015.

QSO	z_{abs}	N(HI)	N(SII)	N(AlII)	N(SiII)	N(CrII)	N(MgI)	N(MgII)
QSO J0008-2900	2.254	20.22 ± 0.1	-	-	< 14.40	< 12.37	-	> 15.01
QSO J0008-2901	2.491	19.94 ± 0.11	13.68 ± 0.18	-	-	< 12.90	-	-
QSO J0018-0913	0.584	20.11 ± 0.1	-	-	-	< 12.97	< 13.04	-
QSO J0041-4936	2.248	20.46 ± 0.13	< 14.82	> 14.06	14.78 ± 0.03	13.12 ± 0.45	-	-
QSO B0128-2150	1.857	20.21 ± 0.09	14.33 ± 0.03	-	14.82 ± 0.02	-	< 13.21	-
QSO J0132-0823	0.647	20.60 ± 0.12	-	-	-	< 13.17	12.60 ± 0.04	-
QSO B0307-195B	1.788	19.00 ± 0.10	-	-	15.00 ± 0.01	< 12.77	12.54 ± 0.00	-
QSO J0427-1302	1.562	19.35 ± 0.10	-	11.78 ± 0.10	-	< 12.39	< 12.38	-
PKS 0454-220	0.474	19.45 ± 0.03	$15.06 \pm 0.04^{*}$	-	$> 14.33^{*}$	-	-	-
J060008.1-504036	2.149	20.40 ± 0.12	-	> 14.33	15.08 ± 0.01	13.10 ± 0.01	-	-
QSO B1036-2257	2.533	19.30 ± 0.1	-	12.52 ± 0.01	13.64 ± 0.01	< 12.54	-	13.57 ± 0.02
J115538.6+053050	3.327	21.00 ± 0.1	15.31 ± 0.01	-	15.93 ± 0.01	-	< 13.33	-
LBQS 1232+0815	1.720	19.48 ± 0.13	< 14.19	-	14.41 ± 0.01	< 12.38	< 12.21	-
QSO J1330-2522	2.654	19.56 ± 0.13	-	12.18 ± 0.02	-	-	-	-
QSO J1356-1101	2.397	19.85 ± 0.08	-	-	-	< 12.64	-	-
QSO J1621-0042	3.104	19.70 ± 0.2	-	-	13.78 ± 0.03	-	-	-
4C 12.59	0.531	20.70 ± 0.09	-	-	-	-	-	-
LBQS 2114-4347	1.912	19.50 ± 0.10	< 13.97	13.00 ± 0.01	14.39 ± 0.02	< 12.77	-	14.40 ± 0.01
QSO B2126-15	2.638	19.25 ± 0.15	-	-	14.67 ± 0.02	-	-	-
QSO B2126-15	2.769	19.20 ± 0.15	-	> 14.04	14.79 ± 0.01	< 12.40	-	-
LBQS 2132-4321	1.916	20.74 ± 0.09	> 14.90	-	15.55 ± 0.01	13.32 ± 0.02	-	-
QSO B2318-1107	1.629	20.52 ± 0.14	< 14.54	< 14.93	-	< 12.47	< 12.37	-

QSO	N(FeII)	N(NiII)	N(ZnII)	N(AlIII)	N(SiIV)	N(CIV)	N(MnII)	N(X)
QSO J0008-2900	13.78 ± 0.01	-	< 11.68	12.39 ± 0.04	13.72 ± 0.03	-	< 12.02	$< 13.07^{(a)}$
QSO J0008-2901	13.65 ± 0.02	< 13.29	< 12.12	< 12.20	-	-	-	$15.31 \pm 0.24^{(b)}$
QSO J0018-0913	13.87 ± 0.03	-	< 12.41	-	-	-	-	-
QSO J0041-4936	14.43 ± 0.04	13.07 ± 0.07	11.70 ± 0.10	12.90 ± 0.01	-	> 14.56	-	$14.03 \pm 0.03^{(c)}$
QSO B0128-2150	14.44 ± 0.01	13.26 ± 0.05	< 12.26	12.78 ± 0.01	-	-	-	-
QSO J0132-0823	14.96 ± 0.07	-	-	-	-	-	-	$12.39 \pm 0.11^{(d)}$
QSO B0307-195B	14.48 ± 0.00	< 13.22	< 12.18	-	> 14.55	> 15.13	< 12.13	-
QSO J0427-1302	12.23 ± 0.04	< 13.23	< 11.75	-	13.90 ± 0.07	-	< 11.84	-
PKS 0454-220	14.71 ± 0.01	$13.69 \pm 0.08^{*}$	-	-	-	-	12.58 ± 0.01	-
J060008.1-504036	14.84 ± 0.03	13.62 ± 0.02	12.11 ± 0.03	12.78 ± 0.01	-	-	-	$< 12.5^{(e)}$
QSO B1036-2257	12.93 ± 0.01	< 12.93	< 11.74	-	13.71 ± 0.01	> 17.42	-	-
J115538.6+053050	-	13.74 ± 0.01	-	13.12 ± 0.01	13.56 ± 0.01	13.71 ± 0.01	-	-
LBQS 1232+0815	13.50 ± 0.01	< 13.05	< 11.58	13.28 ± 0.01	> 14.67	-	-	-
QSO J1330-2522	-	< 13.22	-	12.62 ± 0.02	-	-	-	-
QSO J1356-1101	13.44 ± 0.01	< 12.76	< 12.38	-	-	-	< 12.07	-
QSO J1621-0042	13.30 ± 0.04	-	-	-	14.24 ± 0.03	14.71 ± 0.01	-	$< 14.41^{(f)}$
4C 12.59	14.26 ± 0.08	-	-	-	-	-	-	-
LBQS 2114-4347	14.02 ± 0.01	< 12.88	< 12.17	< 12.09	13.43 ± 0.01	14.39 ± 0.01	< 12.24	-
QSO B2126-15	14.05 ± 0.01	13.15 ± 0.01	< 11.58	13.24 ± 0.02	-	-	-	-
QSO B2126-15	14.17 ± 0.00	-	< 11.95	13.11 ± 0.01	13.84 ± 0.13	-	< 12.28	-
LBQS 2132-4321	15.03 ± 0.02	13.77 ± 0.02	12.66 ± 0.02	13.25 ± 0.01	14.20 ± 0.01	-	-	-
QSO B2318-1107	14.14 ± 0.02	-	< 11.74	12.17 ± 0.02	-	< 14.10	11.78 ± 0.04	-

sults suggest that quasar absorbers differ from the Galactic depletion patterns or alternatively have a different nucleosynthetic history.

Also, the current QSO sample may suffer from dust selection bias. Indeed, it is possible that quasars in the background of dusty absorbers are not being accounted for in current selection techniques (Boissé et al. 1998). Programs to observe reddened quasars might bring valuable insights to the dust content of quasar absorbers (Maddox et al. 2012; Krogager et al. 2015, 2016). Using the analysis from Vladilo et al. (2006)[3], we recover estimates for the average extinction in our quasar absorber samples to be below 0.01, in line with results from Frank & Péroux (2010) or Khare et al. (2012). This suggests that the dust reddening is not observed in the current quasar selection.

Given these limitations, we do not apply dust corrections to the measured abundances. There is work underway (Tchernyshyov et al. 2015) to derive the parameters A_X, B_X and z_X for the Small Magellanic Cloud, which is more in line with the expected morphological type or H_2 fraction of DLAs.

[3] see Appendix A2 for details of the calculation

Table 3. Abundances with respect to solar for the 22 systems studied in this work. In column [X/H], (a) refers to Ar, (b) refers to O, (c) refers to N and (d) refers to C. For PKS 0454-220, the metallicities with the asterisk have been derived by Som et al. 2015.

QSO	z_{abs}	**log** N(H I)	**[S/H]**	**[Al/H]**	**[Si/H]**	**[Cr/H]**
QSO J0008-2900	2.254	20.22 ± 0.10	-	-	< -1.33	< -1.49
QSO J0008-2901	2.491	19.94 ± 0.11	-1.38 ± 0.21	-	-	< -0.68
QSO J0018-0913	0.584	20.11 ± 0.10	-	-	-	< -0.78
QSO J0041-4936	2.248	20.46 ± 0.13	< -0.75	> -0.85	-1.19 ± 0.16	-0.98 ± 0.58
QSO B0128-2150	1.857	20.21 ± 0.09	-1.00 ± 0.09	-	-0.90 ± 0.09	-
QSO J0132-0823	0.647	20.60 ± 0.12	-	-	-	< -1.07
QSO B0307-195B	1.788	19.00 ± 0.10	-	-	0.49 ± 0.10	< 0.13
QSO J0427-1302	1.562	19.35 ± 0.10	-	-2.02 ± 0.14	-	< -0.60
PKS 0454-220	0.474	19.45 ± 0.03	$0.49 \pm 0.04^*$	-	$> -0.78^*$	-
J060008.1-504036	2.149	20.40 ± 0.12	-	> -0.52	-0.83 ± 0.12	-0.94 ± 0.12
QSO B1036-2257	2.533	19.30 ± 0.10	-	-1.24 ± 0.10	-1.17 ± 0.10	< -0.40
J115538.6+053050	3.327	21.00 ± 0.10	-0.81 ± 0.10	-	-0.58 ± 0.10	-
LBQS 1232+0815	1.720	19.48 ± 0.13	< -0.41	-	-0.58 ± 0.13	< -0.74
QSO J1330-2522	2.654	19.56 ± 0.13	-	-1.83 ± 0.13	-	-
QSO J1356-1101	2.397	19.85 ± 0.08	-	-	-	< -0.85
QSO J1621-0042	3.104	19.70 ± 0.20	-	-	-1.43 ± 0.20	-
4C 12.59	0.531	20.70 ± 0.09	-	-	-	-
LBQS 2114-4347	1.912	19.50 ± 0.10	< -0.65	-0.95 ± 0.10	-0.62 ± 0.10	< -0.37
QSO B2126-15	2.638	19.25 ± 0.15	-	-	-0.09 ± 0.15	-
QSO B2126-15	2.769	19.20 ± 0.15	-	> 0.39	0.08 ± 0.15	< -0.44
LBQS 2132-4321	1.916	20.74 ± 0.09	> -0.96	-	-0.70 ± 0.10	-1.06 ± 0.11
QSO B2318-1107	1.629	20.52 ± 0.14	< -1.10	< -0.04	-	< -1.69

QSO	**[Fe/H]**	**[Ni/H]**	**[Zn/H]**	**[Mg/H]**	**[Mn/H]**	**[X/H]**
QSO J0008-2900	-1.94 ± 0.10	-	< -1.10	> -0.81	< -1.63	$< -1.55^{(a)}$
QSO J0008-2901	-1.79 ± 0.13	< -0.87	< -0.38	-	-	$-1.32 \pm 0.35^{(b)}$
QSO J0018-0913	-1.74 ± 0.10	-	< -0.26	-	-	-
QSO J0041-4936	-1.54 ± 0.14	-1.61 ± 0.20	-1.32 ± 0.16	-	-	$-2.36 \pm 0.13^{(c)}$
QSO B0128-2150	-1.27 ± 0.09	-1.17 ± 0.10	< -0.51	-	-	-
J013209-082349	-1.14 ± 0.14	-	-	-	-	-
QSO B0307-195B	-0.02 ± 0.10	< 0.00	< 0.62	-	< -0.30	-
QSO J0427-1302	-2.62 ± 0.11	< -0.34	< -0.16	-	< -0.94	-
PKS 0454-220	-0.24 ± 0.03	$0.02 \pm 0.09^*$	-	-	-0.30 ± 0.03	$-1.34 \pm 0.09^{*(c)}$
QSO J0132-0823	-1.06 ± 0.12	-1.00 ± 0.12	-0.85 ± 0.12	-	-	-
QSO B1036-2257	-1.87 ± 0.10	< -0.59	< -0.12	-1.33 ± 0.10	-	-
J115538.6+053050	-	-1.48 ± 0.10	-	-	-	-
LBQS 1232+0815	-1.48 ± 0.13	< -0.65	< -0.46	-	-	-
QSO J1330-2522	-	< -0.56	-	-	-	-
QSO J1356-1101	-1.91 ± 0.08	< -1.31	< -0.03	-	< -1.21	-
QSO J1621-0042	-1.90 ± 0.20	-	-	-	-	$< -1.72^{(d)}$
4C 12.59	-1.94 ± 0.12	-	-	-	-	$-5.77^{(d)}$
LBQS 2114-4347	-0.98 ± 0.10	< -0.84	< 0.11	-0.70 ± 0.10	< -0.69	-
QSO B2126-15	-0.70 ± 0.15	-0.32 ± 0.15	< -0.23	-	-	-
QSO B2126-15	-0.53 ± 0.15	-	< 0.19	-	< -0.35	-
LBQS 2132-4321	-1.21 ± 0.11	-1.19 ± 0.11	-0.64 ± 0.11	-	-	-
QSO B2318-1107	-1.88 ± 0.14	-	< -1.34	-	-2.17 ± 0.15	-

3.4 α-elements

The production of α-elements (O, N, Mg, Si, S, Ti, Ca...) and Fe-peak elements (V, Cr, Mn, Fe, Co, Ni...) has different origins in the history of star formation. α-elements are mainly created during core-collapse Type II supernovae (SNe), whereas Fe-peak elements originate mainly from thermonuclear Type Ia SNe. These two processes have different time scales, as they originate from distinct stellar populations: the Type II SNe occur from short-lived massive stars while Type Ia SNe are thought to involve binary pairs containing a white dwarf exchanging material over longer periods of time. Observations of different objects suggest an excess of α-elements with respect to Fe-peak elements (from Wallerstein (1962) for G-dwarf stars, to Timmes, Lauroesch & Truran (1995) for QSO absorption line systems and Rafelski et al. (2012) for DLAs).

In Fig. 3, we plot [α/Fe] versus metallicity using α = OI, SII, MgII and SiII for the sub-DLA (blue) and DLA (red) populations.

We observe a correlation between [α/Fe] and [α/H] for sub-DLAs. A Spearman test gives $\rho_{\rm sub-DLA} = 0.69$ with a probability of no correlation $P(\rho_{\rm sub-DLA}) < 10^{-7}$. This correlation spans from low- to high-metallicity systems. The total number of DLA detections adds up to 227 systems. We do not see a flattening for DLAs with [α/H] < -1 as in Rafelski et al. (2012), who attributed this flattening to the fact that the offsets in [α/Fe] values for [α/H] < -1 are the effect of α-enhancement only. To avoid any dust extinction

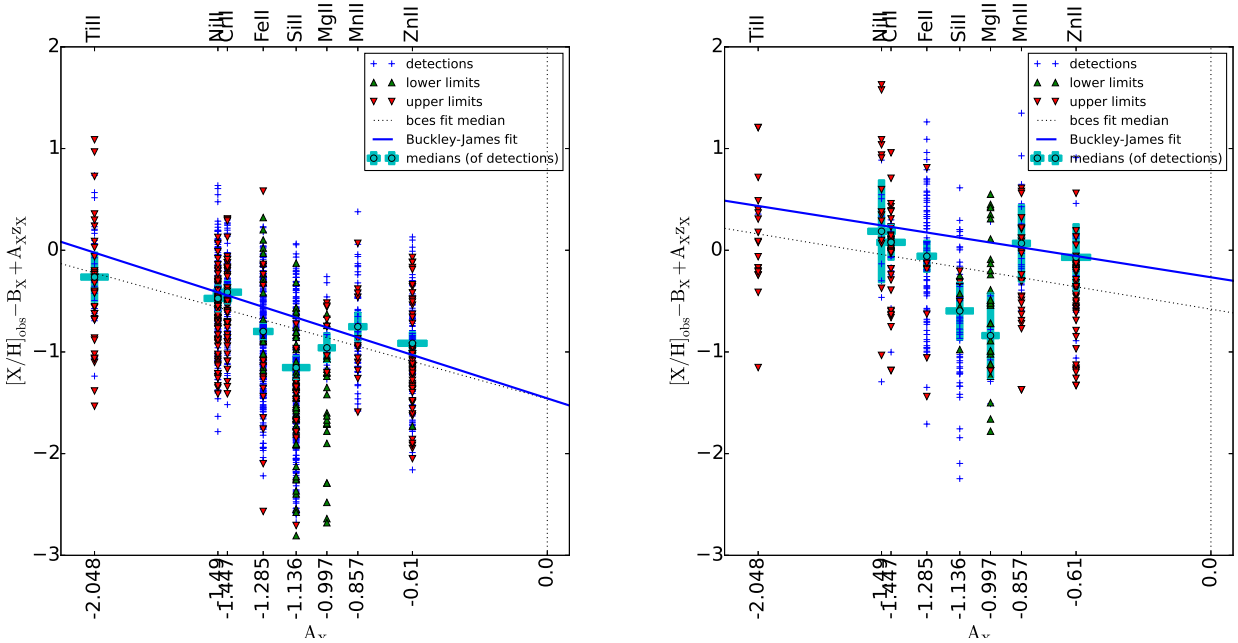

Figure 2. Fits of F_* from equation A5 for the DLAs (362 systems, left panel), and sub-DLAs (92 systems, right panel) in the EUADP+ sample. The blue crosses stand for the detections, the red triangles for the upper limits, the green triangles for lower lower limits, and the cyan points are the median of the detections for each element X. The fits are performed on the medians of the detections with a bisector fit (dashed line), and on the detections and the limits using a survival analysis technique, the Buckley-James method (solid line). We note that the α-elements (Mg and Si) are below the trend lines for both DLAs and sub-DLAs. We refer the reader to Appendix A1 for a mathematical description of the fit.

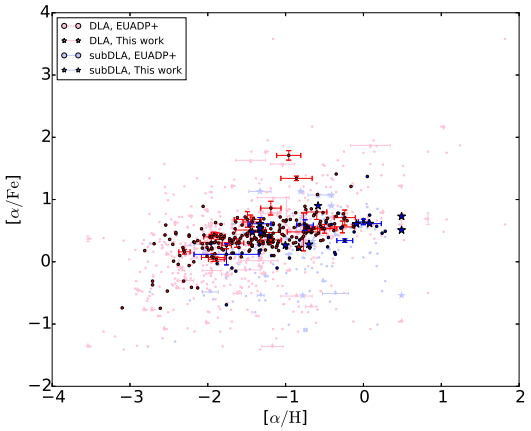

Figure 3. The α-enhancement of DLAs (red) and sub-DLAs (blue) versus metallicity, [α/Fe] versus [α/H], with α = OI, SII or SiII. For clarity, only one in ten data point displays error bars and the limits have faint colors.

effects, we consider the 80 DLAs with [α/H] < -1.5 to derive a correction for α-enhancement for the EUADP+ DLAs (De Cia et al. 2013). We note that these systems might still be affected by dust depletion, as a trend is still visible between [α/Fe] and [α/H], even for [α/H] down to -3 dex. We derive a mean value of [α/Fe] $= 0.32 \pm 0.18$ using 80 DLAs with [α/H] < -1.5, which is consistent with the value found by Rafelski et al. (2012).

DLAs and sub-DLAs may have different nucleosynthetic histories, as they may originate from galaxies of different masses (Khare et al. 2007; Kulkarni et al. 2010) and hence experience different star formation rates. Indeed, different [Mn/Fe] vs. [Zn/H] trends for DLAs and sub-DLAs suggest different nucleosynthetic histories for the two populations (Meiring et al. 2007; Som et al. 2015). Therefore, one expects their α-enhancement to be statistically different and probably higher for sub-DLAs, which may experience higher star formation rates. In Fig. 3, there is no apparent plateau for sub-DLAs, probably due to the small number of detections at low metallicities. More observations of sub-DLAs are needed to obtain more definitive conclusions in this H I column density regime. Nevertheless, to address the question of α-enhancement for sub-DLAs at least partly, we make use of the value derived for DLAs. These corrections add 0.32 ± 0.18 dex to every metallicity derived using element Fe. This doesn't include a correction for dust extinction.

We emphasize that such a trend of [α/Fe] versus [α/H] in DLAs/sub-DLAs does not necessarily imply nucleosynthetic α-enhancement. This is because of the increasing dust depletion of Fe with increasing metallicity, a trend that is seen to hold even at metallicities below -1 dex. [α/Zn] is indeed less prone to depletion than [α/Fe], but our current sub-DLA sample has only a limited number of Zn detections (19/92). Additional Zn observations in the future will help address this question better.

4 RESULTS

4.1 Evolution of metals with redshift

Together, DLA and sub-DLA populations contain the majority of the neutral gas mass in the Universe (Zafar et al. 2013). Therefore, they present a valuable tool to estimate the cosmic metallicity throughout the ages. Models of cosmic chemical evolution claim that the global interstellar metallicity would rise with decreasing redshift, to reach near solar metallicity values at present day (Lanzetta, Wolfe & Turnshek 1995; Pei & Fall 1995; Malaney & Chaboyer 1996; Pei, Fall & Hauser 1999; Tissera, Mosconi & Cora 2001). Sub-DLAs in particular contribute substantially to the cosmic metal budget. Indeed, Kulkarni et al. (2007) show that the contribution of sub-DLAs to the metal budget increases with decreasing redshift considering a constant relative H I gas in DLAs and sub-DLAs at low and high redshifts. Bouché et al. (2007) anticipate that $\lesssim 17$ per cent of the metals are in sub-DLAs at $z \sim 2.5$ but this estimate is highly dependent on the ionized fraction of the gas. It is therefore highly important to compare sub-DLA metallicities with those of DLAs. Our study adds 15 new measurements of sub-DLA metallicity. We chose to use ZnII as our main metallicity indicator (Pettini et al. 1994) as it is nearly undepleted onto interstellar dust. Moreover, ZnII lines are usually unsaturated, and since ZnII is the dominant ionization state in neutral regions, it does not require strong ionization correction. However, Zn has an overall low cosmic abundance and the stronger lines $\lambda\lambda$ 2026 and 2062 can be blended with MgI λ 2026 and CrII λ 2062. When these ZnII lines are undetected, we use the dominant ions of other elements in the following order: OI, SII, SiII, MgII, FeII (corrected for the α analysis) and NiII.

Fig. 4 shows the evolution of the metallicity [M/H] with redshift of the systems for the 92 sub-DLAs (bottom panel) and the 362 DLAs (top panel) from the EUADP+ sample, color-coded with respect to the element used to derive the metallicity. We note that Zn is only detected up to $z = 3$ (but for one DLA measured at $z \sim 4$), and O is only derived for metal-poor systems ([M/H] < -1) because OI λ 1302, the only OI line usually accessible to ground-based telescopes, is saturated otherwise.

Lanzetta, Wolfe & Turnshek (1995) estimated the cosmic metallicity from the gas mass density Ω_g and metal mass density Ω_m via the H I-weighted mean metallicity $\langle Z \rangle$:

$$< Z(z) >= \Omega_m(z)/\Omega_g(z) = \frac{\sum_i Z_i N(H\,I)_i}{\sum_i N(H\,I)_i} \qquad (3)$$

Fig. 5 shows the metallicity derived in our sample, as well as the H I-weighted mean metallicity $\langle Z \rangle$ for both populations (sub-DLAs in blue and DLAs in red).The bins for $\langle Z \rangle$ are chosen such that there is an almost constant number of systems in each bin, that is 16 for the sub-DLAs and 26 for the DLAs.The vertical error bars are derived from the consideration on sampling and measurements errors. The sampling errors are calculated from a bootstrap technique as described in Rafelski et al. (2012) and the measurement errors from the propagation formula. The total errors are the quadratic sums of these two quantities for each bin. We note a large scatter for a third of the newly derived sub-DLA metallicities (blue dots). This points out to the need for a larger sample of sub-DLA measurements at all redshifts.

We measure an anti-correlation between redshift and metallicity for both populations. The Spearman coefficient for sub-DLAs is $\rho = -0.49$ and $\rho = -0.55$ for DLAs, with probabilities of no correlation $P(\rho) < 10^{-6}$ for both populations. The Kendall's τ is -0.34 for sub-DLAs and -0.38 for DLAs, with a probability of no-correlation of below 10^{-5} for both populations. The dotted lines in Fig. 5 show the best bisector fits for the metallicity evolution with redshift of both populations. We measure

$$< Z >_{DLAs}= (-0.15 \pm 0.03)\ z - (0.6 \pm 0.13) \qquad (4)$$

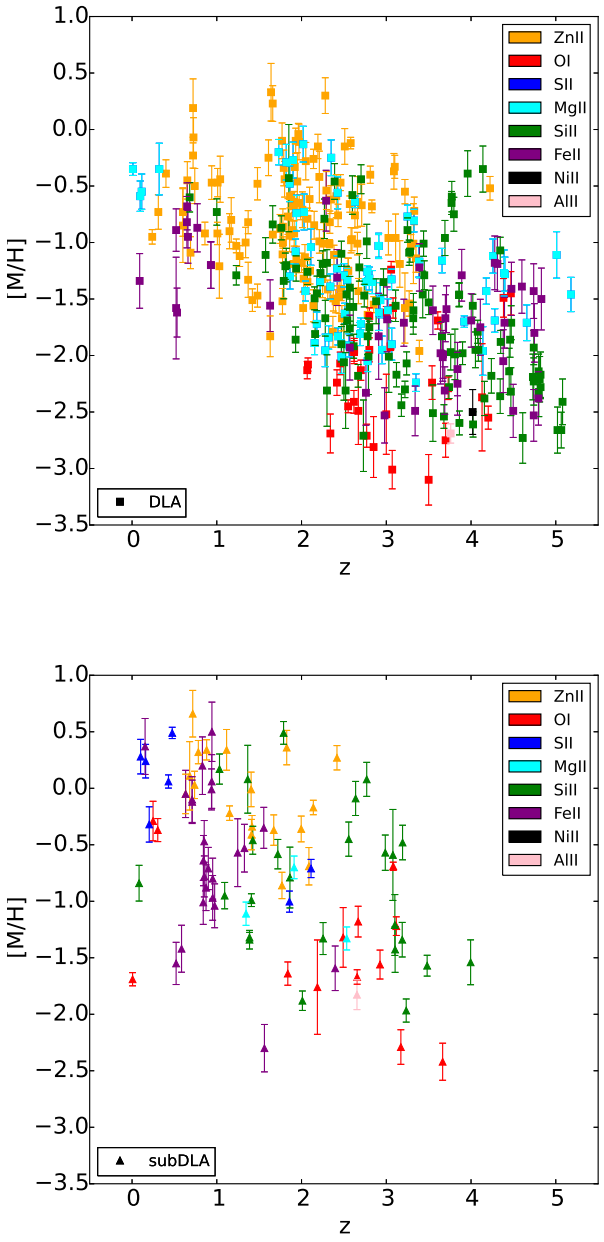

Figure 4. Evolution of [M/H] with redshift, color-coded with respect to the element used to derive the metallicity for DLAs (top panel) and sub-DLAs (bottom panel) from the EUADP+ sample.

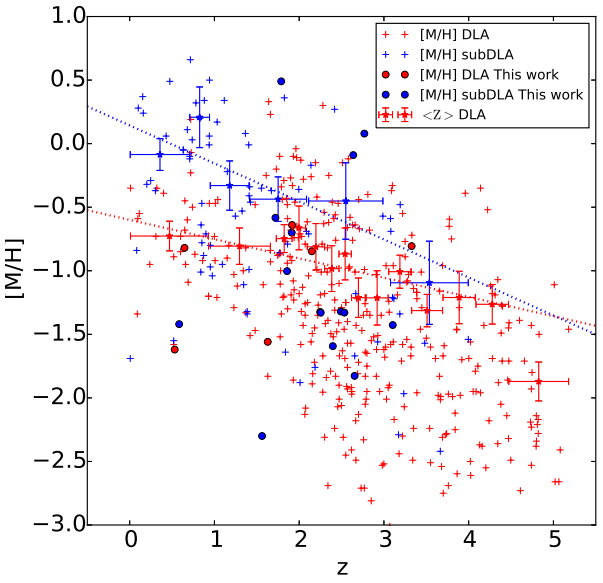

Figure 5. Evolution of the N(HI)-weighted mean metallicity ⟨Z⟩ with redshift. Clearly, both DLA and sub-DLA populations show an increase of ⟨Z⟩ with decreasing redshift, but sub-DLAs have a steeper evolution of ⟨Z⟩ with redshift than DLAs. We also note a floor at [X/H] = −3 below which no metals are detected.

$$< \mathrm{Z} >_{\mathrm{sub-DLAs}} = (-0.30 \pm 0.07)\ \mathrm{z} + (0.15 \pm 0.31) \qquad (5)$$

The fit has been performed shifting the y-axis to z = 3 to minimize the error on the intercept and ignoring the last DLA bin which presents a rapid decline in metallicity (Rafelski et al. 2014). The evolution with redshift is steeper for sub-DLAs than for DLAs. Previous authors (Khare et al. 2007; Kulkarni et al. 2010) argued that this effect might arise from the fact that sub-DLAs are more massive than DLAs.

Our results are in agreement with previous work (Kulkarni et al. 2007, 2010; Som et al. 2015), with a more significant result in the sub-DLA regime thanks to the larger sample presented here. The slope remains unchanged with respect to earlier studies. However, the significance of the result increases indicating a convergence towards a realistic value of the slope.

4.2 Kinematics

In addition to the different abundances derived from Voigt profile fitting, information on the kinematics of the absorbers can be derived from the UVES high resolution spectra.

4.2.1 Voigt Profile Optical Depth Method

We use the definition of the velocity interval ΔV_{90} as defined by Prochaska & Wolfe (1997b), based on the integrated optical depth $\tau_{tot} = \int \tau(v)dv$ and considering the velocity interval from 5% to 95% of this quantity.

In this paper, we do not consider the apparent optical depth (AOD) $\tau_{app} = -\log(I/I_c)$ to derive the velocity interval, as is usually done, but we use instead the optical depth derived from the Voigt profile fits (see appendix C for a description of the fits for every system individually). This method, which we refer to as Voigt profile optical depth (VPOD) method, makes use of the information gathered from the fits. The saturation and contamination issues are then considered when deriving ΔV_{90}. This is the main difference with the AOD method, which might provide ΔV_{90} measurements affected by blends. In the VPOD method, we use simultaneously the information on several transitions to derive the velocity interval for any ion. Indeed, the only quantity that differs between transitions of the same ion is the oscillator strength, which has no impact on the velocity axis. Fig. 6 shows an example of the derivation of the velocity interval for an FeII line. Table 4 summarizes the ΔV_{90} measurements for the 22 systems studied here. For 20 of them, we use the information from the FeII lines as it is the ion most detected in our sample.

One of the sub-DLA in our sample, towards PKS 0454-220, has already been studied by Som et al. (2015). They use SII λ 1250 from an HST/COS spectrum and derive ΔV_{90}=155 km/s based on the AOD method. However, we find with the VPOD method described above a value almost twice smaller. We use the AOD method on the UVES spectrum with FeII λ 2374 and derive $\Delta V_{90}\sim$85.0 km/s, consistent with the result from the VPOD method. We note that the Line Spread Function (LSF) derived from the COS consortium is responsible for the reported large value. To overcome this problem, we exclude COS measurements from our analysis.

In conclusion, the VPOD ΔV_{90} values are not sensitive to blending and saturation effects, to the shape of the instrument's LSF, its resolution and to the SNR of the derived spectrum. We note that depletion of refractory elements contributes to the error in the ΔV_{90} because the different components can be affected differently by dust depletion. In the present study, FeII has been used because it is uniformly detected among the 22 new systems presented here. In the remaining of the sample there is no object in common between the EUADP and the already derived ΔV_{90} found in the literature.

4.2.2 ΔV_{90} versus Metallicity Relation

Recently, Som et al. (2015) compared for the first time the sub-DLA metallicity versus velocity width trend over a statistically significant sample of 31 sub-DLAs at $0.1 \leqslant z_{abs} \leqslant 3.1$. We propose here to extend their analysis to a wider sub-DLA sample using our new 15 sub-DLAs. We consider a different sample than the one used in the remaining of the paper (EUADP+) as the velocity widths are not provided by all authors. We consider the data from Ledoux et al. (2006) (52 DLAs and 14 sub-DLAs at redshifts $1.7 \leqslant z_{abs} \leqslant 4.3$, corrected for Asplund et al. (2009) photospheric solar abundances), observations from Meiring et al. (2009b) (29 sub-DLAs at redshifts $z_{abs} < 1.5$, corrected for Asplund et al. (2009) photospheric solar abundances), observations from Neeleman et al. (2013) (98 DLAs at redshifts $1.6613 \leqslant z_{abs} \leqslant 5.0647$), observations from Moller et al. (2013) (4 DLAs at redshifts $1.9 \leqslant z_{abs} \leqslant 3.1$), as well

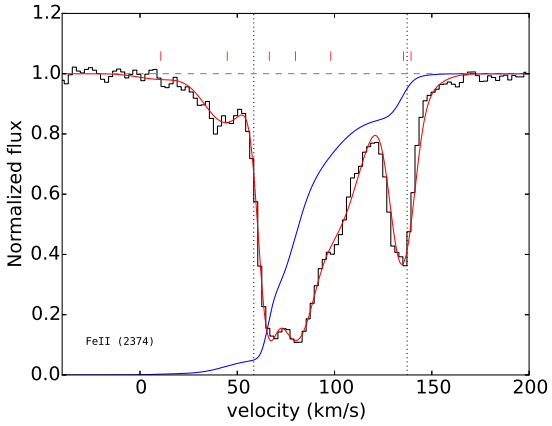

Figure 6. An example illustrating the computation of the velocity interval ΔV_{90}. The black curve is the normalized spectrum of PKS 0454-220 centered on the FeII λ 2374 line, the red curve is the Voigt profile fit of the absorption and the blue curve is the integrated optical depth derived from the Voigt profile. The vertical dotted lines indicates the 5% and 95% thresholds for the integrated optical depth, defining the velocity width ΔV_{90}.

Table 4. Measures of ΔV_{90} in our sample derived from Voigt profile fits to the FeII lines (except for two systems with no Fe coverage, for which we used SiII (a) and AlII (b)).

QSO	z_{abs}	log N(H I) [cm^{-2}]	Δv_{90} [km/s]
QSO J0008-2900	2.254	20.22	53.7
QSO J0008-2901	2.491	19.94	12.4
QSO J0018-0913	0.584	20.11	192.6
QSO J0041-4936	2.248	20.46	21.2
QSO B0128-2150	1.857	20.21	53.7
QSO J0132-0823	0.647	20.60	76.5
QSO B0307-195B	1.788	19.00	204.8
QSO J0427-1302	1.562	19.35	7.8
PKS 0454-220	0.474	19.45	78.7
J060008.1-504036	2.149	20.40	79.9
QSO B1036-2257	2.533	19.30	220.4
J115538.6+053050	3.327	21.00	186.8[a]
LBQS 1232+0815	1.72	19.48	167.6
QSO J1330-2522	2.654	19.56	21.0[b]
QSO J1356-1101	2.397	19.85	337.7
QSO J1621-0042	3.104	19.70	161.9
4C 12.59	0.531	20.70	62.4
LBQS 2114-4347	1.912	19.50	135.9
QSO B2126-15	2.638	19.25	62.3
QSO B2126-15	2.769	19.20	121.2
LBQS 2132-4321	1.916	20.74	233.4
QSO B2318-1107	1.629	20.52	13.8

as results from this study (see Table 4). We only consider the systems with detected [α/H] (11/15 sub-DLAs and 4/7 DLAs). The resulting sample gathers 54 sub-DLAs and 162 DLAs.

Fig. 7 shows the trend between the metallicity and the velocity width ΔV_{90} for sub-DLAs (bottom panel) and DLAs (top panel) from this ΔV_{90} sample.

We fit both populations with the best bisector fits:

$$[\mathrm{X/H}]_{\mathrm{DLA}} = (1.52 \pm 0.08)\ \log \Delta V_{90} - (4.20 \pm 0.16) \quad (6)$$

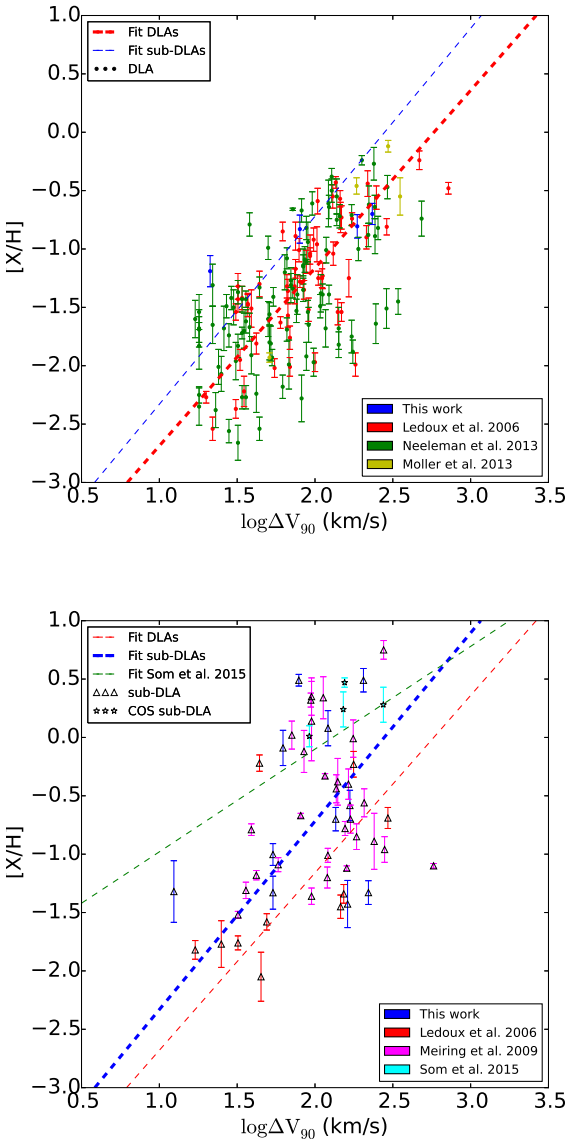

Figure 7. [X/H] versus ΔV_{90} for the newly derived systems, the systems from Ledoux et al. (2006), Neeleman et al. (2013), Som et al. (2015), Meiring et al. (2009b), and Moller et al. (2013) in blue, red, green, cyan, magenta and yellow, respectively. The upper panel shows the DLAs and the bottom panel the sub-DLAs. The data points measured with COS (stars) are not considered for the fit due to the discussion in section 4.2.1. The open triangles represent the sub-DLAs and the dots the DLAs. The dashed blue line reproduces the bisector fit of the sub-DLAs, the dashed red line is the bisector fit for all the DLAs and the green dashed line in the lower panel represents the Som et al. (2015) sub-DLA fit.

$$[\mathrm{X/H}]_{\mathrm{sub-DLA}} = (1.61 \pm 0.22)\ \log \Delta V_{90} - (3.94 \pm 0.45) \quad (7)$$

The fits are performed shifting the y-axis to $\log \Delta V_{90} = 2$ to minimize the error on the intercept.

Som et al. (2015) find a higher intercept and a shallower slope for the sub-DLA population, using only Zn and S with ionization corrections. Although this result is free from dust depletion effect on the metallicity estimation, it might be

biased towards higher metallicity sub-DLAs, where Zn or S can be measured. A larger Zn-based metallicity sub-DLAs samples is required to recover the metallicity-ΔV_{90} relation free from the effects of dust bias.

A larger Zn-based metallicity sub-DLAs samples is required to recover the metallicity-Delta v relation free from the effects of dust bias.

As in previous studies, the DLA sample is well correlated. The Spearman coefficient is $\rho = 0.63$, with a probability of no correlation $< 10^{-6}$. The Kendall's τ is 0.46 with a probability of no correlation $< 10^{-6}$. The sub-DLA sample is less correlated than the DLA sample, in agreement with Som et al. (2015). The Spearman coefficient is $\rho = 0.39$, with a probability of no correlation of 0.004. The Kendall's τ is 0.25 with a probability of no correlation of 0.007. Adding more sub-DLAs to the ΔV_{90}-metallicity relation does not improve the correlation. Som et al. (2015) showed that the ionization correction also does not improve this correlation. This indicates a larger spread for the sub-DLAs, which may originate from more complex kinematic behaviors in sub-DLA clouds. However, the determination of ΔV_{90} appears to be sensitive to the resolution, the LSF and the SNR of the data. This might contribute to the observed scatter, although an intrinsic scatter is expected from CGM regions.

4.2.3 Is ΔV_{90} a Reliable Tracer of Mass?

A mass-metallicity relation (hereafter MZR) has been reported at low redshifts (Lequeux et al. 1979; Tremonti et al. 2004), intermediate redshifts (Savaglio et al. 2005) and high redshifts (Erb et al. 2006). It relates the stellar mass of galaxies to the metallicity of their ISM. This relation is crucial in our understanding of galaxy evolution as it supports the theory of metal ejection from galactic outflows in low-mass (and hence low potential well) galaxies and their enrichment with accreting metal-poor IGM gas, diluting the galactic metallicity.

For quasar absorbers, some simulations indicate that the origin of the velocity width, ΔV_{90}, could be strongly related to the gravitational potential well of the absorption system's host galaxy (e.g. Prochaska & Wolfe 1997b; Haehnelt, Steinmetz & Rauch 1998; Pontzen et al. 2008). Similarly, assuming a scaling of the galaxies luminosity with dark matter haloes, Ledoux et al. (2006) and later Moller et al. (2013) proposed to interpret the ΔV_{90} versus metallicity relation of quasar absorbers as a MZR. Such a picture does not take into account the complex gas processes at play now known to take place in CGM regions. In other words, the ΔV_{90} may reflect bulk motions of the absorbing gas rather than motions governed by the gravitational potential well.

Observationally, a measurement of mass and ΔV_{90} has been possible in few individual systems. Infra-red IFU SINFONI observations of the galaxy hosts of 3 DLAs and 2 sub-DLAs in Péroux et al. (2011) and Péroux, Kulkarni & York (2014) allow one to determine the mass of the systems from a detailed kinematic study. In addition, Christensen et al. (2014) has used photometric information of the galaxy hosts and Spectral Energy Distribution (SED) fits to estimate the stellar mass of 13 DLAs. Combined together, these findings suggest that, individually, the absorption systems align well with the MZR reported at these redshifts.

In addition to these measurements in a few specific systems, several authors have put constraints on the mass estimates of quasar absorbers in a statistical manner. Interestingly, the local analogues to DLAs, the 21cm z = 0 emitting galaxies studied with HIPASS by Zwaan et al. (2008) show that the quantity ΔV_{90} correlates little with mass. Similarly, Bouché et al. (2007) (and later Lundgren et al. 2009; Gauthier et al. 2014) have used the ratio of MgII systems auto-correlation with a correlation with Luminous Red Galaxies (LRG) at the same redshifts to derive an estimate of the overall mass of quasar absorbers. Their findings show an anti-correlation between equivalent width, a proxy for ΔV_{90}, and metallicity. Admittedly, the populations of absorbers do not completely overlap, the Ledoux et al. (2006) sample contains mostly DLAs, while the MgII sample of Bouché et al. (2007) might have at most 25% of DLAs (according to the criterion of Rao, Turnshek & Nestor (2006): 50% meet the FeII/MgII criteria and 35-50% of these are DLAs). In fact, Bouché et al. (2007) and Schroetter et al. (2015) argue that MgII absorbers can be used to trace superwinds as they are not virialized in the gaseous halo of the host-galaxies. Bouché et al. (2012) also show that the inclination of the galaxy has a direct impact on the absorption profile and therefore on the velocity width. Put together, these many lines of evidence question the interpretation of the velocity width as a proxy for the mass of the host galaxy and the interpretation of the ΔV_{90}/metallicity correlation as a MZR for quasar absorbers.

4.3 Tracing the Circum-Galactic Medium with sub-DLAs

Our understanding of galaxy formation and evolution is tightly linked with the study of two opposite processes that take place within the CGM. Indeed, to create stars, the galaxy requires a continuous input of cold gas, that is believed to accrete along the filamentary structures from the cosmic web. In addition, cosmological simulations fail to reproduce the observed SFR without invoking feedback processes from star formation itself or AGN activity. These outflowing processes and their large scale impact have been confirmed observationnally (Steidel et al. 2010; Bouché et al. 2012; Kacprzak et al. 2014), but there is still little observational evidence for accretion of cool material (Bouché et al. 2013; Cantalupo et al. 2014; Martin et al. 2014). Quasar absorbers with H I column densities in the range of LLS and sub-DLAs are believed to be good probes of this CGM (Fumagalli et al. 2011; van de Voort & Schaye 2012). Lehner et al. (2013, 2014) report a bimodality in the metallicity distribution of 29 $z < 1$ LLS, which they interpret as the signatures of outflows (metal-rich) and infalls (metal-poor).

Lehner et al. (2013) extended their analysis on 29 sub-DLAs and 26 DLAs, but do not report a bimodality distribution in the metallicity of these systems based on α-elements. Clearly, larger samples of quasar absorbers are required to perform such studies.

Here, we perform similar analysis on a larger sample of sub-DLAs and DLAs with a broad redshift range.

Fig. 8 shows the bimodal metallicity distribution in $z < 1$ LLS by Lehner et al. (2013) and the α-element metallicity distribution for DLAs (316 systems) and sub-DLAs (68 systems) derived from our EUADP+ sample at all redshifts.

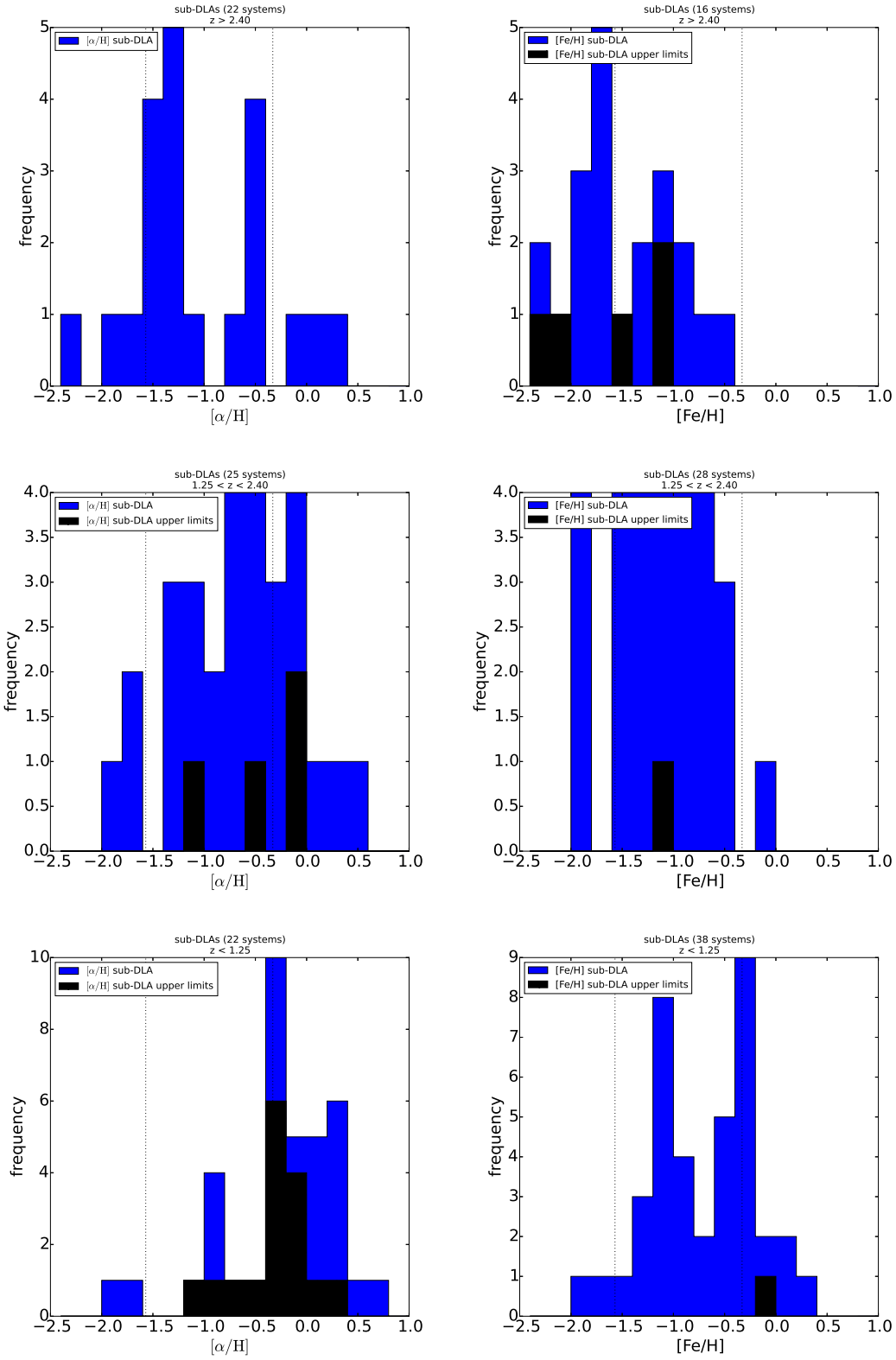

Figure 9. Metallicity (left panels: [α/H], right panels: [Fe/H]) distribution of sub-DLAs for different redshift bins: z > 2.4 (top panels), 1.25 < z < 2.4 (middle panels) and z < 1.25 (bottom panels). The black vertical dashed lines represent the mean values derived from the z_{abs} < 1 LLS sub-groups by Lehner et al. (2013). The black areas represent upper limits. The metallicity distribution is a strong function of redshift and only the lowest redshift range presents hints of a bimodal distribution for the [Fe/H] metallicity.

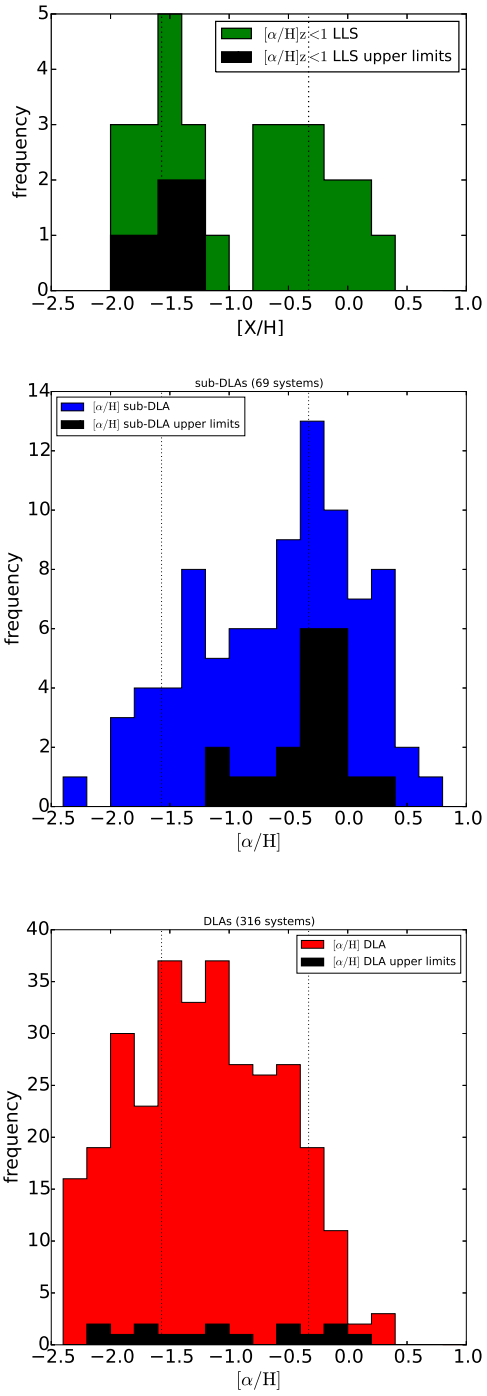

Figure 8. Metallicity [α/H] distribution of LLSs (top panel), sub-DLAs (middle panel) and DLAs (bottom panel). The histogram for LLSs has been taken from Lehner et al. (2013) and indicates a bimodality in the metallicity distribution for LLS at z < 1. The black vertical dashed lines represent the mean values derived from the $z_{abs} < 1$ LLS sub-groups by Lehner et al. (2013).

The sub-DLA [α/H] distribution in the middle panel of Fig. 8 also suggests bimodality.

In Fig. 9, we plot the distribution of the α abundances (left panels) and Fe abundances (right panels) for the EUADP+ sub-DLAs in 3 redshift bins ($z_{abs} > 2.4$ for the upper panels, $1.25 \leqslant z_{abs} \leqslant 2.4$ for the middle panels and $z_{abs} < 1.25$ for the bottom panels). We consider the metallicity traced by FeII as we have more detections with this ion and it is little affected by photo-ionization effect, even though Fe has an inclination to lock up onto dust grains. These histograms reveal the strong metallicity evolution with redshift for sub-DLAs. The sub-DLAs in the high redshift bin, $z_{abs} > 2.4$, present an unimodal distribution centered around [M/H]~ -1.6, similar to the metal-poor LLS population derived by Lehner et al. (2013). At intermediate redshifts, $1.25 \leqslant z_{abs} \leqslant 2.4$, a transition from low to higher metallicities appears. At low redshifts, $z_{abs} < 1.25$, however, the distribution presents hints of a bimodal distribution. This trend is more pronounced for the [Fe/H] distribution. A DIP test rejects the unimodal distribution at a significance level of 83%, taking the upper limit as a detection. The peaks of the distribution are located at [Fe/H] = -1.12 and [Fe/H] = -0.29, from a Gaussian Mixture Modeling. These values are compared with what is expected from simulations in terms of metallicity of accreting or outflowing gas. The prediction for the cold-mode accretion metallicity is above a hundredth solar, which is in line with the metal poor population in our distribution (Ocvirk, Pichon & Teyssier 2008; Shen et al. 2013). Therefore, the metal rich population should trace either outflowing gas or gas directly associated with the galaxy's ISM. However, this is not seen in the [α/H] distribution, where the DIP test rejects the unimodal distribution at a significance level of 31%, still taking upper limits as detections. But these limits are located at the high metallicity end of the distribution, and therefore do not contradict the possible bimodal distribution seen in [Fe/H].

These results indicate a similar behavior for low redshift sub-DLAs as for low redshift LLS. However, we expect the position of the peaks to be higher than those derived for the z < 1 LLS, as the [Fe/H] metallicity is underestimated due to depletion of Fe onto dust grains. Lehner et al. (in prep.) show that the bimodal distribution for LLS disappears at higher redshifts, similarly to what we find with sub-DLAs at higher redshifts. We note however that the bimodality in LLS could perhaps be incorrect, given that there are larger uncertainties in the metallicity determination of LLS (due to ionization corrections).

We note that the effect of redshift plays an essential role in such an analysis, as illustrated in Fig. 9.

Altogether, larger samples of both LLS and sub-DLAs at low-redshifts are required to distinguish between metal-poor gas accreting onto the galaxy and metal-rich gas being expelled.

5 CONCLUSION

We present in this paper physical properties of 15 new sub-damped Lyman-α absorbers seen in absorption in background quasar's high resolution UVES spectra. These systems cover a wide redshift range ($0.584 \leqslant z_{abs} \leqslant 3.104$). The

metallicity measurements were performed using Voigt profile fitting of the normalized high resolution UVES quasar spectra. Our sub-DLA measurements add significantly to previous studies since high resolution spectroscopy is required to study these systems.

We apply a multi-element based method to assess the level of dust depletion in the line of sight to the quasar. This study appears to be promising as it uses the combined information from several ions, and is relative to measurements of our Galaxy's ISM. With a survival analysis, we derive the best fit of the depletion factor F_* for the DLAs and sub-DLAs and find negative values, statistically different, for both groups: $F_*^{\rm sub-DLA} = -0.34 \pm 0.19$ and $F_*^{\rm DLA} = -0.70 \pm 0.06$. In comparison with values derived in our Galaxy, DLAs lie outside the halo and the sub-DLAs are associated with Halo like stars, in terms of depletion patterns. This is counter-intuitive as we expect DLAs to be more self-shielded to the UV background than sub-DLAs. We conclude that quasar absorbers differ from the Galactic depletion patterns or alternatively have a different nucleosynthetic history. Future analysis with the Small Magellanic Cloud will enable comparisons to a galaxy more in line with the morphology or the H_2 fraction of DLAs. Moreover, we derive the averaged rest frame extinction A_V for both populations to be below 0.01, suggesting that dust reddening is not observed in the current quasar selection.

We then examine the relative abundances of Fe and α-elements. We derived an offset in [α/Fe] for the DLAs in our sample of 0.32 ± 0.18, excluding systems with [α/H] > -1.5 to be less sensitive to dust depletion. This value is similar to that derived by Rafelski et al. (2012). However, we cannot derive a similar parameter for the sub-DLA population as we can not disentangle dust depletion effects from the α-enhancement. We therefore apply the DLA corrections to the sub-DLAs.

We study the evolution of the cosmic metallicity Ω_m, also described by the mean H I-weighted metallicity $\langle$Z$\rangle$. We confirm the steeper evolution of sub-DLAs than DLAs eventually reaching a solar metallicity at low redshifts as expected from chemical evolution models. We note that a third of the newly derived sub-DLA abundances appear as outliers from the previous data.

We measure the velocity width of the absorption systems in our new sample, ΔV_{90}, with a new method using the information from the Voigt profile fits. We confirm that there is a correlation between ΔV_{90} and metallicity for sub-DLAs. Indeed, sub-DLAs are potentially probing a different mass range than DLAs. Sub-DLAs could have a more important feedback mechanism than DLAs, thus increasing the scatter and weakening the possible velocity width/metallicity correlation.

Finally, we look at the metallicity distribution of sub-DLAs. At low redshifts, $z_{\rm abs} < 1.25$, we see a hint of a bimodal distribution which peaks at ~ -1.1 and ~ -0.3. This indicates that low-redshift sub-DLAs are tracing different mechanisms at play within the CGM, such as cold-mode accretion and outflows. Larger samples of sub-DLAs and LLS abundances at low redshifts are required to better identify their connection to gas inflow/outflow processes.

ACKNOWLEDGEMENTS

We thank N. Lehner, C. Howk, M. Fumagalli, M. Rafelski, M. Pieri, R. Bordoloi, J. O'Meara, D. Som and P. Møller for useful discussions. This work has been funded within the BINGO! ('history of Baryons: INtergalactic medium/Galaxies cO-evolution') project by the Agence Nationale de la Recherche (ANR) under the allocation ANR-08-BLAN-0316-01 as well as within the REGAL ('what REgulates the growth of GALaxies? ') project by the Labex (Laboratoire d'Excellence) OCEVU ('Origines, Constituants et Evolution de l'Univers'). This work has been carried out thanks to the support of the OCEVU Labex (ANR-11-LABX-0060) and the A*MIDEX project (ANR-11-IDEX-0001-02) funded by the "Investissements d'Avenir" French government program managed by the ANR. We thanks Pierre Mege for contributing in the development of the VPOD method. SQ acknowledges CNRS and CNES support for the funding of his PhD. CP thanks the ESO science visitor program for support. VPK acknowledges partial support from the NSF grant AST/1108830, with additional support from NASA grant NNX14AG74G and NASA/STScI grant for program GO 12536. EJ thanks Aix-Marseille University and Cécile Gry for a visit where part of this work was undertaken.

REFERENCES

Adelberger K. L., Shapley a. E., Steidel C. C., Pettini M., Erb D. K., Reddy N. a., 2005, The Astrophysical Journal, 629, 636

Akerman C. J., Ellison S. L., Pettini M., Steidel C. C., 2005, Astronomy and Astrophysics, 440, 499

Asplund M., Grevesse N., Sauval a. J., Scott P., 2009, Annu. Rev. Astron. Astrophys, 47, 481

Barbuy B., Hill V., Zoccali M., Minniti D., Renzini A., 2015

Battisti a. J. et al., 2012, The Astrophysical Journal, 744, 93

Bauermeister A., Blitz L., Ma C.-P., 2010, The Astrophysical Journal, 717, 323

Berg T. A. M., Ellison S. L., Prochaska J. X., Venn K. A., Dessauges-Zavadsky M., 2015a, Monthly Notices of the Royal Astronomical Society, 452, 4326

Berg T. A. M., Ellison S. L., Venn K. A., Prochaska J. X., 2013, Monthly Notices of the Royal Astronomical Society, 434, 2892

Berg T. A. M., Neeleman M., Prochaska J. X., Ellison S. L., Wolfe A. M., 2015b, Publications of the Astronomical Society of the Pacific, 127, 167

Bergeron J., Dodorico S., 1986, Monthly Notices of the Royal Astronomical Society, 220, 833

Bertone S., Schaye J., Booth C. M., Vecchia C. D., Theuns T., Wiersma R. P. C., 2010a, Monthly Notices of the Royal Astronomical Society, 408, 1120

Bertone S., Schaye J., Vecchia C. D., Booth C. M., Theuns T., Wiersma R. P. C., 2010b, Monthly Notices of the Royal Astronomical Society, 407, 544

Birnboim Y., Dekel A., 2003, Monthly Notices of the Royal Astronomical Society, 345, 349

Blades J. C., Hunstead R. W., Murdoch H. S., Pettini M.,

1982, Monthly Notices of the Royal Astronomical Society, 200, 1091
Boissé P., Brun V. L., Bergeron J.-m., Deharveng J.-m., 1998, Astronomy and Astrophysics, 333, 23
Bouché N., Hohensee W., Vargas R., Kacprzak G. G., Martin C. L., Cooke J., Churchill C. W., 2012, Monthly Notices of the Royal Astronomical Society, 426, 801
Bouché N., Murphy M., Péroux C., Csabai I., Wild V., 2007, New Astronomy Reviews, 51, 131
Bouché N., Murphy M. T., Kacprzak G. G., Péroux C., Contini T., Martin C. L., Dessauges-Zavadsky M., 2013, Science (New York, N.Y.), 341, 50
Bowen D. V., Jenkins E. B., Pettini M., Tripp T. M., 2005, ApJ, 635, 880
Cantalupo S., Arrigoni-Battaia F., Prochaska J. X., Hennawi J. F., Madau P., 2014, Nature, 506, 63
Carswell R. F. et al., 1996, Monthly Notices of the Royal Astronomical Society, 278, 506
Centurion M., Bonifacio P., Molaro P., Vladilo G., 2000, The Astrophysical Journal, 536, 540
Centurion M., Molaro P., Vladilo G., Peroux C., Levshakov S. a., D'Odorico V., 2003, Astronomy and Astrophysics, 403, 55
Chen H.-W., Kennicutt R., Rauch M., 2005, \Apj, 620, 703
Christensen L., Møller P., Fynbo J. P. U., Zafar T., 2014, 000, 15
Churchill C. W., Mellon R. R., Charlton J. C., Jannuzi B. T., Kirhakos S., Steidel C. C., Schneider D. P., 2000, The Astrophysical Journal, 543, 577
Cooke R., Pettini M., Murphy M. T., 2012, Monthly Notices of the Royal Astronomical Society, 425, 347
Cooke R., Pettini M., Steidel C. C., King L. J., Rudie G. C., Rakic O., 2010a, Monthly Notices of the Royal Astronomical Society, 409, 679
Cooke R., Pettini M., Steidel C. C., Rudie G. C., Jorgenson R. A., 2010b, Monthly Notices of the Royal Astronomical Society, 412, no
Cooke R., Pettini M., Steidel C. C., Rudie G. C., Nissen P. E., 2011, Monthly Notices of the Royal Astronomical Society, 417, 1534
Crighton N. H. M., Hennawi J. F., Prochaska J. X., 2013, The Astrophysical Journal, 776, L18
De Cia A., Ledoux C., Savaglio S., Schady P., Vreeswijk P. M., 2013, Astronomy & Astrophysics, 560, A88
de la Varga A., Reimers D., Tytler D., Barlow T., Burles S., 2000, AA, 363, 69
Dekel A., Birnboim Y., 2006, Monthly Notices of the Royal Astronomical Society, 368, 2
Dessauges-Zavadsky M., Calura F., Prochaska J. X., D'Odorico S., Matteucci F., 2004, Astronomy and Astrophysics, 416, 79
Dessauges-Zavadsky M., Calura F., Prochaska J. X., D'Odorico S., Matteucci F., 2007, Astronomy and Astrophysics, 470, 431
Dessauges-Zavadsky M., D'Odorico S., McMahon R. G., Molaro P., Ledoux C., Proux C., Storrie-Lombardi L. J., 2001, Astronomy and Astrophysics, 370, 426
Dessauges-Zavadsky M., Ellison S. L., Murphy M. T., 2009, Revisiting the origin of the high metallicities of sub-damped Lyman-alpha systems
Dessauges-Zavadsky M., Péroux C., Kim T.-S., D'Odorico S., McMahon R. G., 2003, Monthly Notices of the Royal Astronomical Society, 345, 447
Dessauges-Zavadsky M., Prochaska J. X., D'Odorico S., 2002, Astronomy and Astrophysics, 391, 801
Dessauges-Zavadsky M., Prochaska J. X., D'Odorico S., Calura F., Matteucci F., 2006, Astronomy and Astrophysics, 445, 93
D'Odorico V. et al., 2013, Monthly Notices of the Royal Astronomical Society, 435, 1198
D'Odorico V., Molaro P., 2004, Astronomy and Astrophysics, 415, 879
Draine B., 2011, Physics of the Interstellar and Intergalactic Medium
Dutta R., Srianand R., Rahmani H., Petitjean P., Noterdaeme P., Ledoux C., 2014, Monthly Notices of the Royal Astronomical Society, 440, 307
Ellison S. L., Hennawi J. F., Martin C. L., Sommer-Larsen J., 2007, Monthly Notices of the Royal Astronomical Society, 378, 801
Ellison S. L., Kanekar N., Prochaska J. X., Momjian E., Worseck G., 2012, Monthly Notices of the Royal Astronomical Society, 424, 293
Ellison S. L., Lopez S., 2001, Astronomy and Astrophysics, 380, 117
Ellison S. L., Lopez S., 2009, Monthly Notices of the Royal Astronomical Society, 397, 467
Ellison S. L., Pettini M., Steidel C. C., Shapley A. E., 2001, The Astrophysical Journal, 549, 770
Ellison S. L., Prochaska J. X., Hennawi J., Lopez S., Usher C., Wolfe A. M., Russell D. M., Benn C. R., 2010, Monthly Notices of the Royal Astronomical Society, 406, no
Ellison S. L., York B. a., Pettini M., Kanekar N., 2008, Monthly Notices of the Royal Astronomical Society, 388, 1349
Erb D. K., Shapley A. E., Pettini M., Steidel C. C., Reddy N. a., Adelberger K. L., 2006, The Astrophysical Journal, 644, 813
Fall S. M., Efstathiou G., 1980, Royal Astronomical Society, 193, 189
Faucher-Giguere C.-A., Hopkins P. F., Kere D., Muratov A. L., Quataert E., Murray N., 2015, Monthly Notices of the Royal Astronomical Society, 449, 987
Faucher-Giguere C. A., Kereš D., 2011, Monthly Notices of the Royal Astronomical Society: Letters, 412
Fontana A., Ballester P., 1995, The Messenger, 80, 37
Fox A. J., Petitjean P., Ledoux C., Srianand R., 2007, 5
Fox A. J., Prochaska J. X., Ledoux C., Petitjean P., Wolfe A. M., Srianand R., 2009, 746, 26
Frank S., Péroux C., 2010, Monthly Notices of the Royal Astronomical Society, 406, 2235
Fumagalli M., Prochaska J. X., Kasen D., Dekel A., Ceverino D., Primack J. R., 2011, Monthly Notices of the Royal Astronomical Society, 418, 1796
Fynbo J. P. U. et al., 2013, Monthly Notices of the Royal Astronomical Society, 436, 361
Fynbo J. P. U. et al., 2011, Monthly Notices of the Royal Astronomical Society, 413, 2481
Gauthier J.-R., Chen H.-W., Cooksey K. L., Simcoe R. A., Seyffert E. N., O'Meara J. M., 2014, Monthly Notices of the Royal Astronomical Society, 439, 342
Ge J., Bechtold J., Kulkarni V. P., 2001, The Astrophysical Journal, 547, L1
Genel S., Bouché N., Naab T., Sternberg A., Genzel R.,

2010, The Astrophysical Journal, 719, 229
Guimarães R., Noterdaeme P., Petitjean P., Ledoux C., Srianand R., López S., Rahmani H., 2012, The Astronomical Journal, 143, 147
Haehnelt M. G., Steinmetz M., Rauch M., 1998, The Astrophysical Journal, 495, 647
Heinmueller J., Petitjean P., Ledoux C., Caucci S., Srianand R., 2006, 39, 33
Henry R. B. C., Prochaska J. X., 2007, Publications of the Astronomical Society of the Pacific, 119, 962
HerbertFort S., Prochaska J. X., DessaugesZavadsky M., Ellison S. L., Howk J. C., Wolfe A. M., Prochter G. E., 2006, Publications of the Astronomical Society of the Pacific, 118, 1077
Jenkins E. B., 2009, The Astrophysical Journal, 700, 1299
Kacprzak G. G. et al., 2014, The Astrophysical Journal, 792, L12
Kanekar N. et al., 2014, Monthly Notices of the Royal Astronomical Society, 438, 2131
Kereš D., Katz N., Weinberg D. H., Davé R., 2005, Monthly Notices of the Royal Astronomical Society, 363, 2
Khare P., Kulkarni V. P., Péroux C., York D. G., Lauroesch J. T., Meiring J. D., 2007, Astronomy and Astrophysics, 464, 487
Khare P., Vanden Berk D., York D. G., Lundgren B., Kulkarni V. P., 2012, Monthly Notices of the Royal Astronomical Society, 419, 1028
Kisielius R., Kulkarni V. P., Ferland G. J., Bogdanovich P., Lykins M. L., 2014, The Astrophysical Journal, 780, 76
Kisielius R., Kulkarni V. P., Ferland G. J., Bogdanovich P., Som D., Lykins M. L., 2015, The Astrophysical Journal, 804, 76
Krogager J.-K. et al., 2013, Monthly Notices of the Royal Astronomical Society, 433, 3091
Krogager J.-K., Fynbo J. P. U., Noterdaeme P., Zafar T., Møller P., Ledoux C., Krühler T., Stockton A., 2016, Monthly Notices of the Royal Astronomical Society, 455, 2698
Krogager J.-K. et al., 2015, The Astrophysical Journal Supplement Series, 217, 5
Kulkarni V. P., Fall S. M., Lauroesch J. T., York D. G., Welty D. E., Khare P., Truran J. W., 2005, The Astrophysical Journal, 618, 68
Kulkarni V. P., Khare P., Péroux C., York D. G., Lauroesch J. T., Meiring J. D., 2007, The Astrophysical Journal, 661, 88
Kulkarni V. P., Khare P., Som D., Meiring J., York D. G., Peroux C., Lauroesch J. T., 2010, 27
Kulkarni V. P., Meiring J., Som D., Péroux C., York D. G., Khare P., Lauroesch J. T., 2012, The Astrophysical Journal, 749, 176
Lanzetta K. M., Wolfe A. M., Turnshek D. A., 1995, The Astrophysical Journal, 440, 435
Ledoux C., Bergeron J., Petitjean P., 2002, European Space Agency, (Special Publication) ESA SP, 815, 17
Ledoux C., Petitjean P., Fynbo J. P. U., Møller P., Srianand R., 2006, Astronomy and Astrophysics, 457, 71
Ledoux C., Petitjean P., Srianand R., 2003, Monthly Notices of the Royal Astronomical Society, 346, 209
Ledoux C., Srianand R., Petitjean P., 2002, 789, 9
Lehner N. et al., 2013, The Astrophysical Journal, 770, 138
Lehner N., O'Meara J. M., Fox A. J., Howk J. C., Prochaska J. X., Burns V., Armstrong A. A., 2014, The Astrophysical Journal, 3
Lequeux J., Peimbert M., Rayo J. F., Serrano A., Torres-Peimbert S., 1979, Astronomy and Astrophysics, 80, 155
Lopez S., Ellison S. L., 2003, Astronomy and Astrophysics, 403, 573
Lopez S., Reimers D., D'Odorico S., Prochaska J. X., 2002, Astronomy and Astrophysics, 385, 778
Lopez S., Reimers D., Gregg M. D., Wisotzki L., Wucknitz O., Guzman A., 2005, The Astrophysical Journal, 626, 767
Lopez S., Reimers D., Rauch M., Sargent W. L. W., Smette A., 1999, 10, 49
Lu L., Sargent W. L. W., Barlow T. A., Galaxies D. L., Churchill C. W., Vogt S. S., 1996, The Astrophysical Journal Supplement Series, 107, 475
Lundgren B. F. et al., 2009, The Astrophysical Journal, 698, 819
Maddox N., Hewett P. C., Péroux C., Nestor D. B., Wisotzki L., 2012, Monthly Notices of the Royal Astronomical Society, 424, 2876
Malaney R. A., Chaboyer B., 1996, The Astrophysical Journal, 462, 57
Martin C. L., 2005, The Astrophysical Journal, 621, 227
Martin C. L., Shapley A. E., Coil A. L., Kornei K. a., Bundy K., Weiner B. J., Noeske K. G., Schiminovich D., 2012, The Astrophysical Journal, 760, 127
Martin D. C., Chang D., Matuszewski M., Morrissey P., Rahman S., Moore A., Steidel C. C., 2014, The Astrophysical Journal, 786, 106
Meiring J. D. et al., 2006, Monthly Notices of the Royal Astronomical Society, 370, 43
Meiring J. D., Lauroesch J. T., Kulkarni V. P., Péroux C., Khare P., York D. G., 2009a, Monthly Notices of the Royal Astronomical Society, 397, 2037
Meiring J. D., Lauroesch J. T., Kulkarni V. P., Peroux C., Khare P., York D. G., 2009b, Monthly Notices of the Royal Astronomical Society, 397, 2037
Meiring J. D., Lauroesch J. T., Kulkarni V. P., Péroux C., Khare P., York D. G., Crotts a. P. S., 2007, Monthly Notices of the Royal Astronomical Society, 376, 557
Meyer D. M., Lanzetta K. M., Wolfe A. M., 1995, The Astrophysical Journal, 451, 1
Milutinovic N., Ellison S. L., Prochaska J. X., Tumlinson J., 2010, Monthly Notices of the Royal Astronomical Society, 408, 2071
Molaro P., Bonifacio P., Centurion M., DOdorico S., Vladilo G., Santin P., Di Marcantonio P., 2000, The Astrophysical Journal, 541, 54
Moller P., Fynbo J. P. U., Ledoux C., Nilsson K. K., 2013, Monthly Notices of the Royal Astronomical Society, 430, 2680
Morton D. C., 2003, The Astrophysical Journal Supplement Series, 149, 205
Neeleman M., Wolfe A. M., Prochaska J. X., Rafelski M., 2013, The Astrophysical Journal, 769, 54
Nestor D. B., Pettini M., Hewett P. C., Rao S., Wild V., 2008, Monthly Notices of the Royal Astronomical Society, 390, 1670
Noterdaeme P. et al., 2012a, Astronomy & Astrophysics, 540, A63
Noterdaeme P., Ledoux C., Petitjean P., Le Petit F., Sri-

anand R., Smette A., 2007a, Astronomy and Astrophysics, 474, 393
Noterdaeme P., Ledoux C., Petitjean P., Srianand R., 2008a, Astronomy and Astrophysics, 481, 327
Noterdaeme P., López S., Dumont V., Ledoux C., Molaro P., Petitjean P., 2012b, Astronomy & Astrophysics, 542, L33
Noterdaeme P. et al., 2012c, Astronomy & Astrophysics, 547, L1
Noterdaeme P., Petitjean P., Ledoux C., Srianand R., Ivanchik a., 2008b, Astronomy and Astrophysics, 491, 397
Noterdaeme P., Petitjean P., Srianand R., Ledoux C., Le Petit F., 2007b, Astronomy and Astrophysics, 469, 425
Ocvirk P., Pichon C., Teyssier R., 2008, Monthly Notices of the Royal Astronomical Society, 390, 1326
O'Meara J. M. et al., 2015, Astronomical Journal
Oppenheimer B. D., Davé R., Kereš D., Fardal M., Katz N., Kollmeier J. a., Weinberg D. H., 2010, Monthly Notices of the Royal Astronomical Society, 406, 2325
Pei Y. C., Fall S. M., 1995, The Astrophysical Journal, 454, 69
Pei Y. C., Fall S. M., Hauser M. G., 1999, The Astrophysical Journal, 522, 604
Penprase B. E., Prochaska J. X., Sargent W. L. W., Toro-Martinez I., Beeler D. J., 2010, The Astrophysical Journal, 721, 1
Péroux C., Bouché N., Kulkarni V. P., York D. G., Vladilo G., 2011, Monthly Notices of the Royal Astronomical Society, 410, 2251
Péroux C., Dessauges-Zavadsky M., D'Odorico S., Kim T. S., McMahon R. G., 2005, Monthly Notices of the Royal Astronomical Society, 363, 479
Péroux C., Dessauges-Zavadsky M., D'Odorico S., Kim T. S., McMahon R. G., 2007, Monthly Notices of the Royal Astronomical Society, 382, 177
Péroux C., Kulkarni V. P., Meiring J., Ferlet R., Khare P., Lauroesch J. T., Vladilo G., York D. G., 2006a, Astronomy & Astrophysics, 450, 53
Péroux C., Kulkarni V. P., York D. G., 2014, Monthly Notices of the Royal Astronomical Society, 437, 3144
Péroux C., Meiring J. D., Kulkarni V. P., Ferlet R., Khare P., Lauroesch J. T., Vladilo G., York D. G., 2006b, Monthly Notices of the Royal Astronomical Society, 372, 369
Péroux C., Meiring J. D., Kulkarni V. P., Khare P., Lauroesch J. T., Vladilo G., York D. G., 2008, Monthly Notices of the Royal Astronomical Society, 386, 2209
Peroux C., Petitjean P., Aracil B., Srianand R., 2002, New Astronomy, 7, 1
Petitjean P., Ledoux C., Srianand R., 2008, Astronomy & Astrophysics, 480, 349
Petitjean P., Srianand R., Ledoux C., 2000, AA, 364, 26
Petitjean P., Srianand R., Ledoux C., 2002, Monthly Notices of the Royal Astronomical Society, 332, 9
Pettini M., Cooke R., 2012, Monthly Notices of the Royal Astronomical Society, 425, 2477
Pettini M., Ellison S. L., Bergeron J., Petitjean P., 2002, Astronomy and Astrophysics, 391, 21
Pettini M., Ellison S. L., Steidel C. C., Bowen D. V., 1999, The Astrophysical Journal, 510, 576
Pettini M., Ellison S. L., Steidel C. C., Shapley A. E., Bowen D. V., 2000, The Astrophysical Journal, 532, 65
Pettini M., King D. L., Smith L. J., Hunstead R. W., 1997a, The Astrophysical Journal, 478, 536
Pettini M., Smith L. J., Hunstead R. W., King D. L., 1994, Metal enrichment, dust, and star formation in galaxies at high redshifts. 3: Zn and CR abundances for 17 damped Lyman-alpha systems
Pettini M., Smith L. J., King D. L., Hunstead R. W., 1997b, The Astrophysical Journal, 486, 665
Pettini M., Zych B. J., Murphy M. T., Lewis A., Steidel C. C., 2008a, Monthly Notices of the Royal Astronomical Society, 391, 1499
Pettini M., Zych B. J., Steidel C. C., Chaffee F. H., 2008b, Monthly Notices of the Royal Astronomical Society, 385, 2011
Pontzen A. et al., 2008, Monthly Notices of the Royal Astronomical Society, 390, 1349
Prochaska J. X., Castro S., Djorgovski S. G., 2003, The Astrophysical Journal Supplement Series, 148, 317
Prochaska J. X., Gawiser E., Wolfe A. M., 2001, The Astrophysical Journal, 552, 99
Prochaska J. X., Gawiser E., Wolfe A. M., Cooke J., Gelino D., 2003, The Astrophysical Journal Supplement Series, 147, 227
Prochaska J. X., Henry R. B. C., OMeara J. M., Tytler D., Wolfe A. M., Kirkman D., Lubin D., Suzuki N., 2002, Publications of the Astronomical Society of the Pacific, 114, 933
Prochaska J. X., HerbertFort S., Wolfe A. M., 2005, The Astrophysical Journal, 635, 123
Prochaska J. X., Wolfe A. M., 1996, The Astrophysical Journal, 470, 403
Prochaska J. X., Wolfe A. M., 1997a, \Apj, 474, 140
Prochaska J. X., Wolfe A. M., 1997b, The Astrophysical Journal, 487, 73
Prochaska J. X., Wolfe A. M., 1999, The Astrophysical Journal Supplement Series, 121, 369
Prochaska J. X., Wolfe A. M., 2002, The Astrophysical Journal, 566, 68
Prochaska J. X., Wolfe A. M., 2009, The Astrophysical Journal, 696, 1543
Prochaska J. X., Wolfe A. M., Howk J. C., Gawiser E., Burles S. M., Cooke J., 2007, The Astrophysical Journal Supplement Series, 171, 29
Prochter G. E., Prochaska J. X., O'Meara J. M., Burles S., Bernstein R. a., 2010, The Astrophysical Journal, 20
Quast R., Reimers D., Baade R., 2008, Astronomy & Astrophysics, 457, 443
Rafelski M., Neeleman M., Fumagalli M., Wolfe A. M., Prochaska J. X., 2014, The Astrophysical Journal, 782, L29
Rafelski M., Wolfe A. M., Prochaska J. X., Neeleman M., Mendez A. J., 2012, The Astrophysical Journal, 755, 89
Rao S. M., Prochaska J. X., Howk J. C., Wolfe A. M., 2005, The Astronomical Journal, 129, 9
Rao S. M., Turnshek D. a., 2000, The Astrophysical Journal Supplement Series, 130, 1
Rao S. M., Turnshek D. a., Nestor D. B., 2006, The Astrophysical Journal, 636, 610
Rees M., Ostriker J., 1977, Monthly Notices of the Royal Astronomical Society, 179, 541
Richter P., Westmeier T., Bruens C., 2005, 52, 4
Rix S. a., Pettini M., Steidel C. C., Reddy N. a., Adelberger

K. L., Erb D. K., Shapley A. E., 2007, 27
Rubin K. H. R., Prochaska J. X., Koo D. C., Phillips A. C., Martin C. L., Winstrom L. O., 2014, The Astrophysical Journal, 794, 156
Rubin K. H. R., Xavier Prochaska J., Koo D. C., Phillips A. C., 2012, The Astrophysical Journal, 747, L26
Ryan-Weber E. V., Pettini M., Madau P., Zych B. J., 2009, Monthly Notices of the Royal Astronomical Society, 395, 1476
Saito Y.-j., Takada-Hidai M., Honda S., Takeda Y., 2009, Publications of the Astronomical Society of Japan, 61, 549
Savage B. D., Sembach K. R., 1996, Annual Review of Astronomy and Astrophysics, 34, 279
Savaglio S. et al., 2005, 1, 260
Schroetter I., Bouché N., Peroux C., Murphy M. T., Contini T., Finley H., 2015
Shapley a. E., Steidel C. C., Pettini M., Adelberger K. L., 2003, The Astrophysical Journal, 588, 65
Shen S., Madau P., Guedes J., Mayer L., Prochaska J. X., Wadsley J., 2013, The Astrophysical Journal, 765, 89
Shull J. M., Danforth C. W., Tilton E. M., 2014, The Astrophysical Journal, 796, 49
Shull J. M., Moloney J., Danforth C. W., Tilton E. M., 2015, The Astrophysical Journal, 811, 3
Silk J., 1977, The Astrophysical Journal, 211, 638
Simcoe R. a., Sargent W. L. W., Rauch M., 2004, The Astrophysical Journal, 606, 92
Som D., Kulkarni V. P., Meiring J., York D. G., Péroux C., Khare P., Lauroesch J. T., 2013, Monthly Notices of the Royal Astronomical Society, 435, 1469
Som D., Kulkarni V. P., Meiring J., York D. G., Péroux C., Lauroesch J. T., Aller M. C., Khare P., 2015, The Astrophysical Journal, 806, 25
Songaila A., Cowie L. L., 1996, The Astrophysical Journal, 112, 335
Songaila A., Cowie L. L., 2002, The Astronomical Journal, 123, 2183
Srianand R., Gupta N., Petitjean P., 2007, Monthly Notices of the Royal Astronomical Society, 375, 584
Srianand R., Gupta N., Petitjean P., Noterdaeme P., Ledoux C., Salter C. J., Saikia D. J., 2012, Monthly Notices of the Royal Astronomical Society, 421, no
Srianand R., Petitjean P., 1998, Astronomy & Astrophysics, 40, 33
Srianand R., Petitjean P., 2001, European Space Agency, (Special Publication) ESA SP, 826, 12
Srianand R., Petitjean P., Ledoux C., 2000, Nature, 408, 1
Srianand R., Petitjean P., Ledoux C., Ferland G., Shaw G., 2005, The VLT-UVES survey for molecular hydrogen in high-redshift damped Lyman a systems: Physical conditions in the neutral gas
Steidel C. C., Adelberger K. L., Shapley A. E., Pettini M., Dickinson M., Giavalisco M., 2000, The Astrophysical Journal, 532, 170
Steidel C. C., Dickinson M., Meyer D. M., Adelberger K. L., Sembach K. R., 1997, Astrophysical Journal, 480, 568
Steidel C. C., Erb D. K., Shapley A. E., Pettini M., Reddy N., Bogosavljević M., Rudie G. C., Rakic O., 2010, The Astrophysical Journal, 717, 289
Storrie-Lombardi L. J., Wolfe A. M., 2000, The Astrophysical Journal, 543, 46
Tchernyshyov K., Meixner M., Seale J., Fox A., Friedman S. D., Sembach K., Dwek E., 2015, The Astrophysical Journal, 811, 1
Timmes F. X., Lauroesch J. T., Truran J. W., 1995, 22
Tissera P. B., Mosconi D. G. L. M. B., Cora S. A., 2001, 20, 527
Tremonti C. A. et al., 2004, The Astrophysical Journal, 613, 15
Tripp T. M., Jenkins E. B., Bowen D. V., Prochaska J. X., Aracil B., Ganguly R., 2005, 714
Tumlinson J. et al., 2011, Science (New York, N.Y.), 334, 948
Turnshek D. A., Monier E. M., Rao S. M., Hamilton T. S., Sardane G. M., Held R., 2015, Monthly Notices of the Royal Astronomical Society, 449, 1536
Turnshek D. A., Rao S. M., Nestor D. B., Vanden Berk D., Belfort-Mihalyi M., Monier E. M., 2004, The Astrophysical Journal, 609, L53
van de Voort F., Schaye J., 2012, Monthly Notices of the Royal Astronomical Society, 423, 2991
van de Voort F., Schaye J., Altay G., Theuns T., 2012, Monthly Notices of the Royal Astronomical Society, 421, 2809
Vladilo G., 1998, The Astrophysical Journal, 493, 583
Vladilo G., Abate C., Yin J., Cescutti G., Matteucci F., 2011, Astronomy & Astrophysics, 530, A33
Vladilo G., Centurion M., Bonifacio P., Howk J. C., 2001, The Astrophysical Journal, 557, 1007
Vladilo G., Centurión M., Levshakov S. a., Péroux C., Khare P., Kulkarni V. P., York D. G., 2006, Astronomy and Astrophysics, 454, 151
Wallerstein G., 1962, The Astrophysical Journal Supplement Series, 6, 407
White S. D. M., Rees M. J., 1978, Monthly Notices of the Royal Astronomical Society, 183, 341
Wolfe A. M., Gawiser E., Prochaska J. X., 2005, Annual Review of Astronomy and Astrophysics, 43, 861
Zafar T., Centurion M., Peroux C., Molaro P., D'Odorico V., Vladilo G., Popping A., 2014a, 16, 16
Zafar T., Péroux C., Popping A., Milliard B., Deharveng J.-M., Frank S., 2013, Astronomy & Astrophysics, 556, A141
Zafar T., Popping A., Péroux C., 2013, Astronomy & Astrophysics, 556, A140
Zafar T., Vladilo G., Peroux C., Molaro P., Centurion M., D'Odorico V., Abbas K., Popping A., 2014b, Monthly Notices of the Royal Astronomical Society, 14
Zafar T., Watson D., Fynbo J. P. U., Malesani D., Jakobsson P., de Ugarte Postigo A., 2011, Astronomy & Astrophysics, 532, A143
Zwaan M., Walter F., Ryan-Weber E., Brinks E., de Blok W. J. G., Kennicutt R. C., 2008, The Astronomical Journal, 136, 2886
Zych B. J., Murphy M. T., Hewett P. C., Prochaska J. X., 2009, Monthly Notices of the Royal Astronomical Society, 392, 1429

APPENDIX A: MULTI-ELEMENT ANALYSIS

A1 Derivation of F_*

Jenkins (2009) proposed to use the abundances of different elements (namely C, N, O, Mg, Si, P, Cl, Ti, Cr, Mn, Fe, Ni, Cu, Zn, Ge, Kr and S) to compare the dust depletion of dense neutral hydrogen systems to that of the Interstellar Medium (ISM) of our Galaxy. Specifically, the depletion $[X_{gas}/H]$ described in Jenkins (2009) is the difference between the observed abundance of element X normalized to the total hydrogen abundance in both neutral and molecular phases, $N(H) = N(H\,I)+2N(H_2)$, and its intrinsic abundance (assumed to be solar, initially):

$$[X_{gas}/H] = \log(X/H)_{obs} - \log(X/H)_{\odot} \quad (A1)$$

Using 243 sight lines in our Galaxy, Jenkins (2009) linearly fits the following formula:

$$[X_{gas}/H]_{fit} = [X_{gas}/H]_0 + A_X F_* \quad (A2)$$

where F_* is defined as the line-of-sight depletion factor[4], A_X as the propensity of the element X to increase the absolute value of its particular depletion level as F_* becomes larger and $[X_{gas}/H]_0$ as the depletion for element X when $F_* = 0$. This equation can linearly be rewritten as:

$$[X_{gas}/H]_{fit} = B_X + A_X(F_* - z_X) \quad (A3)$$

where F_* has its zero-point reference displaced to an intermediate value z_X (unique to element X), B_X being the depletion at $F_* = z_X$. The three parameters, A_X B_X and z_X, are then solved for each element (Table 4 of Jenkins 2009).

In the case of DLAs and sub-DLAs[5], releasing the hypothesis of solar metallicity, equation A1 can be rewritten as follows:

$$[X_{gas}/H] = \log(X/H)_{obs} - \log(X/H)_{intrinsic} \quad (A4)$$

where $\log(X/H)_{intrinsic}$ is the abundance of element X in the absence of depletion. Equation A3 then becomes:

$$[X/H]_{obs} - B_X + A_X z_X = [X/H]_{intrinsic} + A_X F_* \quad (A5)$$

where $[X/H]_{obs}$ is the metallicity compared to solar as we measure it (hence affected by depletion) and $[X/H]_{intrinsic}$ is the intrinsic metallicity compared to solar of the system derived from element X (corrected for depletion). We derive F_* by linearly fitting the left hand side of equation A5 as a function of A_X, thus providing an estimate of the intrinsic metallicity.

A2 Derivation of A_V

Our study relates to the rest frame extinction A_V through equation 3 of Vladilo et al. (2006), which scales A_V to the dust-phase column density of iron $\widehat{N_{Fe}}$. Assuming that zinc is completely undepleted, and that the intrinsic ratio Zn/Fe ratio in DLAs and sub-DLAs is solar, we can express $\widehat{N_{Fe}}$ as the following:

$$\widehat{N_{Fe}} = f_{Fe} N_{Zn} \left(\frac{Fe}{Zn}\right)_{\odot} \quad (A6)$$

where $f_{Fe} = 1 - 10^{\delta_{Fe}}$ is the fraction of iron in dust form. We can assume $\delta_{Fe} = [Fe/Zn]_{obs}$. To recover N_{Zn}, we use the assumption that [Zn/H] = [X/H], with [X/H] being the metallicity derived for each system using the ion X (when Zn is not detected). We obtain the following expression:

$$\log \widehat{N_{Fe}} = \log\left(1 - 10^{[Fe/Zn]_{obs}}\right) + \log(N_X) - \log\left(\frac{N_X}{N_{Fe}}\right)_{\odot} \quad (A7)$$

where N_X is the column density of the ion used for the metallicity derivation for a given system.

We can use equation A5 to derive an estimate of the quantity $[Fe/Zn]_J$ from the Jenkins analysis:

$$[Fe/Zn]_J = (-1.01 \pm 0.07) + (-0.68 \pm 0.08)F_* \quad (A8)$$

This results in $\langle[Fe/Zn]\rangle_{J,\,sub-DLA} = -0.78 \pm 0.15$ and $\langle[Fe/Zn]\rangle_{J,\,DLA} = -0.53 \pm 0.10$. Using a bootstrap method, we derive $\left\langle \log \widehat{N_{Fe}} \right\rangle_{sub-DLA} = 14.38 \pm 0.80$ and $\left\langle \log \widehat{N_{Fe}} \right\rangle_{DLA} = 14.73 \pm 0.85$. Based on Fig. 4 from Vladilo et al. (2006), we can estimate the rest frame extinction $\log A_V$ from $\log \widehat{N_{Fe}}$. For both populations, the value of $\left\langle \log \widehat{N_{Fe}} \right\rangle$ falls below the range of MW data used to derive the correlation, giving low values of $\langle \log A_V \rangle \lesssim -2$ mag. This suggests that the dust reddening is not observed in the current quasar selection.

APPENDIX B: SAMPLE

This Appendix presents the full list of damped and sub-damped absorbers identified in the EUADP+. We compile estimates of abundances from various references in the literature, as specified in the last column. We list the column density of ZnII, FeII and SII, as well as estimates of their metallicity based on the ion specified. The online version of this table includes a more complete list of ions.

[4] We stress that this definition is based on calibration of F_* against the descriptive summary definitions reported in the review article by Savage & Sembach (1996).

[5] We note that the measured molecular hydrogen fraction for DLAs is rather low and that this fraction is not correlated with the HI column density (Ledoux, Petitjean & Srianand 2003; Noterdaeme et al. 2008a). Therefore, the definition $N(H) = N(H\,I) + 2N(H_2)$ still holds for the present study.

Table B1: Full list of damped and sub-damped absorbers identified in the EUADP+, with the column densities of ZnII, FeII and SII, as well as estimates of their metallicity based on the ion specified.

QSO name	$z_{\rm abs}$	log N(HI)	log N(Zn)	log N(Fe)	log N(S)	[X/H]	X	Ref
CTQ418	2.5100	20.50 ± 0.07	-	14.07 ± 0.03	13.99 ± 0.06	-1.63 ± 0.09	SII	43
CTQ418	2.4300	20.68 ± 0.07	-	13.91 ± 0.05	13.97 ± 0.03	-1.83 ± 0.08	SII	43
QXO0001	3.0000	20.70 ± 0.05	-	< 15.09	-	-1.62 ± 0.05	OI	92
Q0000-262	3.3900	21.41 ± 0.08	12.01 ± 0.05	14.87 ± 0.03	-	-1.96 ± 0.09	ZnII	62, 90
QSO J0003-2323	2.1870	19.60 ± 0.40	< 11.04	13.22 ± 0.12	< 13.12	-1.76 ± 0.42	OI	103
Q0005+0524	0.8514	19.08 ± 0.04	< 11.24	13.79 ± 0.01	-	-0.47 ± 0.18	FeII	60
PSS0007+2417	3.5000	21.10 ± 0.10	< 12.39	> 14.63	-	-1.53 ± 0.11	SiII	94
PSS0007+2417	3.8400	20.85 ± 0.15	-	13.91 ± 0.03	-	-2.12 ± 0.24	FeII	94
J0007+0041	4.7300	20.65 ± 0.20	-	-	-	-2.19 ± 0.20	SiII	99
QSO J0008-2900	2.2540	20.22 ± 0.10	< 11.68	13.78 ± 0.01	-	-1.33 ± 0.14	SiII	114
QSO J0008-2901	2.4910	19.94 ± 0.11	< 12.12	13.65 ± 0.02	13.68 ± 0.18	-1.32 ± 0.26	OI	114
J0008-0958	1.7700	20.85 ± 0.15	13.31 ± 0.05	15.62 ± 0.05	15.84 ± 0.05	-0.10 ± 0.16	ZnII	44, 3, 4, 5
LBQS 0009-0138	1.3860	20.26 ± 0.02	< 11.55	14.25 ± 0.01	-	-1.32 ± 0.04	SiII	60
LBQS 0010-0012	2.0250	20.95 ± 0.10	12.19 ± 0.05	15.18 ± 0.03	14.98 ± 0.05	-1.32 ± 0.11	ZnII	52, 110
Q0012-0122	1.3862	20.26 ± 0.02	< 11.55	14.24 ± 0.01	-	-1.34 ± 0.08	SiII	60
LBQS 0013-0029	1.9730	20.83 ± 0.05	12.74 ± 0.05	14.81 ± 0.03	15.28 ± 0.03	-0.65 ± 0.07	ZnII	76, 110, 44
LBQS 0018+0026	0.5200	19.54 ± 0.03	-	13.17 ± 0.04	-	-1.55 ± 0.19	FeII	32
LBQS 0018+0026	0.9400	19.38 ± 0.15	< 11.64	14.62 ± 0.04	-	0.06 ± 0.24	FeII	32
J001855-091351	0.5840	20.11 ± 0.10	< 12.41	13.87 ± 0.03	-	-1.42 ± 0.21	FeII	114
Q0019-15	3.4400	20.92 ± 0.10	-	> 14.79	-	-1.01 ± 0.11	SiII	89, 90
Q0021+0104	1.3259	20.04 ± 0.11	< 11.48	14.69 ± 0.01	-	-0.53 ± 0.21	FeII	60
Q0021+0104	1.5756	20.48 ± 0.15	< 11.95	14.61 ± 0.02	-	-1.11 ± 0.15	SiII	60
J0021+0043	0.9424	19.38 ± 0.13	< 11.64	15.06 ± 0.14	-	0.50 ± 0.26	FeII	26
QSO B0027-1836	2.4020	21.75 ± 0.10	12.79 ± 0.02	14.97 ± 0.02	15.23 ± 0.02	-1.52 ± 0.10	ZnII	64
J0035-0918	2.3400	20.55 ± 0.10	-	13.07 ± 0.04	< 13.13	-2.69 ± 0.17	OI	17
QSO B0039-3354	2.2240	20.60 ± 0.10	-	14.41 ± 0.03	-	-1.27 ± 0.11	SiII	66
J004054.7-091526	4.7400	20.55 ± 0.15	-	14.05 ± 0.06	-	-1.93 ± 0.15	SiII	98
J0040-0915	4.7394	20.30 ± 0.15	-	14.05 ± 0.06	-	-1.43 ± 0.24	FeII	98
QSO J0041-4936	2.2480	20.46 ± 0.13	11.70 ± 0.10	14.42 ± 0.04	< 14.82	-1.32 ± 0.16	ZnII	114
LBQS 0042-2930	1.8090	20.40 ± 0.10	-	-	-	-1.21 ± 0.12	SiII	37
LBQS 0042-2930	1.9360	20.50 ± 0.10	-	-	-	-1.23 ± 0.11	SiII	37
J0044+0018	1.7300	20.35 ± 0.10	< 12.61	> 14.77	15.27 ± 0.05	-0.20 ± 0.11	SII	3, 4, 5
Q0049-2820	2.0700	20.45 ± 0.10	-	14.50 ± 0.02	-	-1.26 ± 0.11	SiII	67
QSO B0058-292	2.6710	21.10 ± 0.10	12.23 ± 0.05	14.75 ± 0.03	14.92 ± 0.03	-1.43 ± 0.11	ZnII	51, 110
J0058+0115	2.0100	21.10 ± 0.15	12.95 ± 0.05	15.18 ± 0.05	15.40 ± 0.05	-0.71 ± 0.16	ZnII	3, 4, 5
QSO B0100+1300	2.3090	21.35 ± 0.08	12.49 ± 0.02	15.10 ± 0.04	15.09 ± 0.06	-1.42 ± 0.08	ZnII	89, 22
QSO J0105-1846	2.3700	21.00 ± 0.08	11.77 ± 0.11	14.47 ± 0.10	14.30 ± 0.04	-1.79 ± 0.14	ZnII	51, 110
QSO J0105-1846	2.9260	20.00 ± 0.10	-	13.80 ± 0.03	13.82 ± 0.03	-1.56 ± 0.13	OI	66
B0105-008	1.3700	21.70 ± 0.15	12.93 ± 0.04	15.59 ± 0.03	-	-1.33 ± 0.16	ZnII	35
QSO B0112-30	2.4180	20.50 ± 0.08	-	13.33 ± 0.04	14.44 ± 0.03	-2.24 ± 0.11	OI	77
QSO B0112-30	2.7020	20.30 ± 0.10	-	14.77 ± 0.07	-	-0.44 ± 0.13	SiII	51, 110
Q0112+030	2.4200	20.90 ± 0.10	-	14.85 ± 0.01	14.79 ± 0.05	-1.23 ± 0.11	SII	110, 52, 67
QSO B0122-005	1.7610	20.78 ± 0.07	-	15.10 ± 0.10	-	-0.87 ± 0.11	SiII	33
QSO B0122-005	2.0100	20.04 ± 0.07	< 11.40	13.69 ± 0.07	-	-1.88 ± 0.09	SiII	33
QSO J0123-0058	1.4090	20.08 ± 0.09	12.23 ± 0.10	14.98 ± 0.02	-	-0.41 ± 0.13	ZnII	74
QSO J0124+0044	2.9880	19.18 ± 0.10	-	< 13.55	< 14.27	-0.57 ± 0.16	SiII	73
QSO J0124+0044	3.0780	20.21 ± 0.10	-	< 14.13	-	-0.59 ± 0.40	SiII	73
QSO B0128-2150	1.8570	20.21 ± 0.09	< 12.26	14.44 ± 0.01	14.33 ± 0.03	-1.00 ± 0.09	SII	114
J013209-082349	0.6470	20.60 ± 0.12	-	14.96 ± 0.07	-	-0.82 ± 0.23	FeII	114
QSO J0133+0400	3.6920	20.68 ± 0.15	-	13.51 ± 0.07	-	-0.96 ± 0.16	SiII	93
QSO J0133+0400	3.7730	20.55 ± 0.13	< 13.10	> 14.87	-	-0.59 ± 0.13	SiII	93
QSO J0133+0400	3.9950	19.94 ± 0.15	-	< 13.43	-	-1.54 ± 0.20	SiII	73
PSS0133+0400	3.6900	20.70 ± 0.10	-	13.57 ± 0.04	< 13.35	-2.31 ± 0.21	FeII	93, 77

Continued on next page

Table B1 – *Continued from previous page*

QSO name	$z_{\rm abs}$	log N(HI)	log N(Zn)	log N(Fe)	log N(S)	[X/H]	X	Reference
PSS0133+0400	3.7700	20.60 ± 0.10	< 13.10	> 14.87	-	-0.65 ± 0.10	SiII	93, 67
QSO J0134+0051	0.8420	19.93 ± 0.13	< 12.17	14.47 ± 0.01	-	-0.64 ± 0.22	FeII	72
PSS0134+3317	3.7600	20.85 ± 0.08	-	-	-	-2.69 ± 0.09	AlII	93
QSO B0135-42	3.1010	19.81 ± 0.10	-	13.67 ± 0.11	-	-1.21 ± 0.27	SiII	73
QSO B0135-42	3.6650	19.11 ± 0.10	-	< 13.47	-	-2.42 ± 0.16	OI	73
Q0135-273	2.8000	21.00 ± 0.10	-	14.77 ± 0.03	14.80 ± 0.02	-1.32 ± 0.10	SII	110, 52, 67
Q0135-273	2.1100	20.30 ± 0.15	-	-	14.38 ± 0.06	-1.04 ± 0.16	SII	52
QSO J0138-0005	0.7820	19.81 ± 0.09	12.69 ± 0.05	< 15.17	-	0.32 ± 0.10	ZnII	74
J0140-0839	3.7000	20.75 ± 0.15	-	< 12.73	< 13.33	-2.75 ± 0.15	OI	34
UM673A	1.6300	20.70 ± 0.10	11.43 ± 0.15	14.59 ± 0.03	14.53 ± 0.00	-1.83 ± 0.18	ZnII	15
J0142+0023	3.3500	20.38 ± 0.05	< 11.50	13.70 ± 0.10	13.26 ± 0.06	-2.24 ± 0.08	SII	34
Q0149+33	2.1400	20.50 ± 0.10	11.50 ± 0.10	14.20 ± 0.02	< 14.80	-1.56 ± 0.14	ZnII	89, 11, 90
Q0151+0448	1.9300	20.36 ± 0.10	< 11.81	13.70 ± 0.01	< 13.47	-1.86 ± 0.11	SiII	34, 118
QSO J0157-0048	1.4160	19.90 ± 0.07	12.12 ± 0.07	14.57 ± 0.03	-	-0.34 ± 0.10	ZnII	32
QSO B0201+113	3.3850	21.26 ± 0.08	-	15.35 ± 0.05	15.21 ± 0.11	-1.17 ± 0.14	SII	29
Q0201+365	2.4600	20.38 ± 0.05	12.47 ± 0.05	15.01 ± 0.01	15.29 ± 0.01	-0.47 ± 0.07	ZnII	87, 79, 90, 92, 3, 4, 5
Q0201+1120	3.3900	21.26 ± 0.10	-	15.35 ± 0.10	15.21 ± 0.10	-1.17 ± 0.14	SII	29
QSO J0209+0517	3.6660	20.47 ± 0.10	-	13.63 ± 0.05	-	-2.01 ± 0.21	FeII	93
QSO J0209+0517	3.8630	20.55 ± 0.10	-	< 13.34	-	-2.60 ± 0.11	SiII	93
PSS0209+0517	3.6700	20.45 ± 0.10	-	13.64 ± 0.05	-	-1.99 ± 0.21	FeII	93
J0211+1241	2.6000	20.60 ± 0.15	-	15.06 ± 0.05	-	-0.58 ± 0.17	SiII	3, 4, 5
QSO B0216+0803	1.7690	20.20 ± 0.10	11.90 ± 0.06	14.53 ± 0.09	-	-0.86 ± 0.12	ZnII	57
QSO B0216+0803	2.2930	20.45 ± 0.16	12.47 ± 0.05	14.88 ± 0.02	15.04 ± 0.02	-0.54 ± 0.17	ZnII	57, 117
QSO J0217+0144	1.3450	19.89 ± 0.09	-	14.38 ± 0.10	-	-1.11 ± 0.10	MgII	6, 7
SDSS0225+0054	2.7100	21.00 ± 0.15	12.89 ± 0.11	15.30 ± 0.08	-	-0.67 ± 0.19	ZnII	44
J0233+0103	1.7900	20.60 ± 0.15	-	14.62 ± 0.05	-	-1.34 ± 0.16	SiII	3, 4, 5
J0234-0751	2.3200	20.90 ± 0.10	-	14.18 ± 0.03	14.18 ± 0.03	-1.84 ± 0.10	SII	28
AO0235+164	0.5200	21.70 ± 0.10	-	15.30 ± 0.40	-	-1.58 ± 0.45	FeII	13
QSO B0237-2322	1.3650	19.30 ± 0.30	-	14.13 ± 0.01	-	0.08 ± 0.30	SiII	111
QSO B0237-2322	1.6720	19.65 ± 0.10	11.84 ± 0.09	14.57 ± 0.02	-	-0.37 ± 0.13	ZnII	35
Q0242-2917	2.5600	20.90 ± 0.10	-	14.36 ± 0.03	14.11 ± 0.02	-1.91 ± 0.10	SII	67
QSO B0244-1249	1.8630	19.48 ± 0.18	< 11.50	< 13.90	-	-0.79 ± 0.27	SiII	33
QSO B0253+0058	0.7250	20.70 ± 0.17	13.19 ± 0.04	15.13 ± 0.30	-	-0.07 ± 0.17	ZnII	72
QSO B0254-404	2.0460	20.45 ± 0.08	-	14.17 ± 0.03	14.14 ± 0.04	-1.43 ± 0.09	SII	66
J0255+00	3.9200	21.30 ± 0.05	-	14.75 ± 0.09	14.72 ± 0.01	-1.70 ± 0.05	SII	90
J0255+00	3.2500	20.70 ± 0.10	-	14.76 ± 0.01	-	-0.89 ± 0.11	SiII	90
Q0300-3152	2.1800	20.80 ± 0.10	-	14.21 ± 0.02	14.20 ± 0.03	-1.72 ± 0.10	SII	67
Q0302-223	1.0100	20.36 ± 0.11	12.45 ± 0.06	14.67 ± 0.05	-	-0.47 ± 0.13	ZnII	82
QSO B0307-195B	1.7880	19.00 ± 0.10	< 12.18	14.48 ± 0.00	-	0.49 ± 0.10	SiII	114
J0307-4945	4.4700	20.67 ± 0.09	-	14.21 ± 0.17	< 15.46	-1.45 ± 0.19	OI	20
TXS0311+430	2.2900	20.30 ± 0.00	< 12.50	14.85 ± 0.20	-	-0.63 ± 0.27	FeII	32, 32
J0311-1722	3.7300	20.30 ± 0.06	-	< 13.76	-	-2.29 ± 0.10	OI	16
QSO J0332-4455	2.6560	19.82 ± 0.05	-	13.51 ± 0.05	-	-1.67 ± 0.06	OI	36
QSO B0335-122	3.1780	20.65 ± 0.07	< 12.25	13.70 ± 0.04	-	-2.44 ± 0.10	SiII	1, 67
QSO B0336-017	3.0620	21.20 ± 0.09	-	14.90 ± 0.03	14.99 ± 0.01	-1.33 ± 0.09	SII	90
0338-0005	2.9090	21.10 ± 0.10	< 12.47	15.02 ± 0.06	15.19 ± 0.01	-1.03 ± 0.10	SII	95
QSO B0347-383	3.0250	20.63 ± 0.09	12.23 ± 0.12	14.47 ± 0.01	14.73 ± 0.01	-0.96 ± 0.15	ZnII	90, 51
QSO J0354-2724	1.4050	20.18 ± 0.15	12.73 ± 0.03	15.10 ± 0.03	-	-0.01 ± 0.15	ZnII	59
B0405-331	2.5700	20.60 ± 0.10	< 12.74	14.31 ± 0.00	-	-1.40 ± 0.10	SiII	1
Q0405-443	2.5500	21.13 ± 0.10	12.44 ± 0.05	14.95 ± 0.06	14.82 ± 0.06	-1.25 ± 0.11	ZnII	55, 110
Q0405-443	2.6200	20.47 ± 0.10	-	13.60 ± 0.02	< 14.34	-1.97 ± 0.10	OI	55, 110, 68, 112
QSO J0407-4410	1.9130	20.80 ± 0.10	12.44 ± 0.05	-	-	-0.92 ± 0.11	ZnII	52
QSO J0407-4410	2.5510	21.13 ± 0.10	12.44 ± 0.05	14.95 ± 0.06	14.82 ± 0.06	-1.25 ± 0.11	ZnII	55, 110

Continued on next page

Table B1 – *Continued from previous page*

QSO name	$z_{\rm abs}$	log N(HI)	log N(Zn)	log N(Fe)	log N(S)	[X/H]	X	Reference
QSO J0407-4410	2.5950	21.09 ± 0.10	12.68 ± 0.02	15.15 ± 0.02	15.19 ± 0.05	-0.97 ± 0.10	ZnII	55, 110
QSO J0407-4410	2.6210	20.45 ± 0.10	-	13.60 ± 0.02	< 14.34	-1.95 ± 0.10	OI	55, 110
Q0421-2624	2.1600	20.65 ± 0.10	-	13.97 ± 0.01	-	-1.81 ± 0.10	SiII	67
QSO J0422-3844	3.0820	19.37 ± 0.02	-	13.96 ± 0.10	-	-0.69 ± 0.04	OI	10
Q0425-5214	2.2200	20.30 ± 0.10	-	13.96 ± 0.03	14.07 ± 0.03	-1.35 ± 0.10	SII	67
BRJ0426-2202	2.9800	21.50 ± 0.15	< 12.17	14.15 ± 0.07	-	-2.53 ± 0.24	FeII	93
QSO J0427-1302	1.5620	19.35 ± 0.10	< 11.75	12.23 ± 0.04	-	-2.30 ± 0.21	FeII	114
QSO J0427-1302	1.4080	19.04 ± 0.04	< 11.09	13.33 ± 0.02	-	-0.99 ± 0.06	SiII	60
Q0432-4401	2.3000	20.95 ± 0.10	< 12.20	14.87 ± 0.10	-	-1.18 ± 0.12	SiII	1, 67, 119
QSO B0438-43	2.3470	20.78 ± 0.12	12.72 ± 0.03	-	-	-0.62 ± 0.12	ZnII	1
PKS 0439-433	0.1012	19.63 ± 0.15	-	14.92 ± 0.03	15.03 ± 0.03	0.28 ± 0.15	SII	105
QSO B0449-1645	1.0070	20.98 ± 0.07	12.62 ± 0.07	15.09 ± 0.01	-	-0.92 ± 0.10	ZnII	74
QSO B0450-1310B	2.0670	20.50 ± 0.07	-	14.29 ± 0.03	14.18 ± 0.06	-2.13 ± 0.08	OI	24, 119
PKS 0454-220	0.4740	19.45 ± 0.03	-	14.71 ± 0.01	15.06 ± 0.04	0.49 ± 0.05	SII	114
Q0454+039	0.8600	20.69 ± 0.06	12.33 ± 0.08	-	-	-0.92 ± 0.10	ZnII	82
4C-02.19	2.0400	21.70 ± 0.10	13.13 ± 0.05	15.38 ± 0.05	-	-1.13 ± 0.11	ZnII	42
QSO B0512-3329	0.9310	20.49 ± 0.08	-	14.47 ± 0.06	-	-1.20 ± 0.21	FeII	56
QSO B0515-4414	1.1510	19.88 ± 0.05	12.22 ± 0.04	14.31 ± 0.03	-	-0.22 ± 0.06	ZnII	97, 122
HE0512-3329A	0.9300	20.49 ± 0.08	-	14.47 ± 0.06	-	-1.20 ± 0.21	FeII	56
HE0515-4414	1.1500	20.45 ± 0.15	12.11 ± 0.04	14.31 ± 0.20	-	-0.90 ± 0.16	ZnII	123
QSO B0528-2505	2.1410	20.70 ± 0.08	13.00 ± 0.03	14.94 ± 0.26	14.83 ± 0.04	-0.26 ± 0.09	ZnII	57, 12
QSO B0528-2505	2.8110	21.11 ± 0.07	13.27 ± 0.03	15.47 ± 0.02	15.56 ± 0.02	-0.40 ± 0.08	ZnII	107, 57, 12
QSO B0551-36	1.9620	20.50 ± 0.08	13.02 ± 0.05	15.05 ± 0.05	15.38 ± 0.11	-0.04 ± 0.09	ZnII	49
J060008.1-504036	2.1490	20.40 ± 0.12	12.11 ± 0.03	14.84 ± 0.03	-	-0.85 ± 0.12	ZnII	114
QSO B0642-5038	2.6590	20.95 ± 0.08	12.50 ± 0.06	15.10 ± 0.04	-	-1.01 ± 0.10	ZnII	66, 119
Q0738+313	0.0900	21.18 ± 0.06	< 12.66	15.02 ± 0.15	-	-1.34 ± 0.24	FeII	58, 47
HS0741+4741	3.0200	20.48 ± 0.10	-	14.05 ± 0.01	14.00 ± 0.02	-1.60 ± 0.10	SII	90, 92
J0747+4434	4.0196	20.95 ± 0.15	-	> 14.32	-	-2.50 ± 0.20	NiII	98
FJ0747+2739	3.9000	20.50 ± 0.10	< 12.40	< 13.80	< 14.36	-1.98 ± 0.10	SiII	93
J0759+1800	4.6577	20.85 ± 0.15	-	< 15.16	14.26 ± 0.05	-1.71 ± 0.16	SII	98
SDSS0759+3129	3.0300	20.60 ± 0.10	-	13.80 ± 0.20	-	-2.01 ± 0.32	SiII	70
PSSJ0808+52	3.1100	20.65 ± 0.07	< 12.13	14.17 ± 0.04	-	-1.56 ± 0.14	SiII	91, 93
FJ0812+32	2.0700	21.00 ± 0.10	12.21 ± 0.02	14.89 ± 0.02	-	-1.35 ± 0.10	ZnII	95, 43
FJ0812+32	2.6300	21.35 ± 0.10	13.15 ± 0.05	15.09 ± 0.05	15.63 ± 0.07	-0.76 ± 0.11	ZnII	93, 95, 3, 4, 5
J0815+1037	1.8500	20.30 ± 0.15	-	> 14.87	-	-0.43 ± 0.47	SiII	3, 4, 5
J0816+1446	3.2900	22.00 ± 0.10	13.53 ± 0.00	15.89 ± 0.00	-	-1.03 ± 0.10	ZnII	41
J0817+1351	4.2584	21.30 ± 0.15	-	15.45 ± 0.06	15.30 ± 0.02	-1.12 ± 0.15	SII	98
J0824+1302	4.4700	20.65 ± 0.20	-	13.60 ± 0.08	-	-2.32 ± 0.21	SiII	99
J0825+3544	3.2073	20.30 ± 0.10	-	13.77 ± 0.03	-	-1.71 ± 0.21	FeII	98
J0825+3544	3.6567	21.25 ± 0.10	-	> 14.65	-	-1.83 ± 0.13	SiII	98
J0825+5127	3.3180	20.85 ± 0.10	-	14.22 ± 0.01	-	-1.67 ± 0.14	SiII	98
Q0826-2230	0.9110	19.04 ± 0.04	12.71 ± 0.08	13.57 ± 0.06	-	1.11 ± 0.09	ZnII	60
Q0827+243	0.5200	20.30 ± 0.05	< 12.80	14.59 ± 0.02	-	-0.89 ± 0.19	FeII	58, 45
J0831+4046	4.3440	20.75 ± 0.15	-	13.79 ± 0.07	-	-2.36 ± 0.15	SiII	98
J0834+2140	3.7102	20.85 ± 0.10	-	14.44 ± 0.02	-	-1.59 ± 0.21	FeII	98
J0834+2140	4.3900	21.00 ± 0.20	-	14.76 ± 0.02	14.85 ± 0.04	-1.27 ± 0.20	SII	98
J0834+2140	4.4610	20.30 ± 0.15	-	13.71 ± 0.07	< 14.13	-1.86 ± 0.16	SiII	98
Q0836+11	2.4700	20.58 ± 0.10	< 12.12	14.68 ± 0.01	< 14.66	-1.10 ± 0.11	SiII	90, 92
J0839+3524	4.2800	20.30 ± 0.15	-	14.30 ± 0.04	-	-1.18 ± 0.24	FeII	98
QSO B0841+129	1.8640	21.00 ± 0.10	-	-	14.82 ± 0.05	-1.30 ± 0.11	SII	52
QSO B0841+129	2.3750	21.05 ± 0.10	12.12 ± 0.05	14.76 ± 0.11	14.69 ± 0.15	-1.50 ± 0.11	ZnII	89, 119
QSO B0841+129	2.4760	20.80 ± 0.10	11.69 ± 0.05	14.43 ± 0.03	14.48 ± 0.12	-1.67 ± 0.11	ZnII	89, 24
SDSS0844+5153	2.7700	21.45 ± 0.15	-	15.29 ± 0.06	-	-0.99 ± 0.15	SiII	44
J0900+42	3.2500	20.30 ± 0.10	-	14.54 ± 0.01	14.65 ± 0.01	-0.77 ± 0.10	SII	95, 43
J0909+3303	3.6584	20.55 ± 0.10	-	14.43 ± 0.01	14.51 ± 0.04	-1.16 ± 0.11	SII	98
QSO B0913+0715	2.6180	20.35 ± 0.10	< 11.90	12.99 ± 0.01	13.88 ± 0.03	-2.41 ± 0.10	OI	84, 77

Continued on next page

Table B1 – *Continued from previous page*

QSO name	$z_{\rm abs}$	log N(HI)	log N(Zn)	log N(Fe)	log N(S)	[X/H]	X	Reference
B0913+003	2.7400	20.74 ± 0.10	< 12.82	14.60 ± 0.00	-	-1.47 ± 0.10	SiII	1
Q0918+1636	2.4100	21.26 ± 0.06	13.23 ± 0.18	15.51 ± 0.23	-	-0.59 ± 0.19	ZnII	39
Q0918+1636	2.5800	20.96 ± 0.05	13.40 ± 0.01	15.43 ± 0.01	15.82 ± 0.01	-0.12 ± 0.05	ZnII	38
J0925+4004	0.2477	19.55 ± 0.15	-	14.22 ± 0.09	< 14.72	-0.29 ± 0.17	OI	2
J0927+5823	1.6400	20.40 ± 0.25	13.29 ± 0.05	> 15.27	15.61 ± 0.05	0.33 ± 0.25	ZnII	3, 4, 5
J0928+6025	0.1538	19.35 ± 0.15	-	14.90 ± 0.08	< 14.65	0.37 ± 0.25	FeII	2
SDSS0928+0939	2.9100	20.75 ± 0.15	-	14.10 ± 0.30	-	-1.83 ± 0.38	FeII	70
Q0930+28	3.2400	20.35 ± 0.10	-	13.49 ± 0.03	-	-2.07 ± 0.10	SiII	92, 93
QSO B0933-333	2.6820	20.50 ± 0.10	< 11.99	14.46 ± 0.08	-	-1.22 ± 0.12	SiII	1, 66
Q0933+733	1.4800	21.62 ± 0.10	12.71 ± 0.02	15.19 ± 0.01	-	-1.47 ± 0.10	ZnII	101
Q0935+417	1.3700	20.52 ± 0.10	12.26 ± 0.02	14.82 ± 0.10	-	-0.82 ± 0.10	ZnII	61, 79, 100
Q0948+433	1.2300	21.62 ± 0.06	13.15 ± 0.01	15.56 ± 0.01	-	-1.03 ± 0.06	ZnII	101
QSO B0951-0450	3.2350	20.25 ± 0.10	-	13.49 ± 0.03	-	-1.97 ± 0.10	SiII	93
QSO B0951-0450	3.8580	20.60 ± 0.10	-	14.06 ± 0.06	-	-1.47 ± 0.10	SiII	89
QSO B0951-0450	4.2030	20.55 ± 0.10	-	13.07 ± 0.19	< 13.89	-2.55 ± 0.10	OI	89
BR0951-04	3.8600	20.60 ± 0.10	-	14.06 ± 0.06	-	-1.46 ± 0.10	SiII	89, 90
QSO B0952+179	0.2380	21.32 ± 0.05	12.93 ± 0.04	-	-	-0.95 ± 0.06	ZnII	47
QSO B0952-0115	4.0240	20.55 ± 0.10	-	14.19 ± 0.08	-	-2.61 ± 0.11	SiII	90
PC0953+4749	4.2400	20.90 ± 0.15	-	13.90 ± 0.07	-	-2.18 ± 0.15	SiII	106, 93
PC0953+4749	3.8900	21.20 ± 0.10	-	15.09 ± 0.10	-	-1.29 ± 0.23	FeII	106, 93
PSSJ0957+33	3.2800	20.45 ± 0.08	< 12.13	14.37 ± 0.02	< 14.58	-1.08 ± 0.09	SiII	90, 93
PSSJ0957+33	4.1800	20.70 ± 0.10	-	14.13 ± 0.05	14.39 ± 0.06	-1.43 ± 0.12	SII	90, 93
J0958+0145	1.9300	20.40 ± 0.10	< 12.00	14.23 ± 0.05	14.44 ± 0.05	-1.08 ± 0.11	SII	3, 4, 5
J1001+5944	0.3035	19.32 ± 0.10	-	14.30 ± 0.04	< 14.53	-0.37 ± 0.10	OI	2
SDSS1003+5520	2.5000	20.35 ± 0.15	-	12.90 ± 0.30	-	-2.06 ± 0.34	SiII	70
J1004+0018	2.6900	21.39 ± 0.10	-	14.71 ± 0.04	14.70 ± 0.02	-1.81 ± 0.10	SII	28
J1004+0018	2.5400	21.30 ± 0.10	-	15.13 ± 0.02	15.09 ± 0.01	-1.33 ± 0.10	SII	28
Q1007+0042	1.0400	21.15 ± 0.20	13.27 ± 0.04	-	-	-0.44 ± 0.20	ZnII	63
Q1008+36	2.8000	20.70 ± 0.05	-	< 15.11	-	-1.75 ± 0.05	SiII	43
QSO J1009-0026	0.8400	20.20 ± 0.07	< 11.85	14.37 ± 0.03	-	-1.01 ± 0.19	FeII	59
QSO J1009-0026	0.8800	19.48 ± 0.08	12.38 ± 0.04	15.33 ± 0.06	-	0.34 ± 0.09	ZnII	59
J1009+0713	0.1140	20.68 ± 0.10	-	15.29 ± 0.17	15.25 ± 0.12	-0.55 ± 0.16	SII	2
Q1010+0003	1.2700	21.52 ± 0.07	12.96 ± 0.06	15.26 ± 0.05	-	-1.12 ± 0.09	ZnII	58, 63, 3, 4, 5
J1013+4240	4.7979	20.60 ± 0.15	-	-	-	-2.14 ± 0.15	SiII	98
J1013+5615	2.2800	20.70 ± 0.15	13.56 ± 0.05	> 15.45	-	0.30 ± 0.16	ZnII	3, 4, 5
BRI1013+0035	3.1000	21.10 ± 0.10	13.33 ± 0.02	15.18 ± 0.05	-	-0.33 ± 0.10	ZnII	95
J1017+6116	2.7684	20.60 ± 0.10	-	13.76 ± 0.05	-	-2.71 ± 0.10	OI	98
Q1021+30	2.9500	20.70 ± 0.10	< 12.23	14.04 ± 0.01	13.87 ± 0.07	-1.95 ± 0.12	SII	93, 95
J1024+0600	1.9000	20.60 ± 0.15	-	15.27 ± 0.08	15.45 ± 0.05	-0.27 ± 0.16	SII	3, 4, 5
LBQS 1026-0045B	0.6320	19.95 ± 0.07	12.46 ± 0.16	15.11 ± 0.06	-	-0.05 ± 0.17	ZnII	32
LBQS 1026-0045B	0.7090	20.04 ± 0.06	< 12.51	15.10 ± 0.03	-	-0.12 ± 0.19	FeII	32
J1028-0100	0.6321	19.95 ± 0.07	< 12.38	15.08 ± 0.08	-	-0.05 ± 0.21	FeII	26
J1028-0100	0.7089	20.04 ± 0.06	< 12.49	15.12 ± 0.07	-	-0.10 ± 0.20	FeII	26
SDSS1031+4055	2.5700	20.55 ± 0.10	-	13.80 ± 0.20	-	-1.93 ± 0.29	FeII	70
QSO B1036-2257	2.5330	19.30 ± 0.10	< 11.74	12.93 ± 0.01	-	-1.33 ± 0.10	MgII	114
QSO B1036-2257	2.7770	20.93 ± 0.05	< 12.36	14.68 ± 0.01	14.79 ± 0.02	-1.26 ± 0.05	SII	120, 52, 67
Q1037+0028	1.4244	20.04 ± 0.12	< 12.04	14.84 ± 0.02	-	-0.46 ± 0.12	SiII	60
J1037+0139	2.7000	20.50 ± 0.08	-	13.53 ± 0.02	-	-2.13 ± 0.09	OI	16, 70
QSO J1039-2719	2.1390	19.70 ± 0.05	12.09 ± 0.04	14.56 ± 0.02	14.82 ± 0.04	-0.17 ± 0.06	ZnII	109
J1042+3107	4.0865	20.75 ± 0.10	-	14.22 ± 0.03	-	-1.95 ± 0.10	SiII	98
J1042+0628	1.9400	20.70 ± 0.15	-	15.00 ± 0.15	15.08 ± 0.05	-0.74 ± 0.16	SII	3, 4, 5
SDSS1042+0117	2.2700	20.75 ± 0.15	< 12.74	15.08 ± 0.13	-	-0.79 ± 0.17	SiII	44
SDSS1043+6151	2.7900	20.60 ± 0.15	-	14.00 ± 0.20	-	-2.01 ± 0.34	SiII	70
QSO B1045+056	0.9510	19.28 ± 0.02	< 11.70	13.49 ± 0.08	-	-0.97 ± 0.20	FeII	58
SDSS1048+3911	2.3000	20.70 ± 0.10	-	13.70 ± 0.20	-	-2.31 ± 0.32	SiII	70
J1049-0110	1.6600	20.35 ± 0.15	13.14 ± 0.05	15.17 ± 0.05	15.47 ± 0.05	0.23 ± 0.16	ZnII	3, 4, 5

Continued on next page

Table B1 – *Continued from previous page*

QSO name	$z_{\rm abs}$	log N(HI)	log N(Zn)	log N(Fe)	log N(S)	[X/H]	X	Reference
J1051+3107	4.1392	20.70 ± 0.20	-	13.95 ± 0.03	13.86 ± 0.08	-1.96 ± 0.22	SII	98
J1051+3545	4.3498	20.45 ± 0.10	-	13.66 ± 0.05	-	-1.88 ± 0.10	SiII	98
J1051+3545	4.8206	20.35 ± 0.10	-	-	-	-2.28 ± 0.10	SiII	98
Q1054-0020	0.8301	18.95 ± 0.18	< 11.76	14.33 ± 0.01	-	0.20 ± 0.25	FeII	60
Q1054-0020	0.9514	19.28 ± 0.02	< 11.70	13.66 ± 0.01	-	-0.80 ± 0.18	FeII	60
J1054+1633	3.8400	20.65 ± 0.20	-	13.58 ± 0.07	-	-2.25 ± 0.28	FeII	99
J1054+1633	4.8200	20.65 ± 0.20	-	-	-	-2.17 ± 0.20	SiII	99
J1054+1633	4.1400	20.65 ± 0.20	-	-	-	-0.35 ± 0.20	SiII	99
QSO B1055-301	1.9040	21.54 ± 0.10	12.91 ± 0.03	-	-	-1.19 ± 0.10	ZnII	1
Q1055+46	3.3200	20.34 ± 0.10	-	13.94 ± 0.06	-	-1.60 ± 0.15	SiII	91, 43
J1056+1208	1.6100	21.45 ± 0.15	13.76 ± 0.05	15.81 ± 0.05	> 16.15	-0.25 ± 0.16	ZnII	3, 4, 5
J1100+1122	4.3947	21.74 ± 0.10	-	15.21 ± 0.09	-	-1.71 ± 0.22	FeII	98
QSO B1101-26	1.8380	19.50 ± 0.05	< 11.27	13.51 ± 0.02	13.66 ± 0.11	-1.64 ± 0.10	OI	22
J1101+0531	4.3446	21.30 ± 0.10	-	15.19 ± 0.14	-	-1.07 ± 0.12	SiII	98
QSO B1104-181	1.6610	20.85 ± 0.01	12.48 ± 0.01	14.77 ± 0.02	-	-0.93 ± 0.01	ZnII	53
J1106+1044	1.8200	20.50 ± 0.15	-	> 15.15	15.33 ± 0.05	-0.29 ± 0.16	SII	3, 4, 5
QSO J1107+0048	0.7400	21.00 ± 0.04	13.06 ± 0.15	15.53 ± 0.02	-	-0.50 ± 0.16	ZnII	72, 122
QSO B1108-07	3.4820	19.95 ± 0.07	-	-	-	-1.57 ± 0.09	SiII	52
QSO B1108-07	3.6080	20.37 ± 0.07	-	13.88 ± 0.01	-	-1.69 ± 0.08	OI	90, 77
J1111+3509	4.0520	20.80 ± 0.15	-	14.13 ± 0.05	< 14.34	-1.95 ± 0.16	SiII	98
Q1111-152	3.2700	21.30 ± 0.05	12.32 ± 0.10	14.81 ± 0.01	14.62 ± 0.04	-1.54 ± 0.11	ZnII	52, 67, 120, 119
SDSS1116+4118A	2.6600	20.48 ± 0.10	12.40 ± 0.20	14.36 ± 0.10	-	-0.64 ± 0.22	ZnII	31
BR1117-1329	3.3500	20.84 ± 0.12	12.26 ± 0.03	14.83 ± 0.03	-	-1.14 ± 0.12	ZnII	71, 110
HE1122-1649	0.6800	20.45 ± 0.05	< 11.76	14.55 ± 0.01	-	-0.60 ± 0.13	SiII	123, 50
Q1127-145	0.3100	21.70 ± 0.08	13.53 ± 0.13	> 15.16	-	-0.73 ± 0.15	ZnII	45
J1131+6044	2.8800	20.50 ± 0.15	-	13.76 ± 0.03	< 13.29	-1.52 ± 0.20	SiII	34
HS1132+2243	2.7800	21.00 ± 0.07	< 11.99	14.02 ± 0.01	14.07 ± 0.06	-2.05 ± 0.09	SII	93
J1132+1209	4.3800	20.65 ± 0.20	-	13.78 ± 0.07	-	-2.05 ± 0.28	FeII	99
J1132+1209	5.0200	20.65 ± 0.20	-	< 13.55	-	-2.66 ± 0.20	SiII	99
J1135-0010	2.2100	22.05 ± 0.10	13.62 ± 0.03	15.76 ± 0.03	> 16.19	-0.99 ± 0.10	ZnII	48, 69
Q1137+3907	0.7200	21.10 ± 0.10	13.43 ± 0.05	15.45 ± 0.05	-	-0.23 ± 0.11	ZnII	58
J1142+0701	1.8400	21.50 ± 0.15	13.29 ± 0.05	15.47 ± 0.05	-	-0.77 ± 0.16	ZnII	3, 4, 5
QSO B1151+068	1.7750	21.30 ± 0.08	12.34 ± 0.08	-	-	-1.52 ± 0.11	ZnII	80
J115538.6+053050	3.3270	21.00 ± 0.10	-	-	15.31 ± 0.00	-0.81 ± 0.10	SII	114
J1155+3510	2.7582	21.00 ± 0.10	-	< 14.73	14.77 ± 0.01	-1.35 ± 0.10	SII	98
J1155+0530	2.6100	20.37 ± 0.11	-	-	-	-1.57 ± 0.16	SiII	119
J1155+0530	3.3300	21.05 ± 0.10	12.89 ± 0.07	15.37 ± 0.05	15.40 ± 0.05	-0.72 ± 0.12	ZnII	3, 4, 5
Q1157+014	1.9400	21.70 ± 0.10	13.11 ± 0.06	15.49 ± 0.05	> 15.16	-1.15 ± 0.12	ZnII	75, 24, 25, 3, 4, 5
J1200+4015	3.2200	20.85 ± 0.10	12.86 ± 0.04	15.31 ± 0.04	15.36 ± 0.01	-0.55 ± 0.11	ZnII	98
J1200+4618	4.4765	20.50 ± 0.15	-	14.27 ± 0.02	-	-1.41 ± 0.24	FeII	98
J1201+2117	3.7975	21.35 ± 0.15	-	15.56 ± 0.04	-	-0.75 ± 0.15	SiII	98
J1201+2117	4.1578	20.60 ± 0.15	-	13.76 ± 0.03	-	-2.38 ± 0.15	SiII	98
QSO B1202-074	4.3830	20.55 ± 0.16	-	13.88 ± 0.11	-	-1.49 ± 0.17	OI	57, 106, 27
J1202+3235	4.7955	21.10 ± 0.15	-	13.90 ± 0.03	-	-2.38 ± 0.24	FeII	98
J1202+3235	5.0647	20.30 ± 0.15	-	-	-	-2.66 ± 0.16	SiII	98
J1204-0021	3.6400	20.65 ± 0.20	-	13.85 ± 0.04	-	-1.98 ± 0.27	FeII	99
J120550.2+020131	1.7470	20.40 ± 0.10	12.08 ± 0.08	-	-	-0.88 ± 0.13	ZnII	37
J1208+0010	5.0800	20.65 ± 0.20	-	13.27 ± 0.08	-	-2.41 ± 0.20	SiII	99
QSO B1209+0919	2.5840	21.40 ± 0.10	12.98 ± 0.05	15.25 ± 0.03	-	-0.98 ± 0.11	ZnII	95
LBQS 1210+1731	1.8920	20.70 ± 0.08	12.37 ± 0.03	14.95 ± 0.06	14.96 ± 0.03	-0.89 ± 0.09	ZnII	90, 24
Q1215-0034	1.5543	19.56 ± 0.02	< 11.63	14.39 ± 0.01	-	-0.35 ± 0.18	FeII	60
Q1215+33	2.0000	20.95 ± 0.07	12.33 ± 0.05	14.75 ± 0.05	< 15.36	-1.18 ± 0.09	ZnII	89, 11, 90, 91
PG1216+069	0.0063	19.32 ± 0.03	-	13.23 ± 0.14	-	-1.69 ± 0.06	OI	115

Continued on next page

Table B1 – *Continued from previous page*

QSO name	$z_{\rm abs}$	log N(HI)	log N(Zn)	log N(Fe)	log N(S)	[X/H]	X	Reference
J1219+1603	3.0000	20.35 ± 0.10	-	13.80 ± 0.10	-	-2.52 ± 0.35	OI	70
QSO B1220-1800	2.1120	20.12 ± 0.07	-	14.36 ± 0.04	14.53 ± 0.04	-0.71 ± 0.08	SII	66
Q1220-0040	0.9746	20.20 ± 0.07	< 11.69	14.34 ± 0.02	-	-1.04 ± 0.19	FeII	60
J1221+4445	4.8100	20.65 ± 0.20	-	14.35 ± 0.06	-	-2.21 ± 0.20	SiII	99
LBQS 1223+1753	2.4660	21.40 ± 0.10	12.55 ± 0.03	15.16 ± 0.02	15.14 ± 0.04	-1.41 ± 0.10	ZnII	90, 110
LBQS 1223+1753	2.5570	19.32 ± 0.15	< 11.51	13.98 ± 0.03	-	-0.45 ± 0.15	SiII	22
Q1224+0037	1.2300	20.88 ± 0.05	< 11.89	> 15.11	-	-1.29 ± 0.09	SiII	59
Q1225+0035	0.7700	21.38 ± 0.11	< 13.01	15.69 ± 0.03	-	-0.87 ± 0.21	FeII	58, 63
PHL 1226	0.1602	19.48 ± 0.10	-	14.76 ± 0.18	14.84 ± 0.11	0.24 ± 0.15	SII	105
QSO B1228-113	2.1930	20.60 ± 0.10	13.01 ± 0.04	-	-	-0.15 ± 0.11	ZnII	1
Q1228+1018	0.9376	19.41 ± 0.02	< 11.67	14.58 ± 0.01	-	-0.01 ± 0.18	FeII	60
PKS1229-021	0.4000	20.75 ± 0.07	12.92 ± 0.10	< 14.95	-	-0.39 ± 0.12	ZnII	8
QSO B1230-101	1.9310	20.48 ± 0.10	12.94 ± 0.05	-	-	-0.10 ± 0.11	ZnII	1
LBQS 1232+0815	1.7200	19.48 ± 0.13	< 11.58	13.50 ± 0.01	< 14.19	-0.58 ± 0.13	SiII	114
LBQS 1232+0815	2.3340	20.90 ± 0.04	12.64 ± 0.09	14.68 ± 0.08	14.83 ± 0.10	-0.82 ± 0.10	ZnII	108, 40, 12, 120
J1238+3437	2.4714	20.80 ± 0.10	-	14.06 ± 0.03	13.91 ± 0.11	-2.01 ± 0.15	SII	98
J1240+1455	3.1100	21.30 ± 0.20	12.90 ± 0.07	14.60 ± 0.03	15.56 ± 0.02	-0.96 ± 0.21	ZnII	34
J1241+4617	2.6674	20.70 ± 0.10	-	14.02 ± 0.04	-	-2.18 ± 0.10	SiII	98
LBQS1242+0006	1.8200	20.45 ± 0.10	-	-	-	-1.20 ± 0.15	SiII	119
J1245+3822	4.4500	20.65 ± 0.20	-	< 13.93	-	-2.14 ± 0.20	SiII	99
LBQS 1246-0217	1.7810	21.45 ± 0.00	13.01 ± 0.05	15.47 ± 0.02	-	-1.00 ± 0.05	ZnII	44
J1248+3110	3.6973	20.60 ± 0.10	-	14.11 ± 0.03	-	-1.67 ± 0.21	FeII	98
SDSS1249-0233	1.7800	21.45 ± 0.15	13.15 ± 0.05	15.47 ± 0.02	15.53 ± 0.05	-0.86 ± 0.16	ZnII	44, 3, 4, 5
SDSS1251+4120	2.7300	21.10 ± 0.10	-	14.20 ± 0.30	-	-2.71 ± 0.32	SiII	70
J1253+1046	4.6001	20.30 ± 0.15	-	14.09 ± 0.03	-	-1.39 ± 0.24	FeII	98
PSS1253-0228	2.7800	21.85 ± 0.20	12.77 ± 0.07	15.36 ± 0.04	-	-1.64 ± 0.21	ZnII	93
J1257-0111	4.0208	20.30 ± 0.10	-	13.65 ± 0.07	< 13.90	-1.56 ± 0.10	SiII	98
J1304+1202	2.9131	20.55 ± 0.15	< 11.83	13.72 ± 0.04	14.05 ± 0.05	-1.62 ± 0.16	SII	98
J1304+1202	2.9289	20.30 ± 0.15	< 11.95	13.85 ± 0.03	13.91 ± 0.04	-1.51 ± 0.16	SII	98
J1305+0924	2.0200	20.40 ± 0.15	-	15.21 ± 0.14	15.39 ± 0.05	-0.13 ± 0.16	SII	3, 4, 5
J1310+5424	1.8000	21.45 ± 0.15	13.57 ± 0.05	15.64 ± 0.05	> 16.05	-0.44 ± 0.16	ZnII	3, 4, 5
J1323-0021	0.7160	20.21 ± 0.20	13.43 ± 0.05	15.15 ± 0.03	-	0.66 ± 0.21	ZnII	72
Q1323-0021	0.7200	20.54 ± 0.15	13.29 ± 0.21	-	-	0.19 ± 0.26	ZnII	63
SDSS1325+1255	3.5500	20.50 ± 0.15	-	< 13.69	-	-2.51 ± 0.25	SiII	70
Q1328+307	0.6900	21.25 ± 0.10	12.72 ± 0.10	14.98 ± 0.10	-	-1.09 ± 0.14	ZnII	79, 8, 50
QSO J1330-2522	2.6540	19.56 ± 0.13	-	-	-	-1.83 ± 0.13	AlII	114
Q1330-2056	0.8526	19.40 ± 0.02	< 11.96	13.80 ± 0.01	-	-0.78 ± 0.18	FeII	60
QSO B1331+170	1.7760	21.15 ± 0.07	12.61 ± 0.01	14.60 ± 0.00	15.08 ± 0.11	-1.10 ± 0.07	ZnII	89, 22
J1335+0824	1.8600	20.65 ± 0.15	-	> 15.17	15.29 ± 0.05	-0.48 ± 0.16	SII	3, 4, 5
Q1337+113	2.8000	21.00 ± 0.08	< 12.25	14.33 ± 0.01	14.33 ± 0.02	-1.95 ± 0.11	OI	93, 110, 52, 95, 77, 67
J1340+1106	2.8000	21.00 ± 0.06	-	14.32 ± 0.01	14.30 ± 0.02	-1.65 ± 0.07	OI	16
J1340+3926	4.8300	20.65 ± 0.20	-	14.33 ± 0.05	-	-1.50 ± 0.27	FeII	99
QSO J1342-1355	3.1180	20.05 ± 0.08	-	13.93 ± 0.03	13.83 ± 0.03	-1.22 ± 0.08	OI	77
J1345+2329	5.0100	20.65 ± 0.20	-	-	14.66 ± 0.05	-1.11 ± 0.21	SII	99
BRI1346-03	3.7400	20.72 ± 0.10	-	< 14.13	-	-2.28 ± 0.10	SiII	89, 90
SDSS1350+5952	2.7600	20.65 ± 0.10	-	13.50 ± 0.20	-	-2.33 ± 0.29	FeII	70
J1353+5328	2.8349	20.80 ± 0.10	-	> 14.46	14.57 ± 0.02	-1.35 ± 0.10	SII	98
Q1354+258	1.4200	21.54 ± 0.06	12.59 ± 0.08	15.01 ± 0.04	-	-1.51 ± 0.10	ZnII	81
PKS1354-17	2.7800	20.30 ± 0.15	-	13.37 ± 0.08	-	-1.83 ± 0.16	SiII	93
QSO J1356-1101	2.3970	19.85 ± 0.08	< 12.38	13.44 ± 0.01	-	-1.59 ± 0.20	FeII	114
QSO J1356-1101	2.5010	20.44 ± 0.05	< 11.70	14.36 ± 0.08	14.27 ± 0.09	-1.29 ± 0.10	SII	1, 66
QSO J1356-1101	2.9670	20.80 ± 0.10	< 11.93	14.63 ± 0.05	-	-1.35 ± 0.12	SiII	1, 66

Continued on next page

Table B1 – *Continued from previous page*

QSO name	$z_{\rm abs}$	log N(HI)	log N(Zn)	log N(Fe)	log N(S)	[X/H]	X	Reference
J1358+0349	2.8500	20.50 ± 0.10	-	13.01 ± 0.05	-	-2.81 ± 0.27	OI	70
J1358+6522	3.0700	20.35 ± 0.15	-	< 12.80	-	-3.01 ± 0.17	OI	70, 18
QSO B1409+0930	2.0190	20.65 ± 0.10	11.63 ± 0.10	-	-	-1.58 ± 0.14	ZnII	52
QSO B1409+0930	2.4560	20.53 ± 0.08	-	13.74 ± 0.02	-	-2.07 ± 0.10	OI	83
QSO B1409+0930	2.6680	19.80 ± 0.08	< 11.22	14.02 ± 0.13	13.54 ± 0.06	-1.18 ± 0.14	OI	83, 22
J1412+0624	4.1095	20.40 ± 0.15	-	13.83 ± 0.08	-	-1.75 ± 0.25	FeII	98
J1417+4132	1.9500	21.45 ± 0.25	13.55 ± 0.05	15.58 ± 0.05	> 15.80	-0.46 ± 0.25	ZnII	3, 4, 5
J1418+3142	3.9600	20.65 ± 0.20	-	< 15.78	-	-0.39 ± 0.20	SiII	99
J1419+0829	3.0500	20.40 ± 0.03	-	13.54 ± 0.03	-	-1.92 ± 0.04	OI	16, 86
QSO J1421-0643	3.4480	20.40 ± 0.10	< 11.98	14.18 ± 0.08	-	-1.29 ± 0.13	SiII	1, 66
Q1425+6039	2.8300	20.30 ± 0.04	12.18 ± 0.04	14.48 ± 0.01	-	-0.68 ± 0.06	ZnII	57, 91, 92, 95
J1431+3952	0.6000	21.20 ± 0.10	13.03 ± 0.19	15.15 ± 0.11	-	-0.73 ± 0.21	ZnII	35
PSS1432+39	3.2700	21.25 ± 0.10	< 12.65	> 14.93	-	-1.09 ± 0.11	SiII	93
J1435+3604	0.2026	19.80 ± 0.10	-	14.20 ± 0.08	14.60 ± 0.12	-0.32 ± 0.16	SII	2
SDSS1435+0420	1.6600	21.25 ± 0.15	< 13.21	15.70 ± 0.07	-	-0.84 ± 0.17	SiII	44
J1435+5359	2.3400	21.05 ± 0.10	-	-	14.78 ± 0.05	-1.39 ± 0.11	SII	43
Q1436-0051	0.7377	20.08 ± 0.11	12.67 ± 0.05	14.94 ± 0.02	-	0.03 ± 0.12	ZnII	60
J1437+2323	4.8000	20.65 ± 0.20	-	-	-	-2.34 ± 0.20	SiII	99
J1438+4314	4.3990	20.89 ± 0.15	-	14.42 ± 0.01	14.73 ± 0.01	-1.28 ± 0.15	SII	98
QSO J1439+1117	2.4180	20.10 ± 0.10	12.93 ± 0.04	14.28 ± 0.05	15.27 ± 0.06	0.27 ± 0.11	ZnII	66
SDSS1440+0637	2.5200	21.00 ± 0.15	-	14.50 ± 0.30	-	-2.31 ± 0.34	SiII	70
QSO J1443+2724	4.2240	20.95 ± 0.10	12.99 ± 0.03	15.33 ± 0.03	15.52 ± 0.01	-0.52 ± 0.10	ZnII	90, 66, 52
LBQS 1444+0126	2.0870	20.25 ± 0.07	12.12 ± 0.15	14.41 ± 0.03	14.62 ± 0.08	-0.69 ± 0.17	ZnII	51, 22
Q1451+123	2.4700	20.39 ± 0.10	-	13.36 ± 0.07	< 13.55	-1.90 ± 0.16	SiII	75, 110
Q1451+123	2.2600	20.30 ± 0.15	11.85 ± 0.11	14.33 ± 0.07	-	-1.01 ± 0.19	ZnII	22
J1454+0941	1.7900	20.50 ± 0.15	12.72 ± 0.05	15.02 ± 0.12	15.25 ± 0.06	-0.34 ± 0.16	ZnII	3, 4, 5
Q1455-0045	1.0929	20.08 ± 0.06	< 11.91	14.57 ± 0.01	-	-0.95 ± 0.12	SiII	60
J1456+0407	2.6700	20.35 ± 0.10	-	13.00 ± 0.10	-	-2.49 ± 0.30	OI	70
Q1501+0019	1.4800	20.85 ± 0.13	12.93 ± 0.06	-	-	-0.48 ± 0.14	ZnII	58
Q1502+4837	2.5700	20.30 ± 0.15	-	14.15 ± 0.12	-	-1.57 ± 0.17	SiII	93
PSS1506+5220	3.2200	20.67 ± 0.07	< 12.11	13.71 ± 0.03	-	-2.30 ± 0.07	SiII	93
J1507+4406	3.0644	20.75 ± 0.10	-	14.03 ± 0.03	13.97 ± 0.10	-1.90 ± 0.14	SII	98
J1509+1113	2.0300	21.30 ± 0.15	-	15.48 ± 0.07	15.69 ± 0.05	-0.73 ± 0.16	SII	3, 4, 5
PSS1535+2943	3.7600	20.40 ± 0.15	-	-	-	-1.97 ± 0.16	SiII	94
J1541+3153	2.4435	20.95 ± 0.10	12.03 ± 0.11	14.50 ± 0.11	-	-1.48 ± 0.15	ZnII	98
SBS1543+393	0.0100	20.42 ± 0.04	-	-	15.19 ± 0.04	-0.35 ± 0.06	SII	9
J1553+3548	0.0830	19.55 ± 0.15	-	14.01 ± 0.07	< 14.24	-0.84 ± 0.16	SiII	2
J1555+4800	2.3900	21.50 ± 0.15	< 13.95	15.84 ± 0.05	> 15.88	-0.46 ± 0.16	SiII	3, 4, 5
SDSS1557+2320	3.5400	20.65 ± 0.10	-	13.50 ± 0.30	-	-2.24 ± 0.15	OI	70
SDSSJ1558+4053	2.5500	20.30 ± 0.04	-	13.07 ± 0.06	-	-2.45 ± 0.06	OI	85
J1558-0031	2.7000	20.67 ± 0.05	-	14.11 ± 0.03	14.07 ± 0.02	-1.72 ± 0.05	SII	43
PHL 1598	0.4297	19.18 ± 0.03	-	-	14.36 ± 0.05	0.06 ± 0.06	SII	105
J1604+3951	3.1600	21.75 ± 0.20	13.12 ± 0.05	15.47 ± 0.05	15.71 ± 0.05	-1.19 ± 0.21	ZnII	34, 3, 4, 5
J1607+1604	4.4741	20.30 ± 0.15	-	14.03 ± 0.06	-	-1.71 ± 0.15	SiII	98
SDSS1610+4724	2.5100	21.15 ± 0.15	13.56 ± 0.05	15.62 ± 0.05	> 16.01	-0.15 ± 0.16	ZnII	44, 3, 4, 5
J1616+4154	0.3211	20.60 ± 0.20	-	15.02 ± 0.05	15.37 ± 0.11	-0.35 ± 0.23	SII	2
J1619+3342	0.0963	20.55 ± 0.10	-	14.38 ± 0.15	15.08 ± 0.09	-0.59 ± 0.13	SII	2
QSO J1621-0042	3.1040	19.70 ± 0.20	-	13.30 ± 0.04	-	-1.43 ± 0.20	SiII	114
3C336	0.6600	20.36 ± 0.10	-	14.59 ± 0.11	-	-0.95 ± 0.23	FeII	113, 14, 50
J1623+0718	1.3400	21.35 ± 0.10	12.91 ± 0.09	15.28 ± 0.05	-	-1.00 ± 0.13	ZnII	35
J1626+2751	4.3110	21.34 ± 0.15	-	15.33 ± 0.06	-	-1.19 ± 0.24	FeII	98
J1626+2751	4.4975	21.39 ± 0.15	-	14.08 ± 0.02	-	-2.49 ± 0.24	FeII	98
J1626+2751	5.1791	20.94 ± 0.15	-	> 14.59	14.60 ± 0.02	-1.46 ± 0.15	SII	98
J1626+2858	4.6100	20.65 ± 0.20	-	-	-	-2.73 ± 0.22	SiII	99

Continued on next page

Table B1 – *Continued from previous page*

QSO name	$z_{\rm abs}$	log N(HI)	log N(Zn)	log N(Fe)	log N(S)	[X/H]	X	Reference
J1629+0913	1.9000	20.80 ± 0.10	12.68 ± 0.08	> 14.93	15.24 ± 0.05	-0.68 ± 0.13	ZnII	3, 4, 5
4C 12.59	0.5310	20.70 ± 0.09	-	14.26 ± 0.08	-	-1.62 ± 0.22	FeII	114
4C 12.59	0.9000	19.70 ± 0.04	< 12.18	14.17 ± 0.03	-	-0.71 ± 0.19	FeII	60
J1637+2901	3.5000	20.70 ± 0.10	-	13.84 ± 0.10	-	-3.10 ± 0.22	OI	70
J1654+2227	4.0022	20.60 ± 0.15	-	14.09 ± 0.03	-	-1.69 ± 0.24	FeII	98
SDSS1709+3417	2.5300	20.45 ± 0.15	-	14.30 ± 0.20	-	-1.46 ± 0.25	SiII	70
SDSS1709+3417	3.0100	20.40 ± 0.10	-	13.90 ± 0.20	-	-1.68 ± 0.29	FeII	70
J1712+5755	2.2500	20.60 ± 0.10	-	14.49 ± 0.02	-	-1.19 ± 0.12	SiII	43
Q1715+4606	0.6500	20.44 ± 0.10	< 12.87	14.94 ± 0.03	-	-0.68 ± 0.21	FeII	58
PSS1715+3809	3.3400	21.05 ± 0.12	< 12.11	13.74 ± 0.04	-	-2.49 ± 0.22	FeII	94
Q1727+5302	1.0300	21.41 ± 0.15	12.76 ± 0.24	14.81 ± 0.01	-	-1.21 ± 0.28	ZnII	116, 63
Q1727+5302	0.9400	21.16 ± 0.10	13.25 ± 0.11	15.29 ± 0.01	-	-0.47 ± 0.15	ZnII	116, 63
Q1733+5533	1.0000	20.70 ± 0.10	< 12.11	-	-	-0.73 ± 0.12	SiII	58, 63
SDSS1737+5828	4.7400	20.65 ± 0.10	-	13.30 ± 0.10	-	-2.53 ± 0.23	FeII	106
J1737+5828	4.7400	20.65 ± 0.20	-	-	-	-2.23 ± 0.21	SiII	99
Q1755+578	1.9700	21.40 ± 0.15	13.85 ± 0.05	15.79 ± 0.05	> 16.12	-0.11 ± 0.16	ZnII	3, 4, 5
Q1759+75	2.6300	20.76 ± 0.05	> 11.65	15.08 ± 0.02	15.24 ± 0.01	-0.64 ± 0.05	SII	89, 90, 43
PSS1802+5616	3.8100	20.35 ± 0.20	-	13.67 ± 0.10	-	-1.99 ± 0.22	SiII	94
PSS1802+5616	3.5500	20.50 ± 0.10	< 12.63	14.08 ± 0.06	-	-1.60 ± 0.21	FeII	94
PSS1802+5616	3.3900	20.30 ± 0.10	< 12.41	14.26 ± 0.04	-	-1.22 ± 0.21	FeII	94
QSO B2000-330	3.1720	19.75 ± 0.15	-	< 12.86	-	-2.29 ± 0.15	OI	96
QSO B2000-330	3.1880	19.80 ± 0.15	-	13.69 ± 0.04	-	-1.34 ± 0.15	SiII	96
QSO B2000-330	3.1920	19.10 ± 0.15	-	13.49 ± 0.07	-	-0.48 ± 0.15	SiII	96
J2036-0553	2.2800	21.20 ± 0.15	-	14.68 ± 0.11	-	-1.67 ± 0.16	SiII	43
Q2051+1950	1.1157	20.00 ± 0.15	12.90 ± 0.10	15.02 ± 0.02	-	0.34 ± 0.18	ZnII	60
SDSS2059-0529	2.2100	20.80 ± 0.20	12.94 ± 0.11	15.00 ± 0.11	-	-0.42 ± 0.23	ZnII	44
Q2059-360	3.0800	20.98 ± 0.08	-	14.52 ± 0.07	14.41 ± 0.04	-1.58 ± 0.09	OI	75, 110, 77
SDSS2100-0641	3.0900	21.05 ± 0.15	13.24 ± 0.05	15.37 ± 0.05	15.49 ± 0.05	-0.37 ± 0.16	ZnII	44, 3, 4, 5
LBQS 2114-4347	1.9120	19.50 ± 0.10	< 12.17	14.02 ± 0.01	< 13.97	-0.70 ± 0.10	MgII	114
QSO J2119-3536	1.9960	20.10 ± 0.07	12.30 ± 0.09	14.77 ± 0.09	< 14.95	-0.36 ± 0.11	ZnII	22
QSO B2126-15	2.6380	19.25 ± 0.15	< 11.58	14.05 ± 0.01	-	-0.09 ± 0.15	SiII	114
QSO B2126-15	2.7690	19.20 ± 0.15	< 11.95	14.17 ± 0.00	-	0.08 ± 0.15	SiII	114
LBQS 2132-4321	1.9160	20.74 ± 0.09	12.66 ± 0.02	15.03 ± 0.02	> 14.90	-0.64 ± 0.09	ZnII	114
LBQS 2138-4427	2.3830	20.60 ± 0.05	12.05 ± 0.07	-	-	-1.11 ± 0.09	ZnII	52
LBQS 2138-4427	2.8520	20.98 ± 0.05	11.99 ± 0.05	14.65 ± 0.02	14.50 ± 0.02	-1.55 ± 0.07	ZnII	51, 110
J2144-0632	4.1300	20.40 ± 0.15	-	< 13.51	-	-2.37 ± 0.47	OI	70
PSSJ2155+1358	3.3200	20.50 ± 0.15	12.05 ± 0.32	14.51 ± 0.13	-	-1.01 ± 0.35	ZnII	19, 93
LBQS 2206-1958A	2.0760	20.44 ± 0.05	< 11.20	13.33 ± 0.01	-	-2.08 ± 0.06	OI	84
Q2206-199	1.9200	20.68 ± 0.03	12.91 ± 0.01	15.30 ± 0.02	15.42 ± 0.02	-0.33 ± 0.03	ZnII	88, 90, 91, 117
QSO B2222-396	2.1540	20.85 ± 0.10	-	14.42 ± 0.03	14.08 ± 0.02	-1.89 ± 0.10	SII	66
SDSS2222-0946	2.3500	20.50 ± 0.15	< 12.78	15.06 ± 0.08	15.37 ± 0.05	-0.25 ± 0.16	SII	44, 3, 4, 46, 5
Q2223+20	3.1200	20.30 ± 0.10	-	13.32 ± 0.06	-	-2.17 ± 0.11	SiII	93
Q2228-3954	2.1000	21.20 ± 0.10	12.51 ± 0.06	15.17 ± 0.02	-	-1.25 ± 0.12	ZnII	67
LBQS 2230+0232	1.8640	20.83 ± 0.10	12.80 ± 0.03	15.19 ± 0.02	15.29 ± 0.10	-0.59 ± 0.10	ZnII	89, 90, 91, 24, 25, 3, 4, 5
Q2231-00	2.0700	20.53 ± 0.08	12.30 ± 0.05	14.83 ± 0.03	15.10 ± 0.15	-0.79 ± 0.09	ZnII	89, 90, 21, 23
QSO B2237-0607	4.0790	20.55 ± 0.10	-	13.85 ± 0.11	-	-1.79 ± 0.10	SiII	57, 106, 43
J223941.8-294955	1.8250	19.84 ± 0.14	12.76 ± 0.06	14.33 ± 0.04	-	0.36 ± 0.15	ZnII	24
J2241+1225	2.4200	21.15 ± 0.15	-	15.02 ± 0.08	> 15.01	-1.31 ± 0.25	FeII	3, 4, 5

Continued on next page

Table B1 – *Continued from previous page*

QSO name	$z_{\rm abs}$	log N(HI)	log N(Zn)	log N(Fe)	log N(S)	[X/H]	X	Reference
PSS2241+1352	4.2800	21.15 ± 0.10	-	> 14.65	14.58 ± 0.03	-1.69 ± 0.10	SII	93
HE2243-6031	2.3300	20.67 ± 0.02	12.22 ± 0.03	14.92 ± 0.01	14.88 ± 0.01	-1.01 ± 0.04	ZnII	54
J2252+1425	4.7475	20.60 ± 0.15	-	13.98 ± 0.11	< 14.41	-1.80 ± 0.26	FeII	98
QSO B2311-373	2.1820	20.48 ± 0.13	< 11.82	14.23 ± 0.04	-	-1.45 ± 0.15	SiII	1, 66
B2314-409	1.8600	20.90 ± 0.10	12.52 ± 0.10	15.08 ± 0.10	15.10 ± 0.15	-0.94 ± 0.14	ZnII	30
PSS2315+0921	3.4300	21.10 ± 0.20	-	> 14.63	-	-1.46 ± 0.21	SiII	94
QSO B2318-1107	1.6290	20.52 ± 0.14	< 11.74	14.14 ± 0.02	< 14.54	-1.56 ± 0.23	FeII	114
QSO B2318-1107	1.9890	20.68 ± 0.05	12.50 ± 0.03	14.91 ± 0.01	15.09 ± 0.02	-0.74 ± 0.06	ZnII	64
J2321+1421	2.5700	20.70 ± 0.05	< 11.84	14.18 ± 0.03	< 13.60	-1.76 ± 0.06	SiII	34
PSS2323+2758	3.6800	20.95 ± 0.10	-	13.32 ± 0.13	-	-2.54 ± 0.10	SiII	93
QSO J2328+0022	0.6520	20.32 ± 0.07	12.43 ± 0.15	14.84 ± 0.01	-	-0.45 ± 0.17	ZnII	72
QSO B2332-094	3.0570	20.50 ± 0.07	< 12.17	14.34 ± 0.03	14.34 ± 0.18	-1.24 ± 0.07	OI	51, 93, 77, 119
J233544.2+150118	0.6800	19.70 ± 0.30	12.37 ± 0.04	14.83 ± 0.03	-	0.11 ± 0.30	ZnII	74
J2340-00	2.0500	20.35 ± 0.15	12.63 ± 0.07	14.98 ± 0.05	14.95 ± 0.05	-0.28 ± 0.17	ZnII	95, 3, 4, 5
Q2342+34	2.9100	21.10 ± 0.10	< 12.60	14.91 ± 0.07	15.19 ± 0.05	-1.03 ± 0.11	SII	93, 95, 3, 4, 120, 5
QSO B2343+125	2.4310	20.40 ± 0.07	12.20 ± 0.07	14.52 ± 0.02	14.66 ± 0.02	-0.76 ± 0.10	ZnII	64
Q2344+12	2.5400	20.36 ± 0.10	-	14.03 ± 0.03	< 14.20	-1.69 ± 0.10	SiII	90, 92
PSSJ2344+0342	3.2200	21.25 ± 0.08	12.23 ± 0.30	15.06 ± 0.15	-	-1.58 ± 0.31	ZnII	19, 93
QSO J2346+1247	2.5690	20.98 ± 0.04	12.88 ± 0.06	15.24 ± 0.04	15.38 ± 0.05	-0.66 ± 0.07	ZnII	104
QSO B2348-0180	2.4260	20.50 ± 0.10	< 11.20	14.83 ± 0.07	15.06 ± 0.10	-0.56 ± 0.14	SII	65
QSO B2348-0180	2.6150	21.30 ± 0.08	< 11.87	14.57 ± 0.09	-	-1.92 ± 0.11	SiII	90
QSO B2348-147	2.2790	20.56 ± 0.08	< 11.28	13.79 ± 0.02	13.72 ± 0.12	-1.95 ± 0.14	SII	89, 24
Q2352-0028	0.8730	19.18 ± 0.09	< 11.67	13.48 ± 0.02	-	-0.88 ± 0.20	FeII	60
Q2352-0028	1.0318	19.81 ± 0.13	< 11.93	14.91 ± 0.01	-	0.17 ± 0.13	SiII	60
Q2352-0028	1.2467	19.60 ± 0.24	< 11.53	14.21 ± 0.01	-	-0.57 ± 0.30	FeII	60
Q2353-0028	0.6000	21.54 ± 0.15	13.25 ± 0.29	-	-	-0.85 ± 0.33	ZnII	63
B2355-106	1.1700	21.00 ± 0.10	12.76 ± 0.17	15.08 ± 0.10	-	-0.80 ± 0.20	ZnII	35
LBQS 2359-0216	2.0950	20.65 ± 0.10	12.60 ± 0.03	14.51 ± 0.03	-	-0.61 ± 0.10	ZnII	89
LBQS 2359-0216	2.1540	20.30 ± 0.10	< 11.90	13.89 ± 0.03	-	-1.49 ± 0.10	SiII	89

References: 1: Akerman et al. 2005, 2: Battisti et al. 2012, 3: Berg et al. 2013, 4: Berg et al. 2015b, 5: Berg et al. 2015a, 6: Bergeron & Dodorico 1986, 7: Blades et al. 1982, 8: Boissé et al. 1998, 9: Bowen et al. 2005, 10: Carswell et al. 1996, 11: Centurion et al. 2000, 12: Centurion et al. 2003, 13: Chen, Kennicutt & Rauch 2005, 14: Churchill et al. 2000, 15: Cooke et al. 2010a, 16: Cooke et al. 2011, 17: Cooke et al. 2010b, 18: Cooke, Pettini & Murphy 2012, 19: Dessauge-Zavadsky (unpublished), 20: Dessauges-Zavadsky et al. 2001, 21: Dessauges-Zavadsky, Prochaska & D'Odorico 2002, 22: Dessauges-Zavadsky et al. 2003, 23: Dessauges-Zavadsky et al. 2004, 24: Dessauges-Zavadsky et al. 2006, 25: Dessauges-Zavadsky et al. 2007, 26: Dessauges-Zavadsky, Ellison & Murphy 2009, 27: D'Odorico & Molaro 2004, 28: Dutta et al. 2014, 29: Ellison et al. 2001, 30: Ellison & Lopez 2001, 31: Ellison et al. 2007, 32: Ellison et al. 2008, 33: Ellison & Lopez 2009, 34: Ellison et al. 2010, 35: Ellison et al. 2012, 36: Fox et al. 2007, 37: Fox et al. 2009, 38: Fynbo et al. 2011, 39: Fynbo et al. 2013, 40: Ge, Bechtold & Kulkarni 2001, 41: Guimarães et al. 2012, 42: Heinmueller et al. 2006, 43: Henry & Prochaska 2007, 44: HerbertFort et al. 2006, 45: Kanekar et al. 2014, 46: Krogager et al. 2013, 47: Kulkarni et al. 2005, 48: Kulkarni et al. 2012, 49: Ledoux, Srianand & Petitjean 2002, 50: Ledoux, Bergeron & Petitjean 2002, 51: Ledoux, Petitjean & Srianand 2003, 52: Ledoux et al. 2006, 53: Lopez et al. 1999, 54: Lopez et al. 2002, 55: Lopez & Ellison 2003, 56: Lopez et al. 2005, 57: Lu et al. 1996, 58: Meiring et al. 2006, 59: Meiring et al. 2007, 60: Meiring et al. 2009a, 61: Meyer, Lanzetta & Wolfe 1995, 62: Molaro et al. 2000, 63: Nestor et al. 2008, 64: Noterdaeme et al. 2007a, 65: Noterdaeme et al. 2007b, 66: Noterdaeme et al. 2008b, 67: Noterdaeme et al. 2008a, 68: Noterdaeme et al. 2012b, 69: Noterdaeme et al. 2012a, 70: Penprase et al. 2010, 71: Peroux et al. 2002, 72: Péroux et al. 2006a, 73: Péroux et al. 2007, 74: Péroux et al. 2008, 75: Petitjean, Srianand & Ledoux 2000, 76: Petitjean, Srianand & Ledoux 2002, 77: Petitjean, Ledoux & Srianand 2008, 78: Pettini et al. 1994, 79: Pettini et al. 1997a, 80: Pettini et al. 1997b, 81: Pettini et al. 1999, 82: Pettini et al. 2000, 83: Pettini et al. 2002, 84: Pettini et al. 2008a, 85: Pettini et al. 2008b, 86: Pettini & Cooke 2012, 87: Prochaska & Wolfe 1996, 88: Prochaska & Wolfe 1997a, 89: Prochaska & Wolfe 1999, 90: Prochaska & Wolfe 2002, 91: Prochaska, Gawiser & Wolfe 2001, 92: Prochaska et al. 2002, 93: Prochaska et al. 2003, 94: Prochaska, Castro & Djorgovski 2003, 95: Prochaska et al. 2007, 96: Prochter et al. 2010, 97: Quast, Reimers & Baade 2008, 98: Rafelski et al. 2012, 99: Rafelski et al. 2014, 100: Rao & Turnshek 2000, 101: Rao et al. 2005, 102: Rao, Turnshek & Nestor 2006, 103: Richter, Westmeier & Bruens 2005, 104: Rix et al. 2007, 105: Som et al. 2015, 106: Songaila & Cowie 2002, 107: Srianand & Petitjean 1998, 108: Srianand, Petitjean & Ledoux 2000, 109: Srianand & Petitjean 2001, 110: Srianand et al.

2005, 111: Srianand, Gupta & Petitjean 2007, 112: Srianand et al. 2012, 113: Steidel et al. 1997, 114: This work, 115: Tripp et al. 2005, 116: Turnshek et al. 2004, 117: Vladilo et al. 2011, 118: Zafar et al. 2011, 119: Zafar et al. 2014a, 120: Zafar et al. 2014b, 121: Zafar et al. (in prep), 122: Zych et al. 2009, 123: de la Varga et al. 2000

APPENDIX C: INDIVIDUAL OBJECTS

This Appendix summarizes a description of the individual systems as well as figures and tables providing the Voigt profile parameters for the low, intermediate and high-ionization species when available. For the following figures, we use z_{abs} from the literature as the zero velocity component.

C1 QSOJ0008-2900 $z_{em} = 2.645$, $z_{abs} = 2.254$, $\log N(HI) = 20.22 \pm 0.10$

The EUADP spectrum for this absorber covers multiple low-ionization transitions including FeII $\lambda\lambda\lambda$ 2374, 2382, 2586, 2600, SiII λ 1526, and the saturated MgII doublet $\lambda\lambda$ 2796, 2803. The velocity profiles are well fitted with 5 components. The fit to the Fe lines is found to be consistent with the non-detection of FeII λ 2260. The resulting total column density of Fe is $\log N(FeII) = 13.78 \pm 0.01$. By comparing the detected SiII λ 1526 line with the weak SiII λ 1808 transition, we deduce that the former is slightly contaminated. An estimation on the column density based on SiII λ 1808 gives $\log N(SiII) = 14.40 \pm 0.1$. This total column density is confirmed with the apparent optical depth method applied on SiII λ 1808 from v = −72 km/s and v = +10 km/s. Because it is saturated, the MgII doublet is fitted fixing the number of components and parameters to the low-ionization lines. The result provides a lower limit to the Mg column density of $\log N(MgII) > 15.1$. The non-detection of CrII λ 2062, ZnII λ 2026 and MnII λ 2576 leads to the determination of the following upper limits: $\log N(CrII) < 12.37$, $\log N(ZnII) < 11.68$ and $\log N(MnII) < 12.02$.

In addition to these low-ionization ions, the quasar spectrum covers high-ionization species including the SiIV doublet $\lambda\lambda$ 1393 and 1402. However, the bluest SiIV line lies on the Lyα emission line of the quasar thus complicating the quasar continuum placement. Therefore the reddest component of the SiIV doublet is used to model the Voigt profile. In addition, the intermediate-ionization lines of AlIII $\lambda\lambda$ 1854 and 1862 present a similar velocity profile to the SiIV doublet. Therefore, the fit is performed using these transitions simultaneously. A satisfactory 3-component fit leads to the following column densities: $\log N(SiIV) = 13.72 \pm 0.03$ and $\log N(AlIII) = 12.39 \pm 0.04$.

The parameter fits are summarised in Table C1 and Voigt profile fits are shown in Fig. C1.

Table C1. Voigt profile fit parameters to the low- and high-ionisation species for the z_{abs}=2.645 log N(H I)=20.22 ± 0.10 absorber towards QSO J0008-2900. In this table and in the following ones, the values with no uncertainties have been manually fixed to improve the fitting process.

Comp.	z_{abs}	b km s^{-1}	Ion	log N cm^{-2}
1	2.25337	4.5 ± 0.2	FeII	12.95 ± 0.01
			SiII	13.70
2	2.25352	2.8 ± 0.2	FeII	13.00 ± 0.01
			SiII	13.80
3	2.25367	4.0 ± 0.2	FeII	13.24 ± 0.01
			SiII	13.85
4	2.25380	5.0 ± 0.3	FeII	13.20 ± 0.02
			SiII	13.40
5	2.25392	5.3 ± 0.3	FeII	12.91 ± 0.02
			SiII	13.60
1	2.25332	16.1 ± 2.7	SiIV	13.19 ± 0.05
			AlIII	11.74 ± 0.10
2	2.25366	9.0 ± 1.1	SiIV	13.42 ± 0.05
			AlIII	12.07 ± 0.06
3	2.25389	9.2 ± 1.9	SiIV	13.05 ± 0.08
			AlIII	11.88 ± 0.08

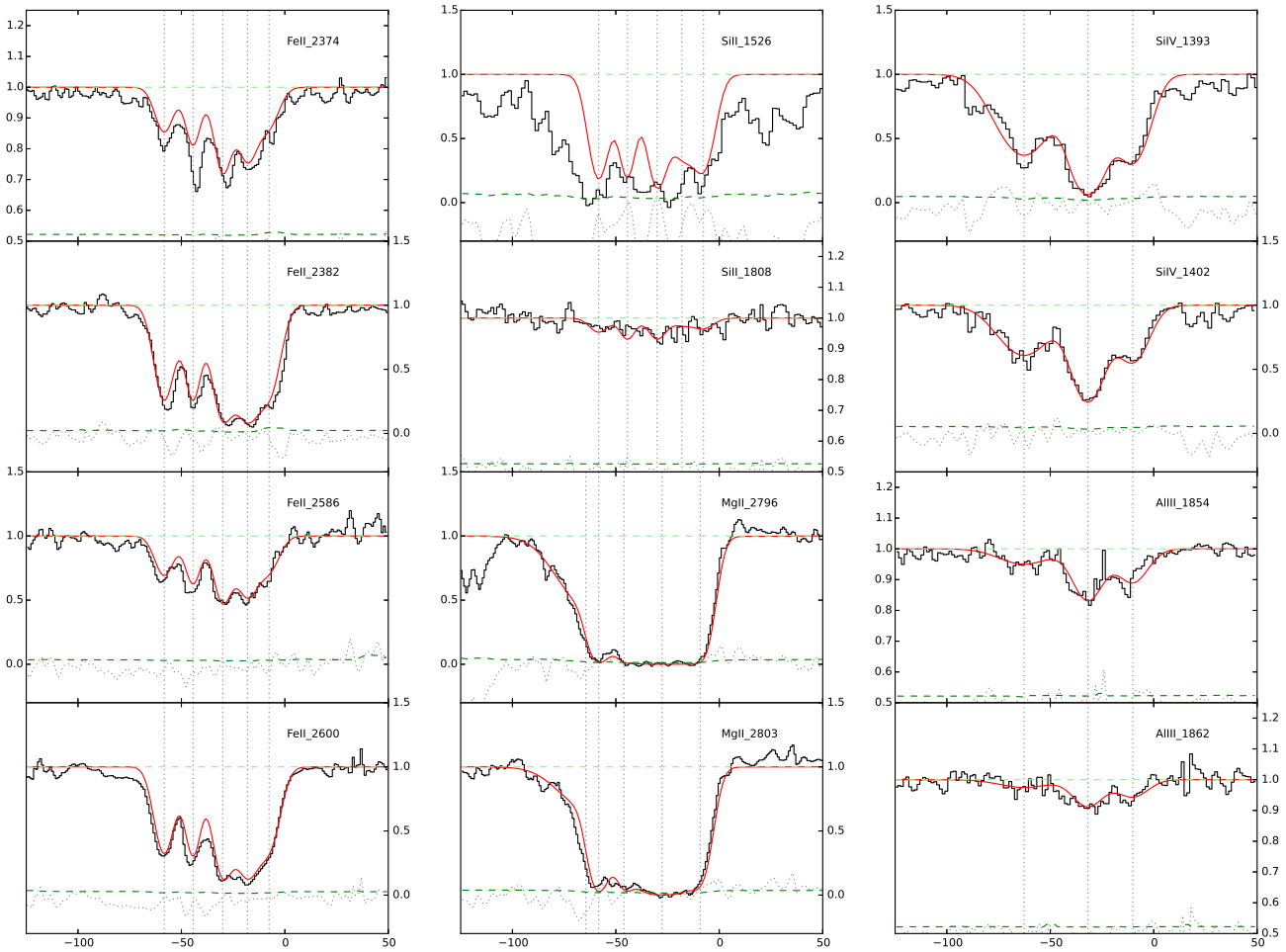

Figure C1. Fit to the low-ionization transitions of the $z_{abs} = 2.254$, log N(H I) $= 20.22 \pm 0.10$ absorber towards QSOJ0008-2900 (see Table C1). In this and the following figures, the Voigt profile fits are overlaid in red above the observed quasar spectrum (black) and the green horizontal line indicates the normalised flux level to one. The zero velocity corresponds to the absorption redshift listed in Table 1 and the vertical dotted lines correspond to the redshift of the fitted components. We warn the reader that the y-axis varies from one panel to another in order to optimise for each transitions so that weaker lines can be readily seen.

Table C2. Voigt profile fit parameters to the low-ionization species for the z_{abs}=2.491 log N(H I)=19.94 ± 0.11 absorber towards QSO J0008-2901.

Comp.	z_{abs}	b km s^{-1}	Ion	log N cm^{-2}
1	2.49046	1.6 ± 0.2	FeII	12.60 ± 0.07
			SII	12.98 ± 0.91
			OI	13.32 ± 1.54
2	2.49054	4.1 ± 0.1	FeII	13.61 ± 0.02
			SII	13.58 ± 0.02
			OI	15.31 ± 0.24

C2 QSOJ0008-2901 z_{em} = 2.607, z_{abs} = 2.491, log N(HI) = 19.94 ± 0.11

In this case, the quasar spectrum is of modest SNR. The wavelength coverage includes low-ionization lines of FeII λλλλ 2260, 2344, 2382, 2586, SII λ 1259 and OI λ 1039. A two-component fit is used given the asymmetrical shape of the FeII and SII lines. The resulting column densities are log N(FeII)= 13.65 ± 0.02, log N(OI)= 15.31 ± 0.24 and log N(SII)= 13.68 ± 0.18. Finally, we used the non-detection of the following transitions to derive upper limits on the column densities: CrII λ 2062 log N(CrII)< 12.9, NiII λ 1741 log N(NiII)< 13.29, ZnII λ 2026 log N(ZnII)< 12.12 and AlIII λ 1854 log N(AlII)< 12.2.

The EUADP quasar spectrum does not cover the CIV doublet for this absorber. In addition, the high-ionization SiIV doublet λλ 1393 and 1402 is covered but no satisfactory fit could be determined given the low SNR of the quasar spectrum in this region.

The resulting parameter fits are summarised in Table C2 and Voigt profile fits are shown in Fig. C2.

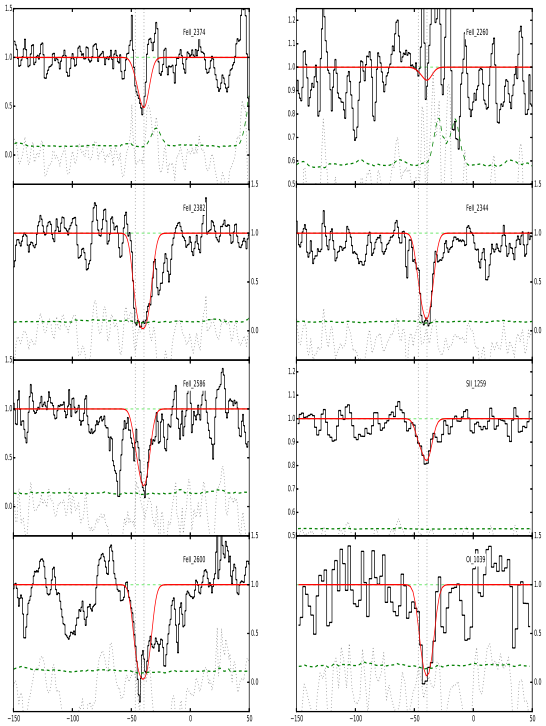

Figure C2. QSOJ0008-2901

C3 QSO J0018-0913 z_{em} = 0.75593, z_{abs} = 0.584, log N(HI) = 20.11 ± 0.10

We detect in this low-redshift absorber's spectrum the following low-ionization ions: FeII λλλ 2344 2374 and 2382. The profile is fitted using 11 components, spread over a velocity range of about 200km/s, resulting in an abundance for FeII of log N(FeII) = 13.87 ± 0.03. The main component is located on the blue edge of the profile and is accounting for about 40% of the total abundance. Also, we derive upper limits from non detection of ZnII λ 2026, log N(ZnII) < 12.41, CrII λ 2056, log N(CrII) < 12.97, TiII λ 3384, log N(TiII) < 11.57, MgI λ 2026, log N(MgI) < 13.04, NaI λ 3303.3 and log N(NaI) < 13.15.

The metallicity for this low-redshift sub-DLA is surprisingly low (even considering the α-enhancement correction of ∼ .4 dex), [Fe/H] = −1.70±0.13. It may be an effect of dust depletion, but we are unable to conclude on this particular issue due to the low number of detected ions. The metallicity derived here is therefore to be considered as a lower limit.

There is no coverage of the high-ionization ions due to the low redshift of the absorber.

The parameter fits of the individual components are listed in Table C3 and the corresponding Voigt profile fits are shown in Fig. C3.

Table C3. Voigt profile fit parameters to the low-ionization species for the z_{abs}=0.584 log N(H I)=20.11 ± 0.1 absorber towards QSO J0018-0913.

Comp.	z_{abs}	b km s^{-1}	Ion	log N cm^{-2}
1	0.58304	5.4 ± 0.3	FeII	13.51 ± 0.04
2	0.58322	13.0 ± 5.4	FeII	12.60 ± 0.14
3	0.58332	2.5 ± 0.7	FeII	12.90 ± 0.09
4	0.58339	3.1 ± 5.3	FeII	12.28 ± 0.13
5	0.58346	3.3 ± 1.2	FeII	12.78 ± 0.06
6	0.58353	3.5 ± 3.5	FeII	11.96 ± 0.17
7	0.58365	13.4 ± 14.9	FeII	12.15 ± 0.43
8	0.58378	3.8 ± 2.1	FeII	12.69 ± 0.10
9	0.58386	2.0 ± 3.1	FeII	12.33 ± 0.19
10	0.58397	6.7 ± 0.8	FeII	12.98 ± 0.03
11	0.58406	3.8 ± 1.2	FeII	12.57 ± 0.05

C4 QSOJ0041-4936 z_{em} = 3.24, z_{abs} = 2.248, log N(HI) = 20.46 ± 0.13

This spectrum covers many low-ionization transitions associated with the absorber: SII λ 1259, ZnII λ 2026, FeII λ 1608, SiII λλ 1808, 1526 and AlII λ 1670. The velocity profile can be conveniently separated into a group of red and blue components. The overall profile is well fitted with 4 components. Interestingly, the blue group which is weaker than its red counterpart is only detected in SII λ 1259, SiII λ 1526

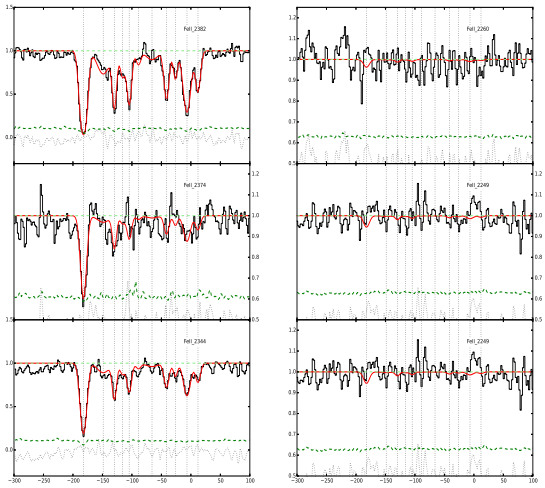

Figure C3. QSOJ0018-0913

and AlII λ 1670. Conversely, the red group of components is saturated in the case of the last two transitions. Therefore, these two groups are fitted separately: the blue-component group is fitted with two components using the lines of SiII λ 1526 and AlII λ 1670. The SII λ 1259 line is too blended to provide useful information and we derive an upper limit of $\log \mathrm{N(SII)} < 14.82$. The red-component group includes ZnII λ 2026, FeII λ 1608 and SiII λ 1808. It is also fitted with two components given the asymmetrical profile of FeII λ 1608. A fifth component redward of the profile is considered for SII λ 1526 and AlII λ 1670. The resulting column densities are: log N(FeII)=14.43 $\pm$ 0.04, log N(ZnII)=11.70 $\pm$ 0.10, log N(SiII)=14.78 $\pm$ 0.03, log N(NiII)=13.07 $\pm$ 0.07 and log N(CrII)=13.12$\pm$0.45. We detect four NI absorption lines NI $\lambda\lambda\lambda\lambda$ 1199.5, 1134.1, 1134.4 and 1134.9. The profile is fitted with the low-ionization profile in this case. In spite of the modest SNR, a satisfactory fit is found for NI $\lambda\lambda\lambda$ 1134.1, 1134.9 and 1199.5, while the remaining line (NI λ 1134.4) appears to be blended. The resulting column density is log N(NI)=14.03 $\pm$ 0.03. Finally, the AlII λ 1670 line is saturated thus providing a lower limit on the column density: $\log \mathrm{N(AlII)} > 14.06$.

Regarding the high-ionization ions, the CIV doublet $\lambda\lambda$ 1548 and 1550 is covered by the EUADP spectrum. In addition, the intermediate-ionization AlIII transitions $\lambda\lambda$ 1854 and 1862 are present and match well the high-ionization profile. In the case of the CIV doublet, the CIV λ 1550 is blended with a broad line in the blue part ($\mathrm{v} < -120$km/s), whereas CIV λ 1548 seems blended in the red part ($\mathrm{v} > -120$km/s). In addition, the AlIII transition shows absorption features in the red part of the profile only. A 6-component profile is used to fit the red part of the profile (using transitions from CIV λ 1550, AlIII $\lambda\lambda$ 1862 and 1854) and one-component is used to fit the blue part of the profile (using CIV λ 1548 at $\mathrm{v} \sim -240$km/s). This results in an estimated column density of AlIII $\log \mathrm{N(AlIII)} = 12.90 \pm 0.01$ and a lower limit (blending) for CIV $\log \mathrm{N(CIV)} > 14.56$.

The parameter fits are summarised in Table C4 and Voigt profile fits are shown in Fig. C4.

Table C4. Voigt profile fit parameters to the low-, intermediate- and high-ionization species for the z_{abs}=2.248 log N(H I)=20.46± 0.13 absorber towards QSO J0041-4936.

Comp.	z_{abs}	b km s^{-1}	Ion	log N cm^{-2}
1	2.24785	4.6 ± 0.8	FeII	12.01 ± 0.35
			ZnII	–
			SiII	12.85 ± 0.04
			NiII	–
			CrII	–
			AlII	11.28 ± 0.05
			SII	< 13.24
			NI	12.38 ± 0.17
2	2.24799	7.3 ± 0.4	FeII	12.01 ± 0.35
			ZnII	–
			SiII	13.12 ± 0.02
			NiII	–
			CrII	–
			AlII	11.78 ± 0.02
			SII	< 14.04
			NI	12.80 ± 0.07
3	2.24840	10.2 ± 0.9	FeII	13.71 ± 0.05
			ZnII	11.03 ± 0.36
			SiII	14.35 ± 0.06
			NiII	12.80 ± 0.10
			CrII	12.73 ± 0.91
			AlII	> 13.11
			SII	< 14.38
			NI	12.58 ± 0.15
4	2.24852	3.8 ± 0.2	FeII	14.33 ± 0.05
			ZnII	11.59 ± 0.09
			SiII	14.54 ± 0.04
			NiII	12.74 ± 0.09
			CrII	12.89 ± 0.44
			AlII	> 15.13
			SII	< 14.48
			NI	14.25 ± 0.04
5	2.24866	8.0 ± 0.3	FeII	–
			ZnII	–
			SiII	13.13 ± 0.02
			NiII	–
			CrII	–
			AlII	12.09 ± 0.02
			SII	–
			NI	–
1	2.24547	3.5 ± 0.5	CIV	12.84 ± 0.02
			AlIII	–
2	2.24696	4.1 ± 0.4	CIV	13.21 ± 0.01
			AlIII	–
3	2.24757	12.1 ± 0.7	CIV	13.24 ± 0.01
			AlIII	11.25 ± 0.06
4	2.24797	13.1 ± 0.1	CIV	14.32 ± 0.01
			AlIII	12.28 ± 0.01
5	2.24835	8.7 ± 0.3	CIV	13.58 ± 0.10
			AlIII	12.37 ± 0.01
6	2.24845	19.6 ± 0.4	CIV	13.87 ± 0.01
			AlIII	12.36 ± 0.01
7	2.24853	2.6 ± 0.7	CIV	–
			AlIII	12.08 ± 0.01

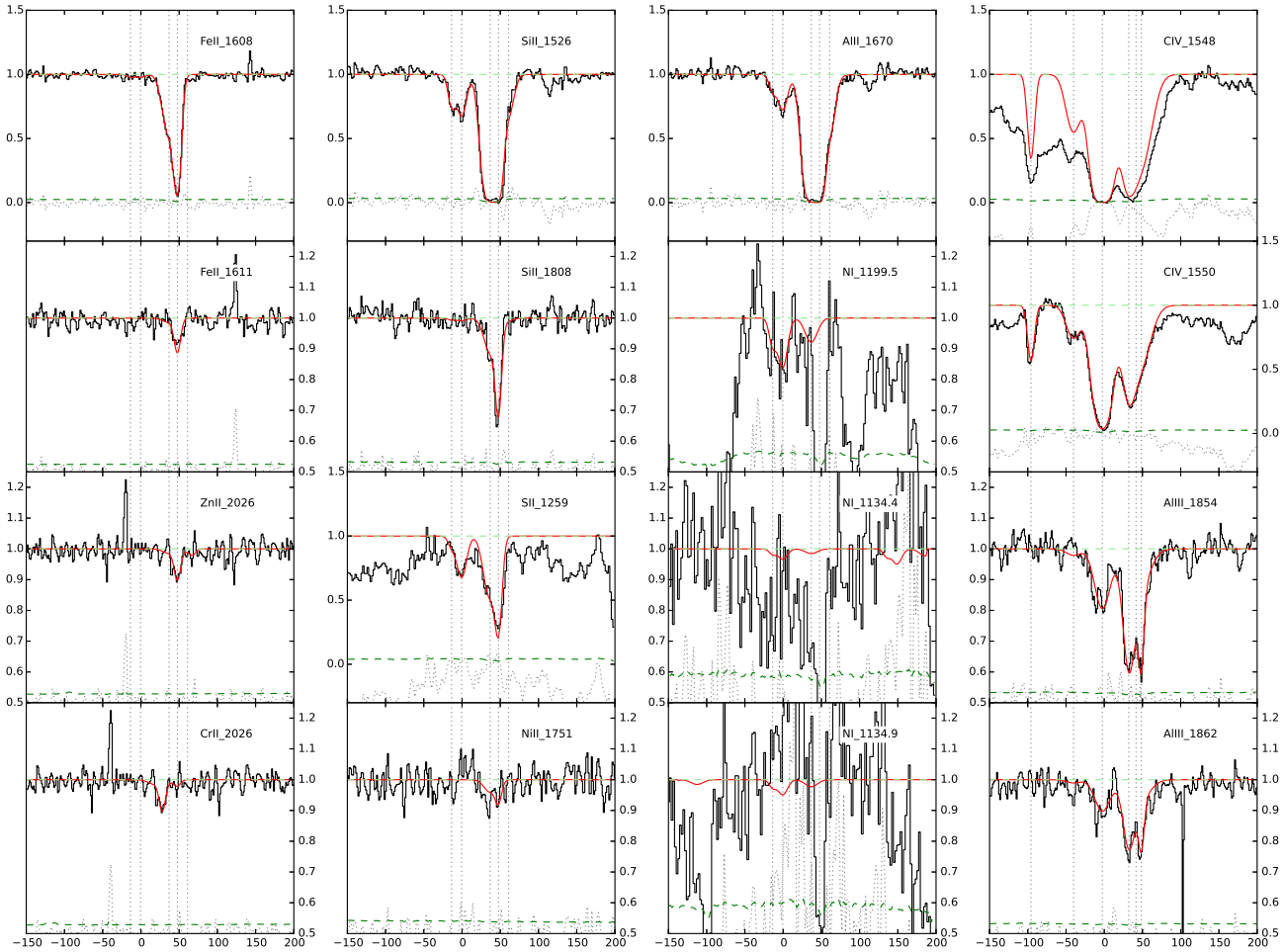

Figure C4. QSOJ0041-4936

Table C5. Voigt profile fit parameters to the low-ionization species for the z_{abs}=1.857 log N(H I)=20.21 ± 0.09 absorber towards QSO B0128-2150.

Comp.	z_{abs}	b km s^{-1}	Ion	log N cm^{-2}
1	1.85610	11.8 ± 2.1	FeII	12.91 ± 0.06
			SiII	13.93 ± 0.10
			SII	12.98 ± 0.29
			AlIII	12.02 ± 0.05
			NiII	–
2	1.85627	4.5 ± 0.7	FeII	13.16 ± 0.04
			SiII	13.71 ± 0.12
			SII	13.23 ± 0.12
			AlIII	11.76 ± 0.07
			NiII	11.80 ± 0.67
3	1.85641	4.3 ± 0.3	FeII	13.82 ± 0.01
			SiII	14.19 ± 0.04
			SII	13.77 ± 0.04
			AlIII	11.94 ± 0.03
			NiII	12.66 ± 0.1
4	1.85655	7.0 ± 0.2	FeII	14.14 ± 0.01
			SiII	14.44 ± 0.01
			SII	13.94 ± 0.03
			AlIII	12.37 ± 0.01
			NiII	12.89 ± 0.06
5	1.85676	4.6 ± 0.2	FeII	13.69 ± 0.01
			SiII	13.99 ± 0.05
			SII	13.60 ± 0.05
			AlIII	12.08 ± 0.02
			NiII	12.73 ± 0.08

C5 QSO B0128-2150 $\mathbf{z_{em}}$ = 1.9, $\mathbf{z_{abs}}$ = 1.857, log N(HI) = 20.21 ± 0.09

For this low-redshift absorber, the EUADP spectrum covers a number of the low-ionization ions including FeII λλλ 2374 2260 2249, NiII λλλ 1751 1741 1709, SII λλλ 1259 1253 1250 and SiII λ 1808. The detected intermediate-ionization transitions, AlIII λλ 1854 and 1862 show the same velocity profile as the low-ionization ions. A 5-component Voigt profile is used to fit FeII λλ 2374 2249, SiII λ 1808 SII λ1259, AlIII λ 1854 and NiII λ 1709. The full absorption profile extends to a velocity range of about 100 km/s. The resulting total column densities are log N(FeII)=14.44 ± 0.01, log N(SiII)=14.82 ± 0.02, log N(SII)=14.33 ± 0.03, log N(NiII)=13.26 ± 0.05 and log N(AlIII)=12.78 ± 0.01. In addition, CII λ 1334 is detected but, as often in DLAs, heavily saturated. Finally, the non-detection of both ZnII λ 2062 and MgI λ 1827 provides robust column density upper limits: $\log N(ZnII) < 12.26$, and log N(MgI) < 13.21.

We note that no high-ionization species are covered by this spectrum.

The parameter fits are summarised in Table C5 and Voigt profile fits are shown in Fig. C5.

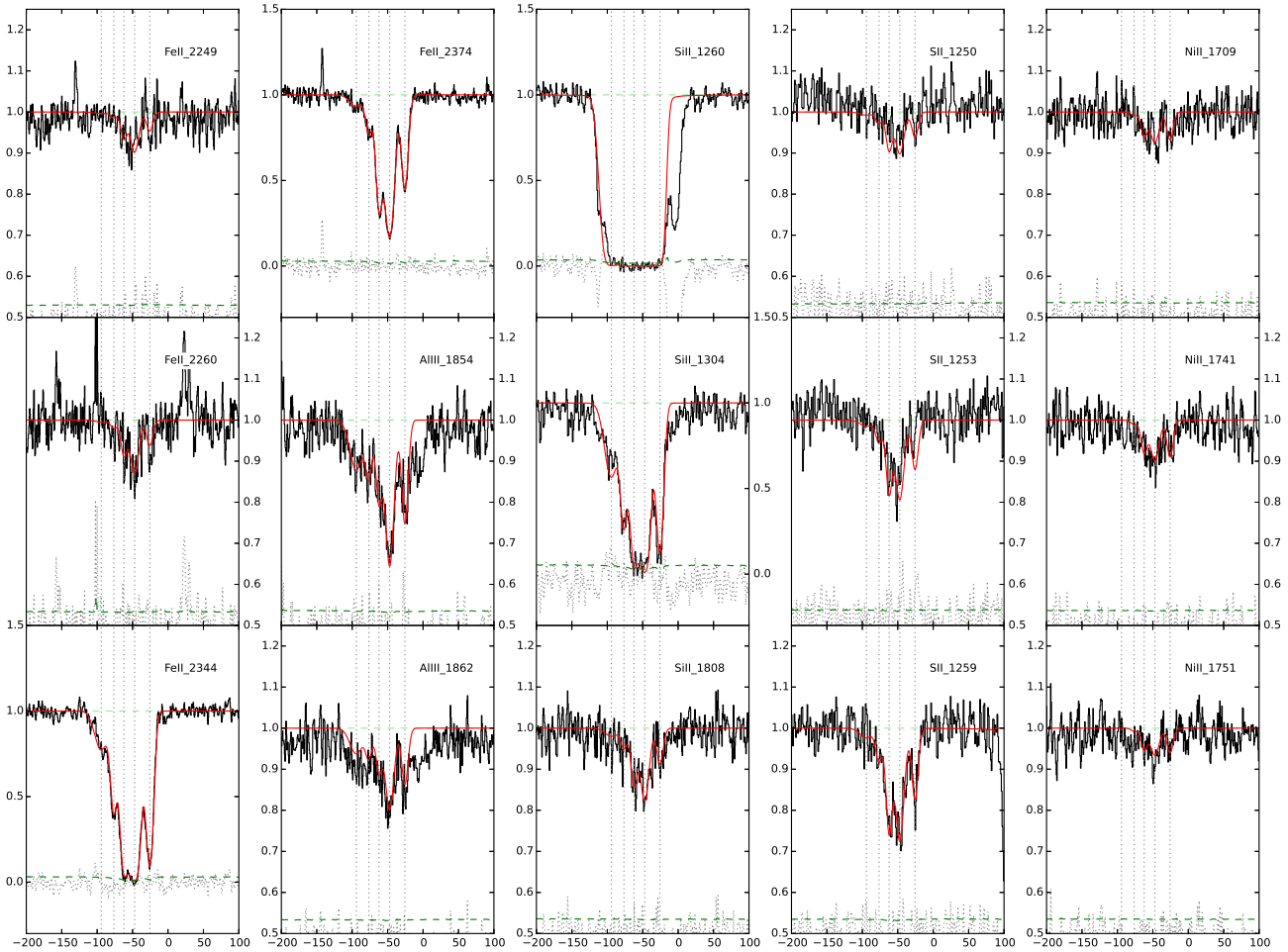

Figure C5. QSOB0128-2150

Table C6. Voigt profile fit parameters to the low-ionization species for the z_{abs}=0.647 log N(H I)=20.60 ± 0.12 absorber towards QSO J0132-0823.

Comp.	z_{abs}	b km s^{-1}	Ion	log N cm^{-2}
1	0.64612	10.7 ± 2.3	FeII	13.38 ± 0.08
			TiII	11.53 ± 0.44
			MgI	10.62 ± 1.76
2	0.64635	15.6 ± 1.2	FeII	14.72 ± 0.09
			TiII	12.15 ± 0.10
			MgI	12.37 ± 0.04
3	0.64658	14.4 ± 2.1	FeII	14.52 ± 0.11
			TiII	11.75 ± 0.21
			MgI	12.13 ± 0.06
4	0.64677	10.8 ± 3.0	FeII	13.35 ± 0.13
			TiII	11.12 ± 0.77
			MgI	11.43 ± 0.19

C6 QSO J0132-0823 $z_{em} = 1.121$, $z_{abs} = 0.6467$, log N(HI) = 20.60 ± 0.12

A few ions are covered and detected in this low-redshift absorber's spectrum: FeII λλ 2249 2260, MgI λ 2582 and TiII λλ 3242 and 3384. The absorption is weak, we use the MgI profile to derive the two main components. The saturated FeII λ 2344 unveils two weak components on either side of the profile. This results in abundances of FeII log N(FeII) = 14.96 ± 0.07, of TiII log N(TiII) = 12.39 ± 0.11 and of MgI log N(MgI) = 12.60 ± 0.04.

The overall SNR (< 10) gives a reasonable upper limit for CrII, using CrII λ 2056, of log N(CrII) < 13.17. ZnII and CII are also covered, but the best upper limits we can derive are above 16.30.

There is no coverage of the high-ionization ions due to the low redshift of the absorber.

The parameter fits of the individual components are listed in Table C6 and the corresponding Voigt profile fits are shown in Fig. C6.

C7 QSO B0307-195B $z_{em} = 2.122$, $z_{abs} = 1.788$, log N(HI) = 19.0 ± 0.10

Many low-ionization ions are detected in this low-redshift absorber including MgI λ 2852, FeII λλλλλλ 2374, 1608, 2586, 2344, 2382, 2600, SiII λλλ 1808, 1304, 1526, MgII λλ 2803, 2796, AlII λ 1670, AlIII λλ 1862, 1854, CIV λλ 1550, 1548 and SiIV λλ 1402, 1393. The absorption profile presents two distinct parts, one in the red (5 components), the other one in the blue (3 components), with a total velocity ranging about 300 km/s. The fit is performed using the transitions which are free from any saturation i.e. FeII λλλ 2374 1608 2586, SiII λ 1808 and MgI λ 2852. The FeII λ 2586 line in particular is not considered for the final fits given the medium quality of the EUADP spectrum around v = 50km/s. The resulting total column densities are: log N(FeII)=14.48 ± 0.004, log N(SiII)=15.0 ± 0.01 and log N(MgI)=12.54 ± 0.01. In addition to these measures, the non-detection of CrII λ 2056, MnII λ 2594, NiII λ 1751, and ZnII λ 2062 is used to derive the following upper limits log N(CrII) < 12.77, log N(MnII) < 12.13, log N(NiII) < 13.22 and log N(ZnII) < 12.18.

The high-ionization doublets of CIV λλ 1548 1550 and

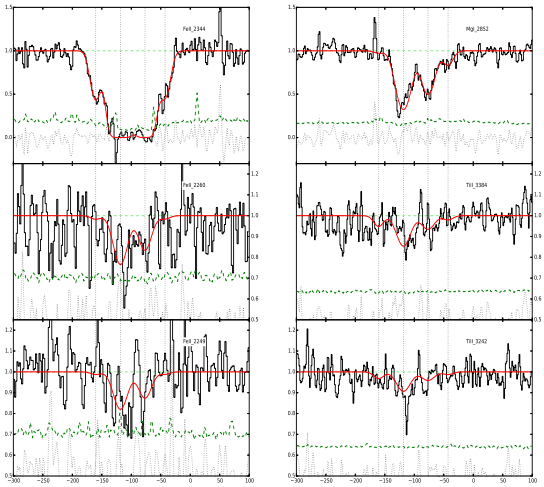

Figure C6. QSOJ0132-0823

SiIV λλ 1393 and 1402 are detected in the spectrum albeit indicating strong saturation. A 7-component profile is used to fit these four transitions resulting in lower limits to the total column densities of log N(SiIV) > 14.55 and log N(CIV) > 15.13. Interestingly, in this absorber, the velocity range of the high-ionization ion profile matches the one from the low-ionization ions extending to about 300 km/s.

The resulting parameter fits for the low- and high-ionization profiles are listed in Table C7 and the corresponding Voigt profile fits are shown in Fig. C7.

Table C7. Voigt profile fit parameters to the low- and high-ionization species for the z_{abs}=1.788 log N(H I)=19.00 ± 0.10 absorber towards QSO B0307-195B.

Comp.	z_{abs}	b km s^{-1}	Ion	log N cm^{-2}
1	1.78744	7.8 ± 0.1	FeII	13.99 ± 0.01
			SiII	14.53 ± 0.01
			MgI	11.83 ± 0.01
2	1.78763	4.3 ± 0.1	FeII	13.61 ± 0.01
			SiII	14.14 ± 0.03
			MgI	11.90 ± 0.01
3	1.78788	8.6 ± 0.4	FeII	13.54 ± 0.01
			SiII	13.99 ± 0.04
			MgI	11.16 ± 0.03
4	1.78847	9.9 ± 0.1	FeII	13.42 ± 0.02
			SiII	13.60 ± 0.11
			MgI	11.61 ± 0.01
5	1.78863	8.2 ± 0.2	FeII	13.58 ± 0.01
			SiII	14.31 ± 0.02
			MgI	11.87 ± 0.01
6	1.78885	8.2 ± 0.2	FeII	13.64 ± 0.01
			SiII	14.25 ± 0.02
			MgI	11.72 ± 0.01
7	1.78929	7.0 ± 0.7	FeII	13.11 ± 0.03
			SiII	13.13 ± 0.26
			MgI	11.14 ± 0.03
8	1.78949	8.9 ± 2.0	FeII	12.95 ± 0.05
			SiII	–
			MgI	10.90 ± 0.07
1	1.78748	19.8 ± 0.3	SiIV	13.27 ± 0.01
			CIV	13.68 ± 0.01
2	1.78796	15.1 ± 0.6	SiIV	13.10 ± 0.03
			CIV	13.46 ± 0.03
3	1.78826	18.6 ± 1.1	SiIV	13.50 ± 0.03
			CIV	14.08 ± 0.03
4	1.78865	19.8 ± 0.5	SiIV	14.37 ± 0.02
			CIV	14.89 ± 0.02
5	1.78921	32.5 ± 1.3	SiIV	13.58 ± 0.02
			CIV	14.42 ± 0.01
6	1.78970	18.9 ± 0.6	SiIV	13.15 ± 0.02
			CIV	13.97 ± 0.02
7	1.78981	5.0 ± 0.3	SiIV	12.78 ± 0.02
			CIV	13.25 ± 0.04

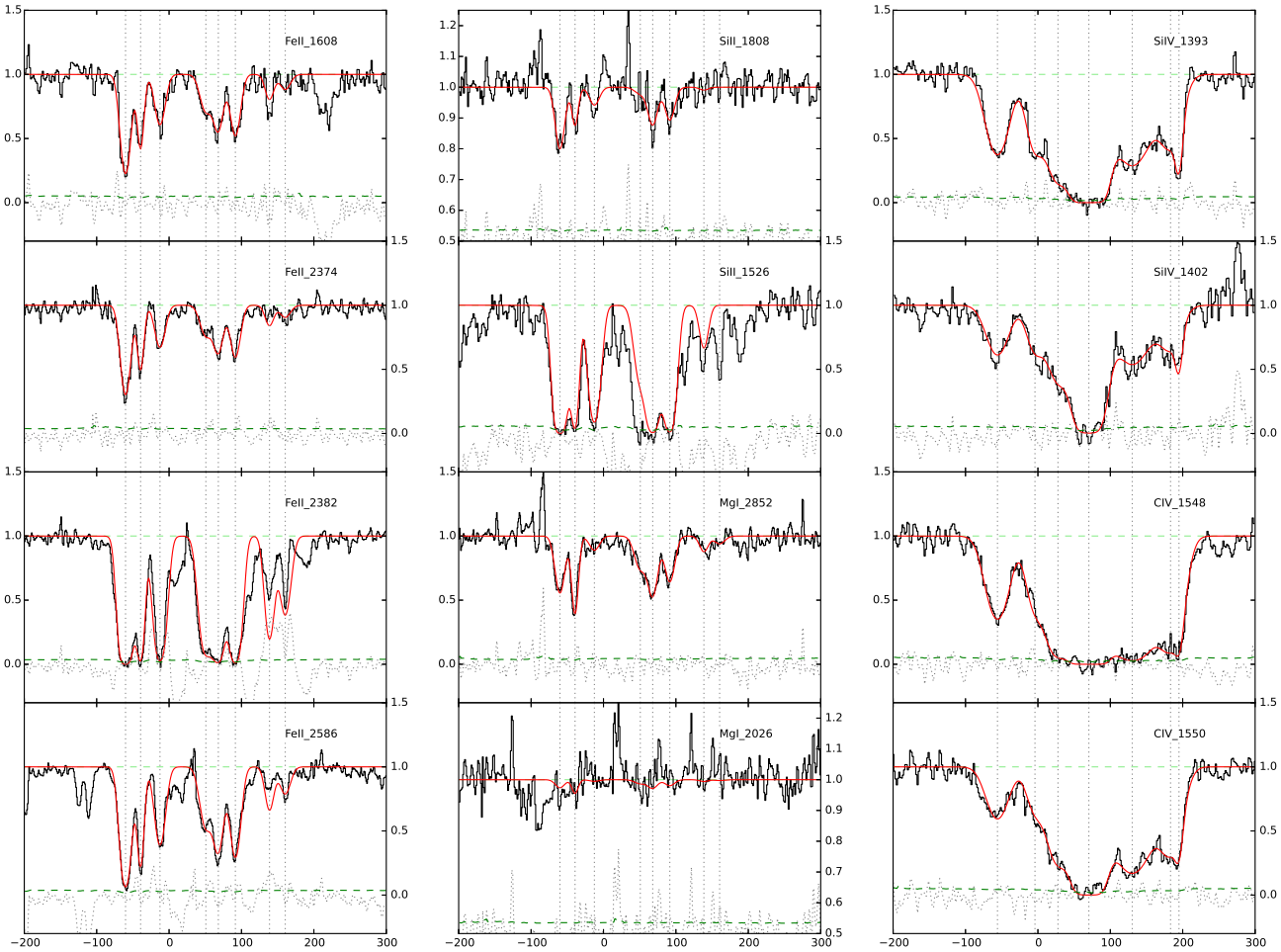

Figure C7. QSOB0307-195B

Table C8. Voigt profile fit parameters to the low- and high-ionization species for the z_{abs}=1.562 log N(H I)=19.35 ± 0.10 absorber towards QSO J0427-1302.

Comp.	z_{abs}	b km s^{-1}	Ion	log N cm^{-2}
1	1.5631845	7.2 ± 1.4	AlII	11.78 ± 0.10
			FeII	-
2	1.5632172	2.9 ± 0.6	AlII	-
			FeII	12.23 ± 0.04
1	1.56065	17.4 ± 2.7	SiIV	12.96 ± 0.08
2	1.56075	3.1 ± 2.4	SiIV	12.31 ± 0.22
3	1.56089	4.6 ± 1.0	SiIV	12.73 ± 0.06
4	1.56101	1.5 ± 0.7	SiIV	12.93 ± 0.62
5	1.56126	23.8 ± 8.3	SiIV	12.85 ± 0.12
6	1.56143	1.2 ± 2.0	SiIV	12.13 ± 0.39
7	1.56165	12.8 ± 1.0	SiIV	13.27 ± 0.03
8	1.56197	12.7 ± 1.8	SiIV	12.81 ± 0.04
9	1.56228	6.4 ± 2.5	SiIV	12.33 ± 0.08
10	1.56270	25.4 ± 5.2	SiIV	12.49 ± 0.08
11	1.56309	2.0 ± 2.0	SiIV	12.35 ± 0.17
12	1.56321	6.4 ± 0.6	SiIV	13.15 ± 0.03

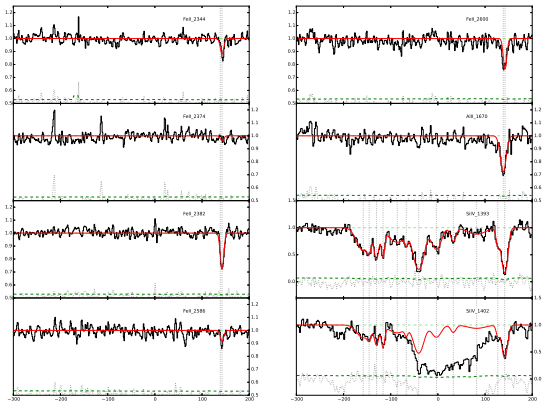

Figure C8. QSOJ0427-1302

C8 QSO J0427-1302 z_{em} = 2.166, z_{abs} = 1.562, log N(HI) = 19.35 ± 0.10

The low-ionization transitions in this low-redshift system are well fitted with two components, the redshift and Doppler parameter of which are fixed by a simultaneous fit of FeII λλλλ 2344, 2382, 2586, 2600 and AlII λ 1670. The 2-component fit shows an interesting asymmetric distribution of FeII and AlII abundances: the blue component is stronger for FeII while the red component is stronger for AlII. The resulting column densities are log N(FeII)=12.23±0.04 and log N(AlII)=11.78 ± 0.1. In addition, the non detection of CrII λ 2056, MgI λ 2026, MnII λ 2576, NiII λ 1741, and ZnII λ 2026 leads to the following upper limits: log N(CrII) < 12.39, log N(MgI) < 12.38, log N(MnII) < 11.84, log N(NiII) < 13.23 and log N(ZnII) < 11.75.

In addition to these low-ionization transitions, the EUADP spectrum covers several high-ionization species. The doublet of CIV λλ 1550, 1548 and SiIV λλ 1393 and 1402 expand a velocity range of about 250 km/s. The CIV transitions are strongly saturated and SiIV λ 1402 appears to be blended (greater absorption in spite of a lower oscillation factor than SiIV λ 1393). Thus the fit is performed using the SiIV λ 1393 line, considering a total of 12 components, with the redder one being associated with the low-ionization profile (v ∼140 km/s). Many of the strongest components fitted for SiIV λ 1393 match the velocity profiles of the CIV doublet. We obtain log N(SiIV) = 13.9 ± 0.07.

The parameter fits are listed in Table C8 and the corresponding Voigt profile fits are shown in Fig. C8.

C9 QSO PKS0454-220 z_{em} = 0.534, z_{abs} = 0.474, log N(HI) = 19.45 ± 0.03

This low-redshift absorption system contains a great number of transitions including three MnII lines: MnII λλλ 2576, 2594, 2606, and seven FeII lines (four of which are saturated): FeII λλλλλλλ 2249, 2260, 2374, 2344, 2382, 2586 and 2600. It is interesting to notice the presence of a component in the blue part of the saturated lines which is not detected in the weaker transitions. Therefore, the fit is performed in two separate steps: on one hand the unsaturated lines are used to constrain the strongest components, on the other hand, this solution is applied to the saturated profiles to check its validity and to constrain the blue component. The absorption profile results in a total of seven components (five strong components as well as one blue and one red additional weaker components), spread in a velocity range of about 150 km/s. The column densities derived are log N(FeII)=14.71 ± 0.01 and log N(MnII)=12.58 ± 0.01.

In this EUADP spectrum, no high-ionisation transitions are covered for this low-redshift absorber.

The parameter fits are summarised in Table C9 and Voigt profile fits are shown in Fig. C9.

Table C9. Voigt profile fit parameters to the low-ionization species for the z_{abs}=0.474 log N(H I)=19.45 ± 0.03 absorber towards QSO PKS 0454-220.

Comp.	z_{abs}	b km s^{-1}	Ion	log N cm^{-2}
1	0.47405	14.3 ± 0.6	FeII	12.39 ± 0.02
			MnII	11.12 ± 0.07
2	0.47422	14.5 ± 0.2	FeII	13.38 ± 0.01
			MnII	11.46 ± 0.03
3	0.47432	4.0 ± 0.1	FeII	14.00 ± 0.02
			MnII	11.65 ± 0.02
4	0.47439	10.0 ± 0.2	FeII	14.26 ± 0.01
			MnII	12.09 ± 0.01
5	0.47448	18.5 ± 0.2	FeII	14.12 ± 0.01
			MnII	12.03 ± 0.01
6	0.47466	6.5 ± 0.1	FeII	13.81 ± 0.01
			MnII	11.48 ± 0.04
7	0.47468	14.9 ± 0.3	FeII	13.11 ± 0.04
			MnII	11.50 ± 0.06

C10 QSOJ0600-5040 z_{em} = 3.13, z_{abs} = 2.149, log N(HI) = 20.4 ± 0.12

The EUADP spectrum for this absorber covers many low-ionization transitions including FeII λλ 1608, 1611, AlII λ

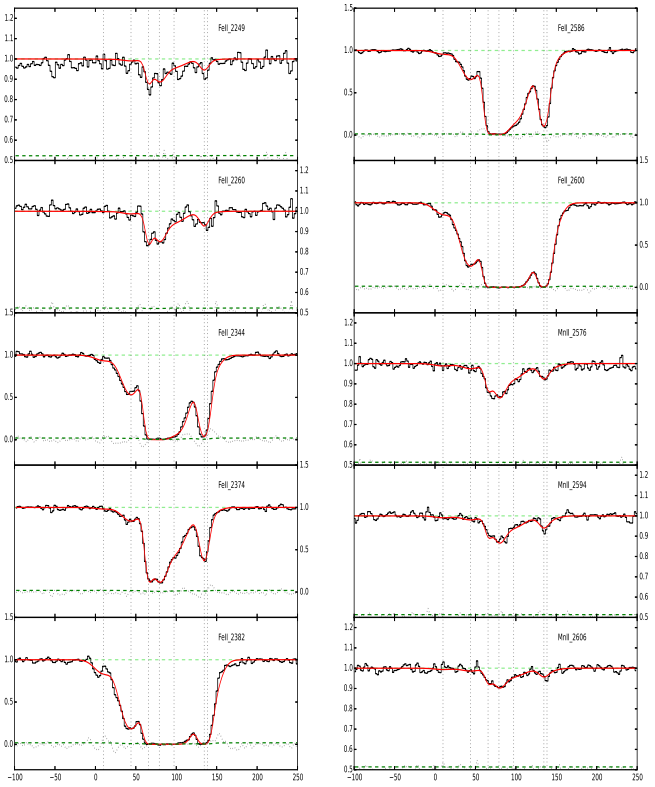

Figure C9. QSOPKS0454-220

1670, SiII λλλλ 1193, 1526, 1304, 1808, ZnII λ 2062, CrII λλ 2062, 2026, NiII λλλ 1709, 1741 and 1751. The absorption profile is clearly multi-component and covers a large velocity range of about 100 km/s based on the strongest transitions (namely AlII λ 1670, FeII λ 1608, SiII λλλ 1193, 1526 and 1304). The profile is well fitted with four components. This velocity profile is then applied to the weakest ZnII λ 2026 line. It reveals a blend in the first two components related to the CrII λ 2062 line which is therefore fitted simultaneously. The AlII λ 1670 line is saturated, leading to a lower limit estimate in the column density of log N(AlII) > 14.33 based on the four component profile (redshifts and Doppler parameters) described above. The AlIII λλ 1854 and 1862 profiles follow the low-ionization ions. However, a blend in AlIII λ 1854 complicates the fit so that the velocity of the first component is fixed to the value derived above. The resulting column densities are: log N(FeII)=14.84 ± 0.03, log N(SiII)=15.08 ± 0.01, log N(NiII)=13.62 ± 0.02, log N(CrII)=13.10 ± 0.01, log N(ZnII)=12.11 ± 0.03 and log N(AlIII)=12.78 ± 0.01.

In this EUADP spectrum, the high-ionization ions SiIV λλ 1393, 1402, and CIV λλ 1548 and 1550 are covered but are located in the forest, and hence suffer from important blending.

Table C10. Voigt profile fit parameters to the low- and intermediate-ionization species for the z_{abs}=2.533 log N(H I)=20.4 ± 0.12 absorber towards QSO J060008.1-504036.

Comp.	z_{abs}	b km s^{-1}	Ion	log N cm^{-2}
1	2.14895	2.2 ± 0.7	FeII	13.22 ± 0.04
			SiII	–
			NiII	12.06 ± 0.18
			CrII	11.50 ± 0.22
			ZnII	–
			AlIII	11.60 ± 0.02
			AlII	> 14.2
2	2.14917	14.1 ± 0.4	FeII	14.1 ± 0.01
			SiII	14.55 ± 0.02
			NiII	13.16 ± 0.03
			CrII	12.33 ± 0.06
			ZnII	–
			AlIII	12.20 ± 0.01
			AlII	> 13.1
3	2.14959	9.1 ± 0.3	FeII	14.58 ± 0.01
			SiII	14.84 ± 0.01
			NiII	13.29 ± 0.02
			CrII	12.83 ± 0.01
			ZnII	11.97 ± 0.03
			AlIII	12.54 ± 0.01
			AlII	> 13.50
4	2.14986	4.7 ± 0.3	FeII	14.26 ± 0.06
			SiII	14.21 ± 0.03
			NiII	12.81 ± 0.04
			CrII	12.54 ± 0.02
			ZnII	11.56 ± 0.06
			AlIII	11.79 ± 0.02
			AlII	> 13.10

The parameter fits are summarized in Table C10 and Voigt profile fits are shown in Fig. C10.

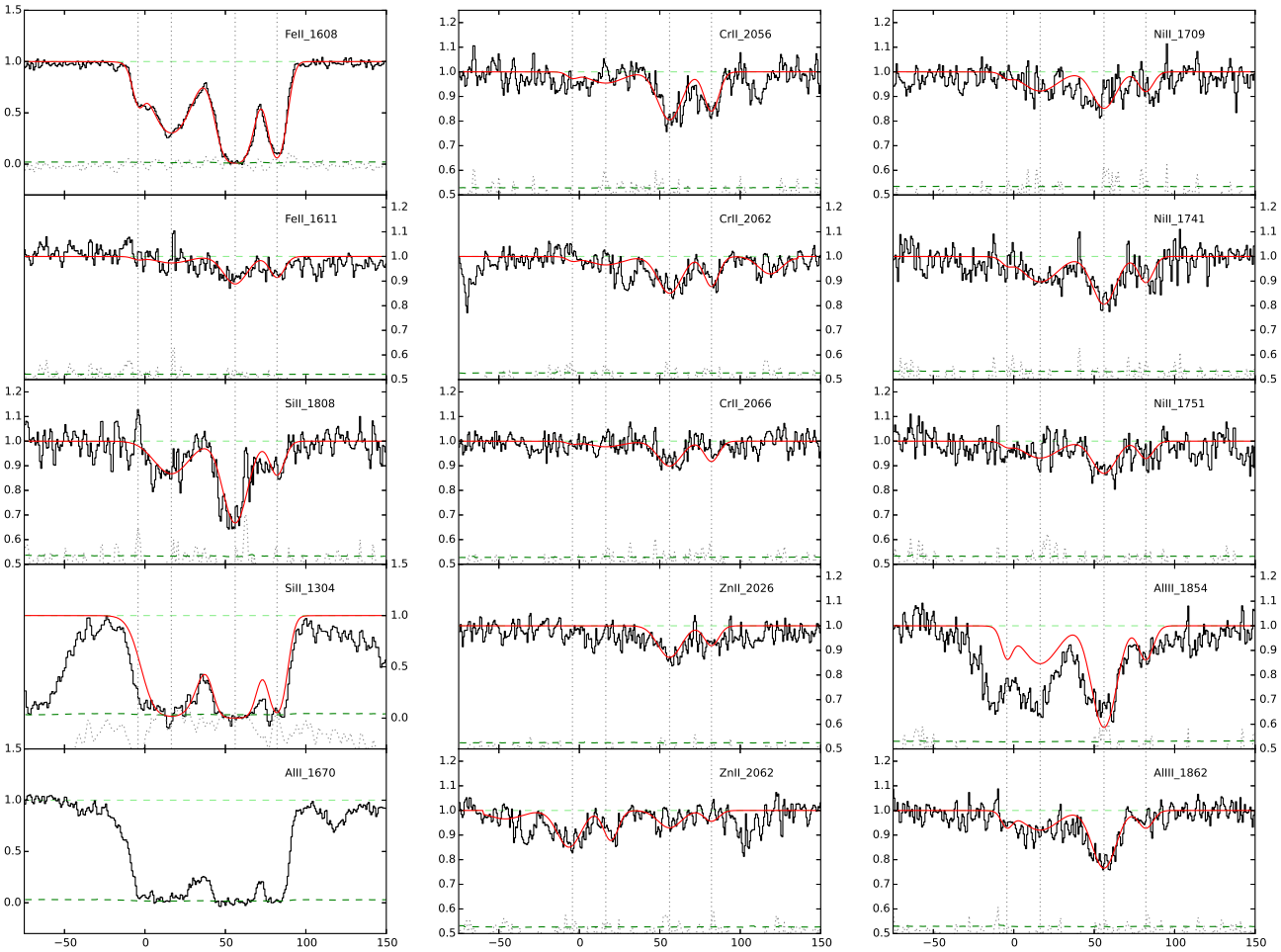

Figure C10. QSOJ0600-5040

C11 QSO B1036-2257 $\mathbf{z}_{\rm em} = 3.13$, $\mathbf{z}_{\rm abs} = 2.533$, $\log \mathrm{N(HI)} = 19.3 \pm 0.10$

A large number of low-ionisation elements are detected in the EUADP spectrum including SiII $\lambda\lambda\lambda\lambda$ 1190, 1193, 1260, 1526, CII $\lambda\lambda$ 1036, 1334, MgII $\lambda\lambda$ 2803 and 2796, AlII λ 1670, AlIII λ 1862 and FeII $\lambda\lambda$ 2382, 2600. Based on the SiII $\lambda\lambda$ 1193 and 1260 lines which are free from any saturation and blending, eleven components are used to fit the absorption profile. The low-ionization transitions for this system cover a large velocity range of about 200 km/s. The strongest components of this profile are used to fit AlII λ 1670, FeII $\lambda\lambda$ 2600, 2382 and AlIII λ 1862. The resulting column densities are log N(SiII)=13.64 ± 0.01, log N(AlII)=12.52 ± 0.01, log N(AlIII)=12.89 ± 0.02 and log N(FeII)=12.93 ± 0.01. The profile estimated from the weakest transition is then used to fit the saturated CII λ 1334 revealing a $12^{\rm th}$ component around $v = 0$ km/s. A manual fit using CII $\lambda\lambda$ 1036 and 1334 and the previous solution provides the following lower limit for CII $\log \mathrm{N(CII)} > 15.98$. Nevertheless, both lines are contaminated with unrelated absorbers, which prevents us from deriving a robust estimate of the lower limit in CII.

A great number of high-ionization lines are detected in this EUADP spectra including OVI $\lambda\lambda$ 1031, 1037, NV $\lambda\lambda$ 1238, 1242, CIV $\lambda\lambda$ 1548, 1550, SiIV $\lambda\lambda$ 1393 and 1402. A number of these lines are located in the Lyman-α forest (SiIV doublet, NV λ1242 and OVI λ 1031) and therefore appear to be blended. The CIV doublet is saturated in this case, such that only a lower limit is derived. Only the OVI λ 1037 and NV λ 1238 lines appear free from any saturation or blending, preventing from performing a reasonable fit. A three-component profile is used to fit SiIV λ 1393. The resulting component velocities and Doppler parameters are then used to fit the other lines available. The resulting column densities are log N(SiIV)=13.71 ± 0.01, log N(CIV)> 17.42.

The parameter fits of the individual components are listed in Table C11 and the corresponding Voigt profile fits are shown in Fig. C11.

Table C11. Voigt profile fit parameters to the low- and high-ionization species for the z_{abs}=2.533 log N(H I)=19.3 ± 0.10 absorber towards QSO B1036-2257

Comp.	z_{abs}	b km s^{-1}	Ion	log N cm^{-2}	Comp.	z_{abs}	b km s^{-1}	Ion	log N cm^{-2}
1	2.53132	5.4 ± 0.1	SiII	13.19 ± 0.01	1	2.53143	12.9 ± 0.6	CIV	12.97 ± 0.02
			FeII	12.65 ± 0.01				SiIV	12.83 ± 0.02
			AlII	12.16 ± 0.01	2	2.53158	7.8 ± 0.4	CIV	12.98 ± 0.02
			MgII	13.20 ± 0.04				SiIV	12.74 ± 0.02
			CII	14.00	3	2.53192	11.6 ± 0.8	CIV	12.83 ± 0.02
2	2.53152	11.3 ± 0.4	SiII	12.87 ± 0.03				SiIV	12.32 ± 0.04
			FeII	–	4	2.53294	13.2 ± 2.5	CIV	13.9 ± 0.01
			AlII	11.77 ± 0.03				SiIV	12.91 ± 0.01
			MgII	12.71 ± 0.03	5	2.53314	6.0 ± 2.3	CIV	> 13.85
			CII	13.81 ± 0.01				SiIV	12.78 ± 0.02
3	2.53178	2.2 ± 0.2	SiII	11.80 ± 0.10	6	2.53340	5.4 ± 4.4	CIV	> 16.57
			FeII	–				SiIV	12.98 ± 0.01
			AlII	11.14 ± 0.03	7	2.53358	3.0 ± 2.6	CIV	> 17.35
			MgII	11.49 ± 0.21				SiIV	13.15 ± 0.01
			CII	12.7					
4	2.53197	2.1 ± 0.2	SiII	12.47 ± 0.06					
			FeII	–					
			AlII	11.32 ± 0.02					
			MgII	12.37 ± 0.06					
			CII	13.60					
5	2.53220	4.3 ± 2.1	SiII	11.49 ± 0.13					
			FeII	–					
			AlII	–					
			MgII	11.19 ± 0.43					
			CII	13.00					
6	2.53248	5.3 ± 0.9	SiII	12.09 ± 0.04					
			FeII	–					
			AlII	–					
			MgII	12.11 ± 0.07					
			CII	14.00					
7	2.53275	7.8 ± 2.3	SiII	11.95 ± 0.05					
			FeII	–					
			AlII	–					
			MgII	11.27 ± 0.48					
			CII	> 15.90					
8	2.53291	7.1 ± 1.5	SiII	12.09 ± 0.04					
			FeII	–					
			AlII	–					
			MgII	12.11 ± 0.07					
			CII	> 15.00					
9	2.53313	4.0 ± 2.0	SiII	11.60 ± 0.04					
			FeII	–					
			AlII	–					
			MgII	12.14 ± 0.06					
			CII	> 14.30					
10	2.53332	5.6 ± 0.3	SiII	12.65 ± 0.01					
			FeII	12.31 ± 0.01					
			AlII	–					
			MgII	12.52 ± 0.04					
			CII	13.8					
11	2.53356	5.9 ± 0.7	SiII	12.32 ± 0.03					
			FeII	–					
			AlII	11.42 ± 0.02					
			MgII	12.35 ± 0.04					
			CII	13.55					
12	2.53382	5.0 ± 0.2	SiII	12.82 ± 0.01					
			FeII	12.30 ± 0.01					
			AlII	11.80 ± 0.01					
			MgII	12.58 ± 0.03					
			CII	13.70					

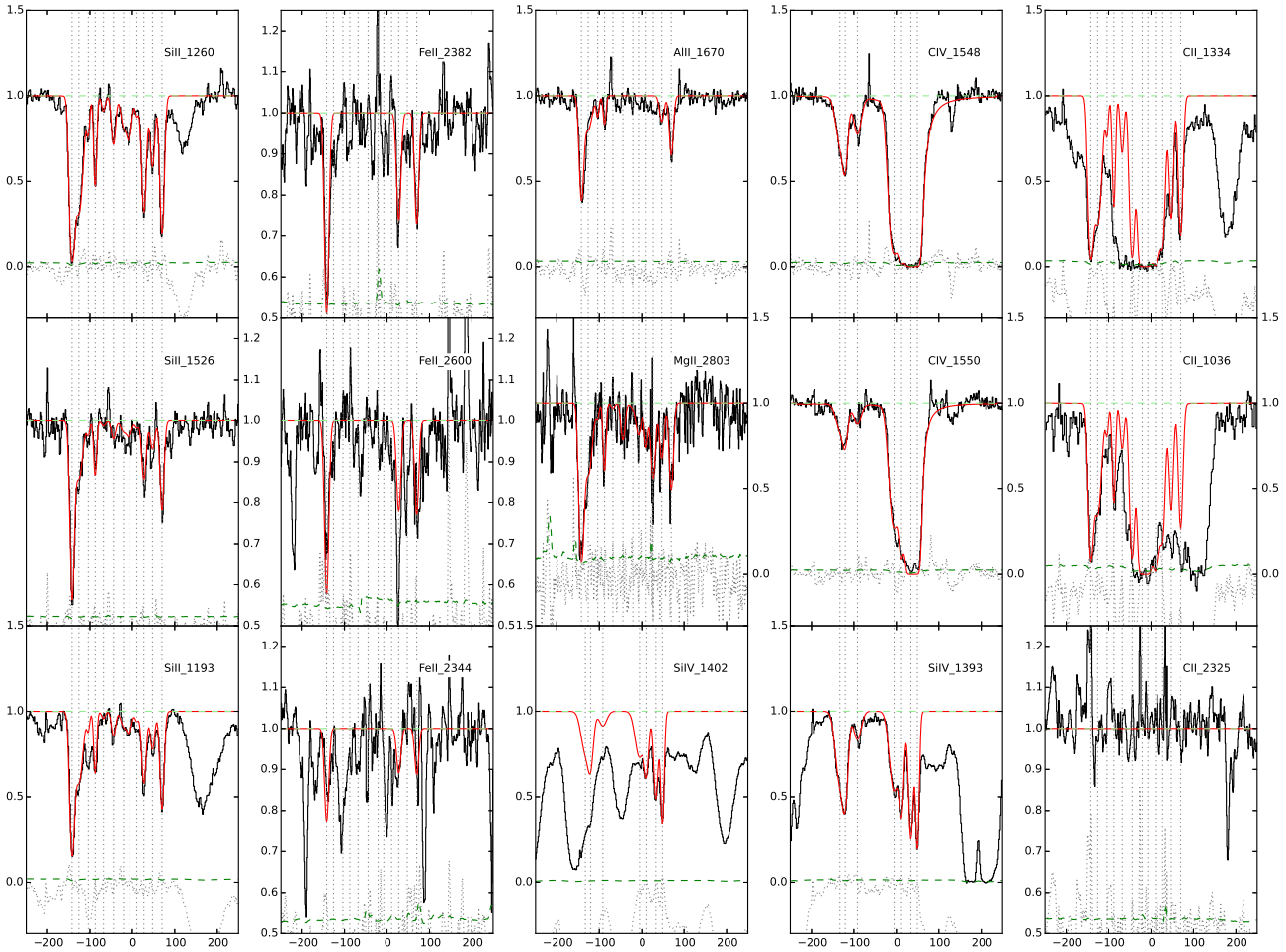

Figure C11. QSOB1036-2257

C12 QSO J115538.6+053050 $z_{em} = 3.475$, $z_{abs} = 3.327$, $\log N(HI) = 21.0 \pm 0.10$

Many ions are detected in this absorber, such as SiII λ 1808, SII $\lambda\lambda\lambda$ 1259 1253 1250, AlIII $\lambda\lambda$ 1854 1862, NiII $\lambda\lambda$ 1370 1317, CIV $\lambda\lambda$ 1548 1550 and SiIV $\lambda\lambda$ 1393 and 1402. The low- and intermediate-ionization ions show a similar profile (strong absorption line near v = 65 km/s) and are therefore fitted together with a 7-component profile. Only the non-saturated lines, NiII $\lambda\lambda$ 1370 1317, SiII λ 1808 and SII λ 1253 are used in the derivation of the parameter. The ions AlII λ 1670, CII $\lambda\lambda$ 1036 and 1334 are also detected but not fitted due to strong saturation. AlIII have not been fitted due to a blend in the AlIII λ 1862 line. The resulting abundances for the low-ionization ions are log N(SiII)=15.93 $\pm$ 0.01, log N(SII)=15.31 $\pm$ 0.01 and log N(NiII)=13.74 $\pm$ 0.01. A non-detection from MgI λ 1827 gives the following upper limit: log N(MgI) $<$ 13.33.

The high-ionization ions CIV $\lambda\lambda$ 1548 1550 and SiIV $\lambda\lambda$ 1402 are fitted using a 3-component profile, extending to about 200 km/s. SiIV λ 1393 is not considered for the fit as it is blended blueward the bluest component of the fit (v $\sim$ 150 km/s). This gives the following abundances for the high-ionization transitions: log N(CIV)=13.71$\pm$0.01 and log N(SiIV)=13.56 $\pm$ 0.01. We note that, although the reddest components for both low- and high-ionization profiles have velocities that differ by about 20 km/s, they both stand out from the bluer absorption profile.

The parameter fits of the individual components are listed in Table C12 and the corresponding Voigt profile fits are shown in Fig. C12.

Table C12. Voigt profile fit parameters to the low- and high-ionization species for the z_{abs}=3.327 log N(H I)=21.0 $\pm$ 0.10 absorber towards QSO J115538.6+053050.

Comp.	z_{abs}	b km s^{-1}	Ion	log N cm^{-2}
1	3.32555	5.9 $\pm$ 0.1	NiII	12.84 $\pm$ 0.01
			SII	14.14 $\pm$ 0.01
			SiII	–
			AlIII	–
2	3.32575	33.8 $\pm$ 0.1	NiII	13.35 $\pm$ 0.01
			SII	14.66 $\pm$ 0.01
			SiII	15.72 $\pm$ 0.01
			AlIII	12.77 $\pm$ 0.01
3	3.32606	13.6 $\pm$ 0.1	NiII	12.88 $\pm$ 0.01
			SII	14.83 $\pm$ 0.01
			SiII	15.20 $\pm$ 0.01
			AlIII	11.96 $\pm$ 0.01
4	3.32626	2.0 $\pm$ 0.1	NiII	12.27 $\pm$ 0.02
			SII	14.16 $\pm$ 0.02
			SiII	13.96 $\pm$ 0.03
			AlIII	11.55 $\pm$ 0.04
5	3.32663	10.7 $\pm$ 0.2	NiII	12.48 $\pm$ 0.01
			SII	14.27 $\pm$ 0.01
			SiII	14.55 $\pm$ 0.01
			AlIII	11.94 $\pm$ 0.02
6	3.32700	11.6 $\pm$ 0.1	NiII	12.71 $\pm$ 0.01
			SII	14.25 $\pm$ 0.01
			SiII	14.57 $\pm$ 0.01
			AlIII	12.12 $\pm$ 0.01
7	3.32797	13.2 $\pm$ 0.1	NiII	12.93 $\pm$ 0.01
			SII	14.45 $\pm$ 0.01
			SiII	14.89 $\pm$ 0.01
			AlIII	12.60 $\pm$ 0.01
1	3.32500	10	CIV	12.9 $\pm$ 0.02
			SiIV	13.00 $\pm$ 0.01
2	3.32558	20	CIV	13.48 $\pm$ 0.02
			SiIV	13.40 $\pm$ 0.01
3	3.32755	7	CIV	13.10 $\pm$ 0.01
			SiIV	12.00 $\pm$ 0.02

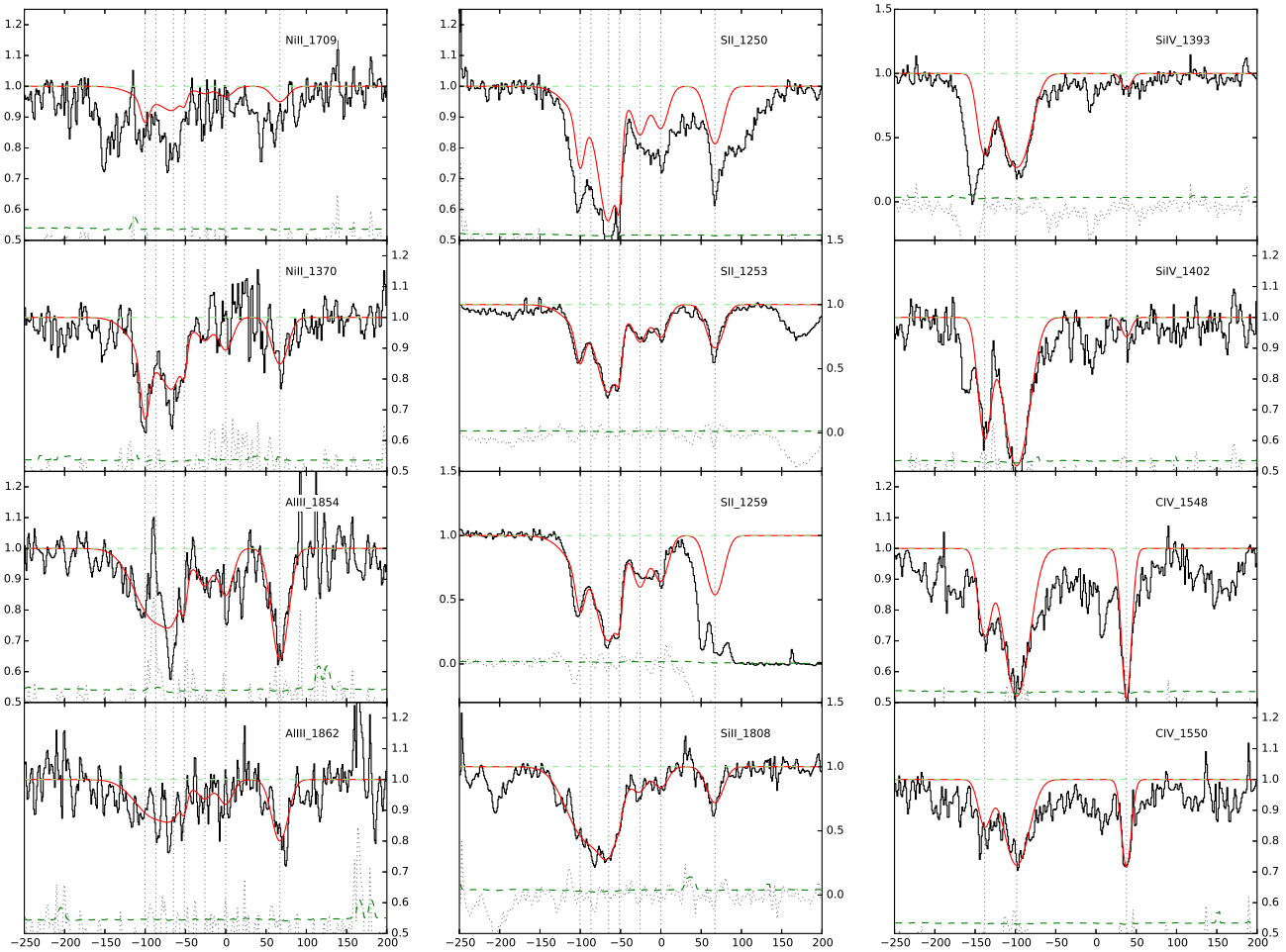

Figure C12. QSOJ115538.6+053050 z=3.32

Table C13. Voigt profile fit parameters to the low–ionization species for the z_{abs}=1.72 log N(H I)=19.48 ± 0.13 absorber towards QSO LBQS 1232+0815.

Comp.	z_{abs}	b km s^{-1}	Ion	log N cm^{-2}
1	1.71942	7.7 ± 0.1	FeII	13.17 ± 0.01
			AlIII	12.61 ± 0.01
			SiII	14.10 ± 0.01
2	1.71958	4.6 ± 0.4	FeII	12.15 ± 0.02
			AlIII	11.96 ± 0.02
			SiII	13.20 ± 0.02
3	1.71995	8.2 ± 0.6	FeII	12.07 ± 0.03
			AlIII	12.04 ± 0.02
			SiII	13.06 ± 0.02
4	1.72014	8.8 ± 0.1	FeII	13.02 ± 0.01
			AlIII	12.90
			SiII	14.01 ± 0.01
5	1.72036	7.1 ± 0.3	FeII	12.16 ± 0.02
			AlIII	12.37 ± 0.01
			SiII	–
6	1.72094	18.3 ± 0.6	FeII	12.33 ± 0.02
			AlIII	12.41 ± 0.01
			SiII	–
1	1.71946	23.3 ± 0.3	SiIV	13.47 ± 0.01
2	1.72008	14.5 ± 0.5	SiIV	> 14.50
3	1.72032	14.2 ± 0.5	SiIV	> 13.82
4	1.72089	10.5 ± 0.3	SiIV	13.49 ± 0.01
5	1.72104	27.8 ± 0.6	SiIV	13.41 ± 0.01

C13 QSO LBQS 1232+0815 $z_{em} = 2.57$, $z_{abs} = 1.72$, $\log N(HI) = 19.48 \pm 0.13$

The EUADP spectrum for this DLA absorber covers the following low- and intermediate-ionization transitions: FeII $\lambda\lambda\lambda\lambda$ 2382, 2374, 2344, 1608, AlIII $\lambda\lambda$ 1862, 1854, SiII $\lambda\lambda$ 1526 (blended) and 1808. It also covers CII λ 1334, which is saturated. The low- and intermediate-ionization profiles are well fitted together with the transitions FeII $\lambda\lambda$ 2382, 2344, AlIII $\lambda\lambda$ 1854, 1862 and SiII λ 1808 using 6 components spread over $\sim$ 200 km/s, resulting in the following abundances log N(FeII)=13.50 ± 0.01, log N(SiII) = 14.41 ± 0.01 and log N(AlIII)=13.28±0.01. We derived upper limits from non detection for SII λ 1253, log N(SII) < 14.18, CrII λ 2056, log N(CrII) < 12.38, MgI λ 2026, log N(MgI) < 12.21, NiII λ 1751, log N(NiII) < 13.05, and ZnII λ 2026, log N(ZnII) < 11.58.

The high-ionization ions detected in the spectrum are SiIV $\lambda\lambda$ 1393, 1402, CIV $\lambda\lambda$ 1548 and 1550. The CIV transition lines are highly saturated and contaminated by an apparent blend, they are therefore not consider for the fit. From the less saturated SiIV transition lines, a 5-component profile provides the following lower limit log N(SiIV) > 14.67. We notice that the low- and high-ionization ions seem to share the same components.

The parameter fits of the individual components are listed in Table C13 and the corresponding Voigt profile fits are shown in Fig. C13.

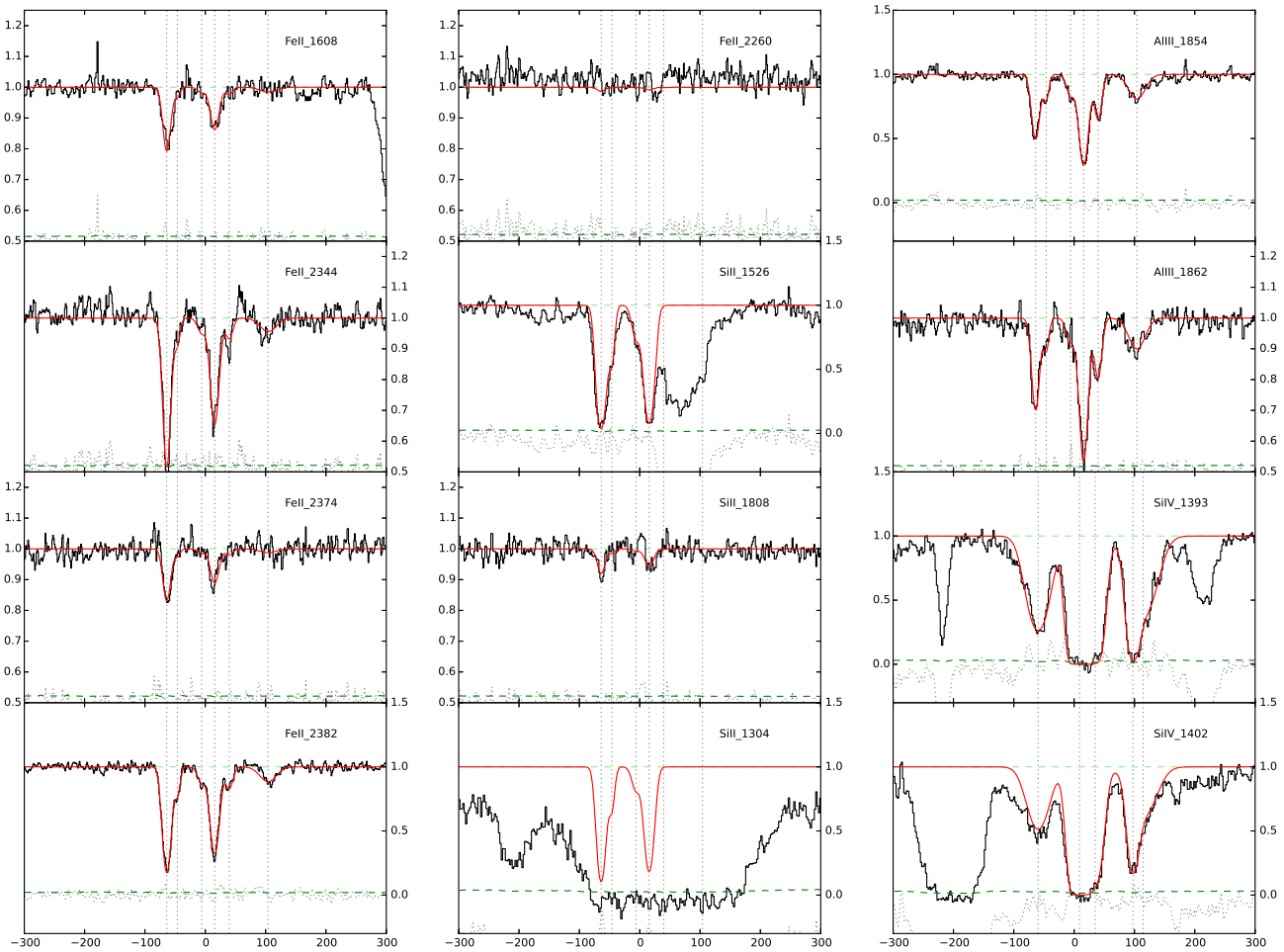

Figure C13. QSOLBQS1232+0815

Table C14. Voigt profile fit parameters to the low- and intermediate-ionization species for the z_{abs}=2.654 log N(H I)=19.56 ± 0.13 absorber towards QSO J1330-2522.

Comp.	z_{abs}	b km s^{-1}	Ion	log N cm^{-2}
1	2.65414	6.7	AlII	12.16 ± 0.02
			AlIII	12.55 ± 0.02
2	2.65433	2.0	AlII	10.90 ± 0.21
			AlIII	11.79 ± 0.08

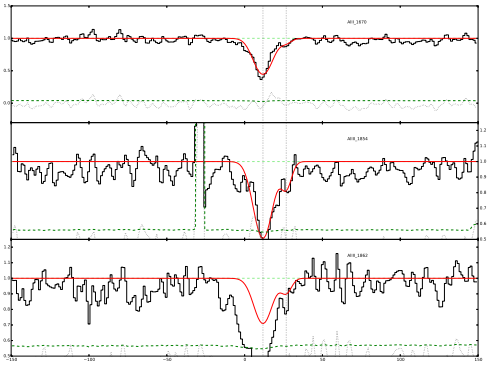

Figure C14. QSOJ1330-2522 z=2.654

C14 QSO J1330-2522 z_{em} = 3.91, z_{abs} = 2.654, log N(HI) = 19.56 ± 0.13

This EUADP spectrum covers six ions, SiIV λλ 1393, 14(SiII λ 1526, AlII λ 1670, AlIII λλ 1854 and 1862. Many these transitions are blended and/or saturated, such tl only AlII λ 1670 and AlIII λ 1854 have been fitted. T asymmetry of both lines suggests a 2-component profile, sulting in the following abundances: log N(AlIII)=12.62 0.02 and log N(AlII)=12.18 ± 0.2. We derive an upper lir from non detection of NiII λ 1741: log N(NiII) < 13.22.

In this spectrum, the high-ionization ions SiIV λλ 13! 1402 and CIV λλ 1548 and 1550 are covered but suffer fr severe blending, such that no fit has been performed.

The parameter fits of the individual components a listed in Table C14 and the corresponding Voigt profile fits are shown in Fig. C14.

C15 QSO J1356-1101 z_{em} = 3.006, z_{abs} = 2.397, log N(HI) = 19.85 ± 0.08

The spectrum covers four FeII lines and two SiIV lines associated with the absorber: FeII λλλλ 2600 2344 2382 2586 and SiIV λλ 1393 and 1402. The low-ionization profile is well fitted with a 6-component profile in the red, and a single blue component isolated from the red group of components by about 250km/s. The resulting column density is log N(FeII) = 13.44 ± 0.01. We derived upper limits from the non-detection of several transitions: CrII λ 2056, log N(CrII) < 12.64, MnII λ 2576, log N(MnII) < 12.07, NiII λ 1317, log N(NiII) < 12.76, and ZnII λ 2062, log N(ZnII) < 12.38.

Table C15. Voigt profile fit parameters to the low-ionization species for the z_{abs}=2.397 log N(H I)=19.85 ± 0.08 absorber towards QSO J1356-1101.

Comp.	z_{abs}	b km s^{-1}	Ion	log N cm^{-2}
1	2.39339	11.0 ± 0.3	FeII	12.81 ± 0.01
2	2.39621	14.8 ± 1.4	FeII	11.99 ± 0.08
3	2.39629	4.5 ± 0.3	FeII	12.44 ± 0.02
4	2.39669	61.1 ± 5.4	FeII	12.63 ± 0.04
5	2.39677	5.8 ± 0.1	FeII	12.95 ± 0.01
6	2.39706	2.4 ± 0.3	FeII	12.44 ± 0.02
7	2.39714	2.6 ± 0.6	FeII	12.10 ± 0.02

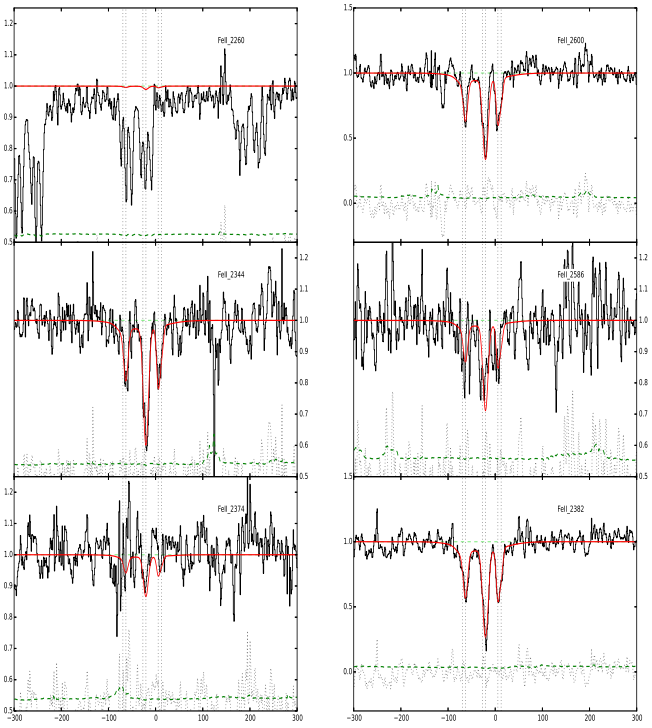

Figure C15. QSOJ1356-1101

The high-ionization ion SiIV λλ 1393 and 1402 is detected but not fitted because it is heavily saturated.

The parameter fits of the individual components are listed in Table C15 and the corresponding Voigt profile fits are shown in Fig. C15.

C16 QSO J1621-0042 z_{em} = 3.7, z_{abs} = 3.104, log N(HI) = 19.7 ± 0.20

The EUADP spectrum probing this high-redshift subDLA covers many transitions associated with the absorber such as FeII λλ 1608, 1611, CII λλ 1036, 1334, SII λλλ 1250, 1253, 1259, SiII λλλλλ 1190, 1193, 1260, 1304, 1526, SiIV

$\lambda\lambda$ 1393, 1402 (partly), CIV $\lambda\lambda$ 1548 and 1550. Most of these lines are heavily blended (SiII $\lambda\lambda\lambda$ 1190, 1304, 1260) or saturated (CII $\lambda\lambda$ 1334 and 1036), but the wide coverage and SNR of the spectrum provide enough elements to derive the different parameters.

The low-ionization ions are fitted with a 12-component profile, with a broad velocity range (about 400 km/s). The component with the highest velocity (v $\sim$ 400 km/s) is identified in three transitions: SiII $\lambda\lambda$ 1190 and CII λ 1334. The low velocity components are less affected by the blending and are therefore well fitted, but the information about the group of component between v $\sim$ 100 km/s and v $\sim$ 250 km/s are only derived from FeII λ 1608 and SiII λ 1526. For CII in particular, this group of component is saturated so that a lower limit is derived based on the low velocity components $\log$ N(CII) $<$ 14.41. The SII line is most probably blended as its profile does not match the other low-ionization ions. The resulting abundances for the low-ionization ions are $\log$ N(FeII) = 13.30$\pm$0.04 and $\log$ N(SiII) = 13.78$\pm$0.03.

The high-ionization ion components are also detected with a broad velocity range (400km/s). The EUADP spectrum does not fully cover the SiIV λ 1402 transition, thus preventing a proper fit. However, the blue part of SiIV λ 1402 matches the blue parts of SiIV λ 1393 and the CIV lines, confirming the detection of SiIV and CIV. It is interesting to note that in this case no satisfactory solutions could be found to fit simultaneously the SiIV and CIV doublets. To check the wavelength calibration of the spectrum, the SiII $\lambda\lambda$ 1526 and 1190 lines (which fall on two different arm of the spectrograph) are fitted independently. The redshifts determined for these transitions are consistent with each other (z = 3.10408 and z = 3.10409) thus indicating no systematic shift in the spectrum. Therefore, the SiIV and CIV transitions are fitted separately, with different Doppler parameters and velocities as seen in Table C16. The 14-component fit results in $\log$ N(SiIV) = 14.24 $\pm$ 0.03 and $\log$ N(CIV) = 14.71 $\pm$ 0.01.

The parameter fits of the individual components are listed in Table C16 and the corresponding Voigt profile fits are shown in Fig. C16.

C17 QSO 4C12.59 z_{em} = 1.792, z_{abs} = 0.531, $\log$ N(HI) = 20.7 $\pm$ 0.09

This very low-redshift DLA absorber presents a few absorption features in the EUADP spectrum partly due the limited wavelength coverage and an overall low SNR. The FeII ion is detected in the following transitions FeII $\lambda\lambda\lambda$ 2344, 2382 and 2374. The FeII λ 2382 line is saturated. A satisfactory fit for the remaining transitions FeII $\lambda\lambda$ 2374 and 2344 is found with six components. The resulting column density is $\log$ N(FeII) = 14.26 $\pm$ 0.08. The CII λ 2325 line is covered but not detected. The resulting upper limit is $\log$ N(CII) $<$ 11.36.

No high-ionization ions are covered in this EUADP spectrum.

The parameter fits of the individual components are listed in Table C17 and the corresponding Voigt profile fits are shown in Fig. C17.

Table C17. Voigt profile fit parameters to the low-ionization species for the z_{abs}=0.531 log N(H I)=20.7 $\pm$ 0.09 absorber towards QSO 4C 12.59.

Comp.	z_{abs}	b km s^{-1}	Ion	log N cm^{-2}
1	0.53123	7.0 $\pm$ 1.3	FeII	13.20 $\pm$ 0.08
2	0.53130	4.6 $\pm$ 1.4	FeII	13.58 $\pm$ 0.08
3	0.53135	4.0 $\pm$ 1.1	FeII	13.68 $\pm$ 0.10
4	0.53143	13.9 $\pm$ 4.1	FeII	13.59 $\pm$ 0.26
5	0.53143	6.8 $\pm$ 1.4	FeII	13.47 $\pm$ 0.28
6	0.53156	6.3 $\pm$ 1.8	FeII	13.06 $\pm$ 0.12

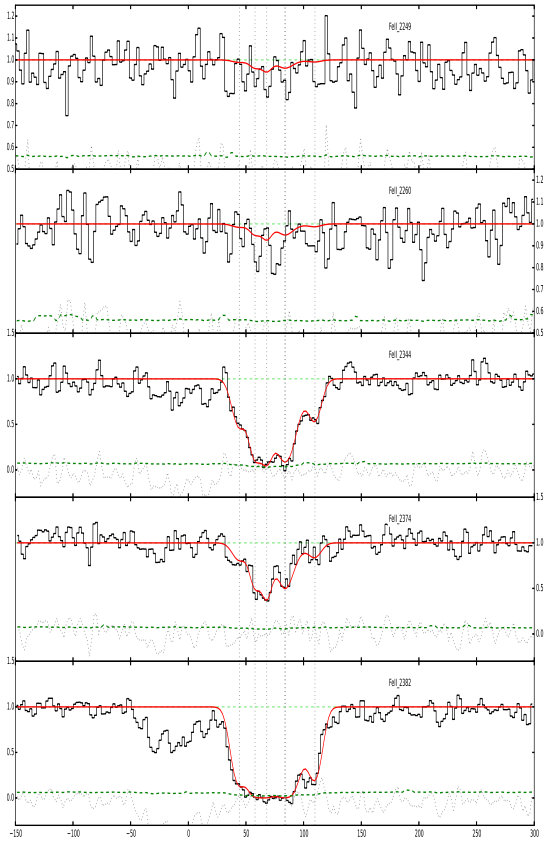

Figure C17. QSO4C12.59

C18 QSO LBQS2114-4347 z_{em} = 2.04, z_{abs} = 1.912, $\log$ N(HI) = 19.5 $\pm$ 0.10

The EUADP spectrum of this quasar covers the following low-ionization ions: SiII $\lambda\lambda$ 1304 1526, MgII $\lambda\lambda$ 2796 2803, FeII $\lambda\lambda\lambda\lambda\lambda\lambda$ 2600 1608 2260 2344 2374 2586, AlII λ 1670 and CII λ 1334. An 11-component fit is used to describe the lines free from saturations and blends, namely SiII $\lambda\lambda$ 1526 1304 and FeII $\lambda\lambda\lambda$ 1608 2374 and 2586.

Table C16. Voigt profile fit parameters to the low- and high-ionization species for the z_{abs}=3.104 log N(H I)=19.7 ± 0.20 absorber towards QSO J1621-0042.

Comp.	z_{abs}	b km s^{-1}	Ion	log N cm^{-2}	Comp.	z_{abs}	b km s^{-1}	Ion	log N cm^{-2}
1	3.10394	3.7 ± 0.7	FeII	12.62 ± 0.06	1	3.10509	7.0 ± 1.0	SiIV	12.77 ± 0.07
			SiII	12.95 ± 0.03		3.10541	24.6 ± 1.0	CIV	13.49 ± 0.21
			CII	13.90 ± 0.03	2	3.10530	7.9 ± 3	SiIV	12.69 ± 0.18
2	3.10407	2.7 ± 0.5	FeII	13.03 ± 0.04		3.10539	6.4 ± 3.4	CIV	12.13 ± 0.21
			SiII	13.55 ± 0.03	3	3.10564	12.0 ± 2.8	SiIV	13.47 ± 0.09
			CII	14.00 ± 0.17		3.10568	8.5 ± 1.0	CIV	13.16 ± 0.05
3	3.10415	8.4 ± 2	FeII	12.32 ± 0.19	4	3.10588	6.1 ± 1.9	SiIV	13.40 ± 0.12
			SiII	12.93 ± 0.15		3.10592	9.0 ± 0.6	CIV	13.64 ± 0.04
			CII	13.57 ± 0.02	5	3.10607	7.5 ± 1.7	SiIV	13.52 ± 0.09
4	3.10438	6.0 ± 1.1	FeII	12.28 ± 0.11		3.10612	7.9 ± 0.6	CIV	13.69 ± 0.05
			SiII	12.73 ± 0.06	6	3.10631	8.1 ± 1.5	SiIV	13.16 ± 0.10
			CII	13.47 ± 0.01		3.10632	8.6 ± 0.5	CIV	13.36 ± 0.05
5	3.10462	7.3 ± 1.4	FeII	11.95 ± 0.21	7	3.10657	15.0 ± 1.6	SiIV	13.10 ± 0.06
			SiII	12.37 ± 0.06		3.10659	21.5 ± 0.7	CIV	13.70 ± 0.02
			CII	13.00 ± 0.01	8	3.10709	9.3 ± 1.2	SiIV	12.51 ± 0.04
6	3.10523	6.1 ± 0.13	FeII	13.28 ± 0.01		3.10712	12.1 ± 0.4	CIV	13.24 ± 0.02
			SiII	13.74 ± 0.01	9	3.10742	7.9 ± 1.1	SiIV	12.40 ± 0.04
			CII	–		3.10746	9.3 ± 0.4	CIV	12.95 ± 0.02
7	3.10563	7.9 ± 0.23	FeII	13.16 ± 0.02	10	3.10780	6.0 ± 0.6	SiIV	12.50 ± 0.02
			SiII	13.73 ± 0.03		3.10785	12.2 ± 0.2	CIV	13.27 ± 0.01
			CII	–	11	3.10836	6.5 ± 0.7	SiIV	12.61 ± 0.03
8	3.10593	20.0 ± 1.08	FeII	13.07 ± 0.05		3.10842	10.4 ± 0.2	CIV	13.63 ± 0.01
			SiII	13.73 ± 0.03	12	3.10859	5.7 ± 1.2	SiIV	12.49 ± 0.07
			CII	–		3.10865	5.5 ± 0.3	CIV	13.43 ± 0.02
9	3.10601	5.0	FeII	13.10 ± 0.02	13	3.10883	10.6 ± 2.1	SiIV	12.53 ± 0.07
			SiII	13.66 ± 0.02		3.10887	10.4 ± 0.3	CIV	13.76 ± 0.01
			CII	–	14	3.10922	7.5 ± 0.3	SiIV	13.47 ± 0.03
10	3.10618	0.9 ± 0.2	FeII	–		3.10928	14.1 ± 0.1	CIV	14.12 ± 0.01
			SiII	13.39 ± 0.25					
			CII	–					
11	3.10743	6.1 ± 0.29	FeII	12.47 ± 0.06					
			SiII	12.93 ± 0.01					
			CII	–					
12	3.10926	2.5 ± 0.25	FeII	10.84 ± 1.99					
			SiII	12.77 ± 0.01					
			CII	–					

This results in the following column densities: $\log$N(SiII) = 14.39 ± 0.02, $\log$N(FeII) = 14.02 ± 0.01, $\log$N(AlII) = 13.00 ± 0.01 and $\log$N(MgII) = 14.40 ± 0.01. In addition, the non-detections in the spectrum provide further upper limits as follows: AlIII λ 1854, $\log$N(AlIII) < 12.09, CrII λ 2056, $\log$N(CrII) < 12.77, MnII λ 2576, $\log$N(MnII) < 12.24, NiII λ 1317, $\log$N(NiII) < 12.88, SII λ 1253, $\log$N(SII) < 13.97, and ZnII λ 2026, $\log$N(ZnII) < 12.17.

A 4-component profile is used to fit the high-ionization ions: CIV $\lambda\lambda$ 1548 1550 and SiIV $\lambda\lambda$ 1393 and 1402. The resulting column densities are $\log$N(SiIV) = 13.43 ± 0.01 and $\log$N(CIV) = 14.39 ± 0.01.

The parameter fits of the individual components are listed in Table C18 and the corresponding Voigt profile fits are shown in Fig. C18.

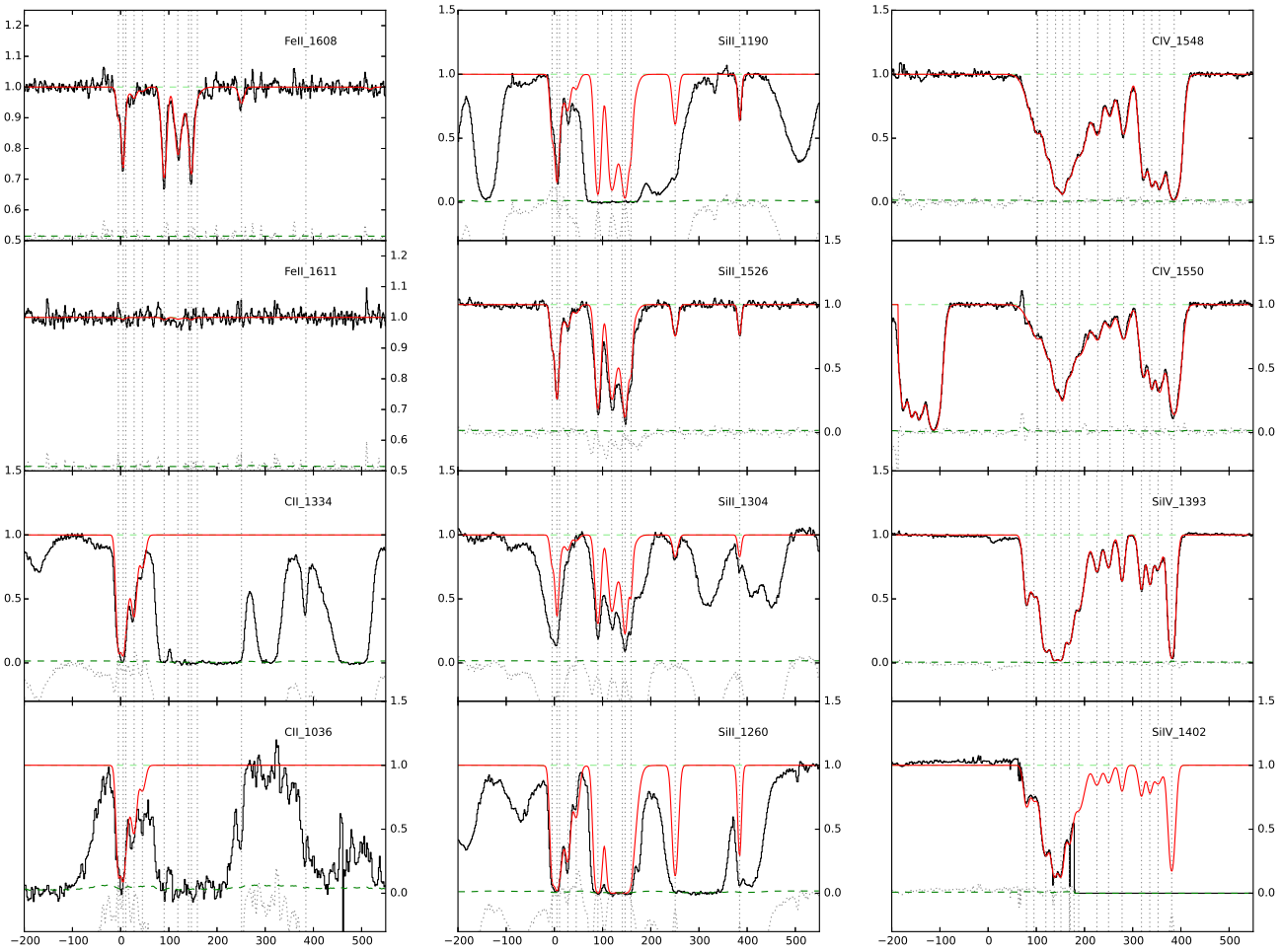

Figure C16. QSOJ1621-0042

Table C18. Voigt profile fit parameters to the low- and high-ionization species for the z_{abs}=1.912 log N(H I)=19.5 ± 0.10 absorber towards QSO LBQS 2114-4347.

Comp.	z_{abs}	b km s^{-1}	Ion	log N cm^{-2}
1	1.9109296	6.7 ± 0.1	SiII	13.16 ± 0.03
			FeII	12.65 ± 0.01
			AlII	11.70 ± 0.02
			MgII	12.92 ± 0.01
2	1.9111506	3.0 ± 0.1	SiII	12.53 ± 0.01
			FeII	12.11 ± 0.01
			AlII	10.84 ± 0.01
			MgII	11.76 ± 0.01
3	1.9113052	4.6 ± 0.1	SiII	13.44 ± 0.01
			FeII	13.18 ± 0.01
			AlII	12.10 ± 0.01
			MgII	13.23 ± 0.01
4	1.91146	12.3 ± 0.1	SiII	12.96 ± 0.01
			FeII	–
			AlII	11.66 ± 0.01
			MgII	12.53 ± 0.01
5	1.91148	3.7 ± 0.1	SiII	12.79 ± 0.04
			FeII	12.38 ± 0.01
			AlII	11.75 ± 0.01
			MgII	12.69 ± 0.01
6	1.91165	5.5 ± 0.1	SiII	13.00 ± 0.03
			FeII	12.30 ± 0.01
			AlII	11.43 ± 0.02
			MgII	12.55 ± 0.01
7	1.91185	4.1 ± 0.1	SiII	14.08 ± 0.02
			FeII	13.77 ± 0.01
			AlII	12.69 ± 0.01
			MgII	14.21 ± 0.01
8	1.91205	6.7 ± 0.1	SiII	13.37 ± 0.20
			FeII	12.88 ± 0.01
			AlII	11.73 ± 0.01
			MgII	13.12 ± 0.01
9	1.91221	4.0 ± 1.0	SiII	13.17 ± 0.02
			FeII	12.59 ± 0.01
			AlII	11.81 ± 0.01
			MgII	13.14 ± 0.01
10	1.91232	0.9 ± 0.1	SiII	12.25 ± 0.01
			FeII	12.41 ± 0.01
			AlII	10.91 ± 0.01
			MgII	13.08 ± 0.01
11	1.91252	6.3 ± 1.0	SiII	13.24 ± 0.02
			FeII	12.78 ± 0.01
			AlII	11.84 ± 0.01
			MgII	13.05 ± 0.01
1	1.91173	16.3 ± 0.3	CIV	14.19 ± 0.01
			SiIV	12.97 ± 0.01
2	1.91199	8.5 ± 0.3	CIV	13.63 ± 0.02
			SiIV	12.65 ± 0.02
3	1.91224	12.3 ± 0.8	CIV	13.18 ± 0.03
			SiIV	12.63 ± 0.02
4	1.91252	8.8 ± 0.2	CIV	13.49 ± 0.01
			SiIV	12.97 ± 0.01

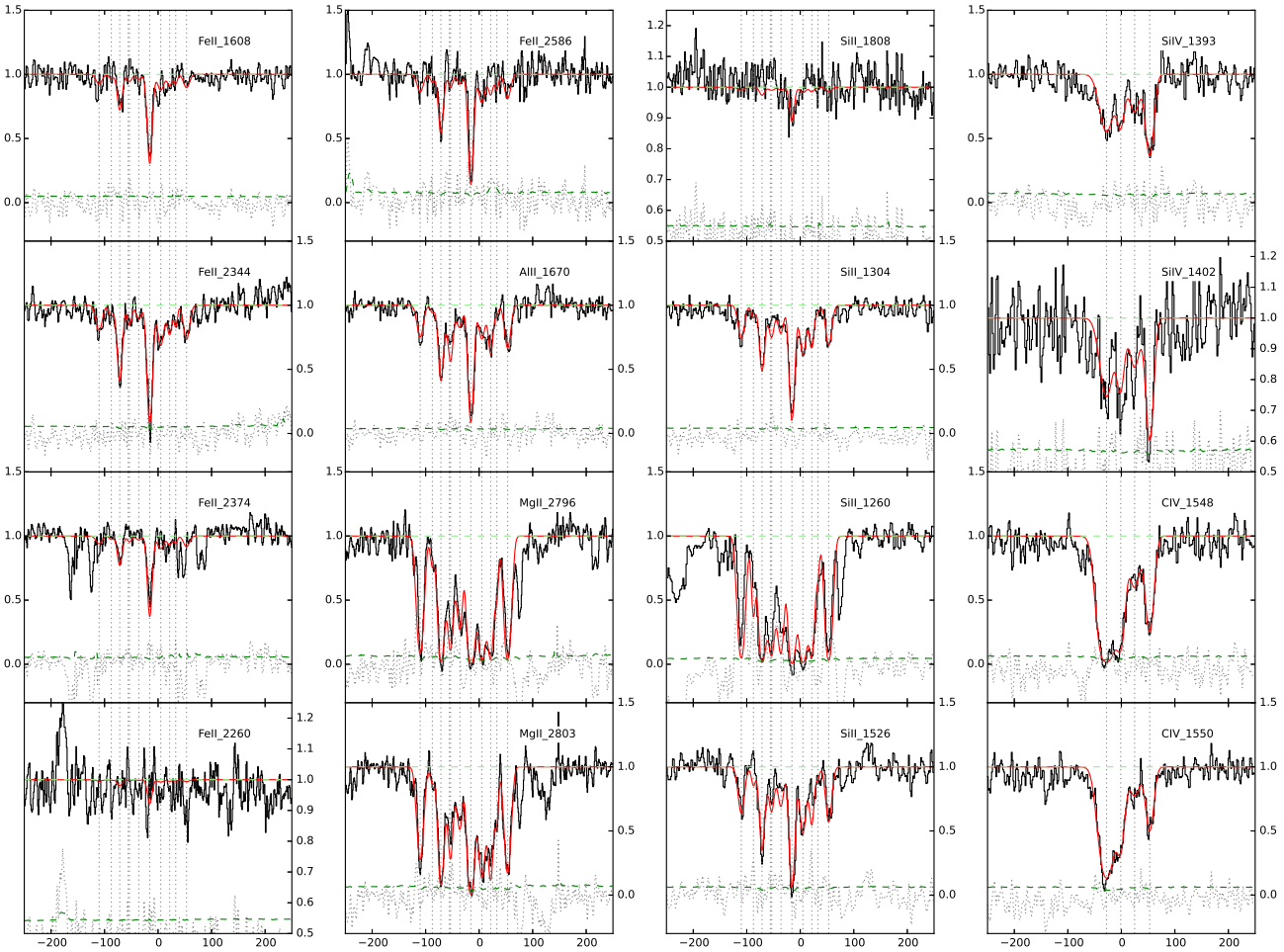

Figure C18. QSOLBQS2114-4347

Table C19. Voigt profile fit parameters to the low- and intermediate-ionization species for the z_{abs}=2.638 log N(H I)=19.25 ± 0.15 absorber towards QSO B2126-15.

Comp.	z_{abs}	b km s^{-1}	Ion	log N cm^{-2}
1	2.63767	17.8 ± 0.1	FeII	13.77 ± 0.01
			SiII	14.38 ± 0.02
			NiII	12.66 ± 0.02
2	2.63799	4.1 ± 0.1	FeII	13.39 ± 0.01
			SiII	13.80 ± 0.05
			NiII	12.47 ± 0.01
3	2.63807	19.3 ± 0.3	FeII	13.45 ± 0.01
			SiII	14.21 ± 0.03
			NiII	12.83 ± 0.02
1	2.63758	9.9 ± 0.5	AlIII	12.38 ± 0.02
2	2.63784	13.3 ± 0.2	AlIII	12.84 ± 0.01
3	2.63802	4.2 ± 0.5	AlIII	12.34 ± 0.05
4	2.63818	10.3 ± 0.8	AlIII	12.52 ± 0.08
5	2.63827	11.75 ± 1.8	AlIII	12.43 ± 0.11

C19 QSO B2126-15 z_{em} = 3.268, z_{abs} = 2.638, log N(HI) = 19.25 ± 0.15

This EUADP spectrum covers the following transitions associated with the absorber: NiII λλλ 1709 1741 1751, SiII λ 1808, FeII λλλλλ 2586 1608 2249 2600 2382 and AlIII λλI 1854 and 1862. The good quality of the spectrum and the presence of non blended lines enables a robust 3-component fit of the low-ionization ions with FeII λλ 1608 2586, SiII λ 1808 and NiII λλλ 1741 1751 and 1709. The apparent shift in FeII λ 2586 is thought to originate from a poor continuum fit. The resulting abundances are log N(FeII) = 14.05 ± 0.01, log N(SiII) = 14.67 ± 0.02, log N(NiII) = 13.15 ± 0.01. We derive an upper limit from the non detection of ZnII λ 2026: log N(ZnII) < 11.58.

The intermediate-ionization transitions AlIII λλ 1854 and 1862 do not share the same absorption profile as the low-ionization ions (except for the strong narrow line in the middle of both profiles). These are therefore fitted separately with a 5-component profile. The resulting column density is log N(AlIII) = 13.24 ± 0.02.

The high-ionization transitions SiIV λλ 1398 and 1402 are clearly detected. However these lines are both blended and saturated, so that no fit are attempted.

The parameter fits of the individual components are listed in Table C19 and the corresponding Voigt profile fits are shown in Fig. C19.

C20 QSO B2126-15 z_{em} = 3.268, z_{abs} = 2.769, log N(HI) = 19.2 ± 0.15

Many lines associated to the absorber are detected in this EUADP spectrum: FeII λλλλλλλ 2586 2374 2344 1608 1144 2382 2600, SiII λλλ 1808 1526 1190, CII λλ 1334 1036, AlII λ 1670, AlIII λλ 1862 1854, CIV λλ 1550 1548 and SiIV λλ 1402 and 1393.

The low-ionization ions are fitted considering the non blended lines, FeII λ 2344, SiII λλ 1808, 1526 and AlII λ 1670. This resulted in a 9-component profile with a 250km/s velocity range. The transition FeII λ 2374 is not considered for the final fit due to the complexity in the continuum placement in this portion of the spectrum. The CII line is strongly saturated and therefore no fit could be performed on this transition. The AlII λ 1670 transition is saturated, therefore resulting in a lower limit for the column density (log N(AlII) < 14.05). The fit results in the following column densities: log N(FeII) = 14.17 ± 0.01 and log N(SiII) = 14.79 ± 0.01. In addition, the non-detections led to the following upper limits: CrII λ 2056, log N(CrII) < 12.40, MnII λ 2606, log N(MnII) < 12.28, and ZnII λ 2062, log N(ZnII) < 11.95.

The intermediate- and high-ionization ions AlIII λλ 1854 1862 and SiIV λ 1402 are fitted together given the similarities in their absorption profile. The SiIV λ 1393 transition is not considered because of an unidentified blending in the red part of the profile. The blending does not match any transition from the absorber at redshift z_{abs} = 2.638. The 9-component profile of about 200km/s and results in the following column densities log N(SiIV) = 13.84 ± 0.13 and log N(AlIII) = 13.11 ± 0.01. The CIV doublet is also covered by the data but the CIV λ 1548 line is saturated and both profiles show evidence for the presence of blending. It is interesting to note that the CIV doublet presents some components far in the red (up to ∼ 240km/s) which are not seen in SiIV. The OVI λλ 1031 and 1037 lines are also detected, but they are blended as often the case in the Lyα forest.

The parameter fits of the individual components are listed in Table C20 and the corresponding Voigt profile fits are shown in Fig. C20.

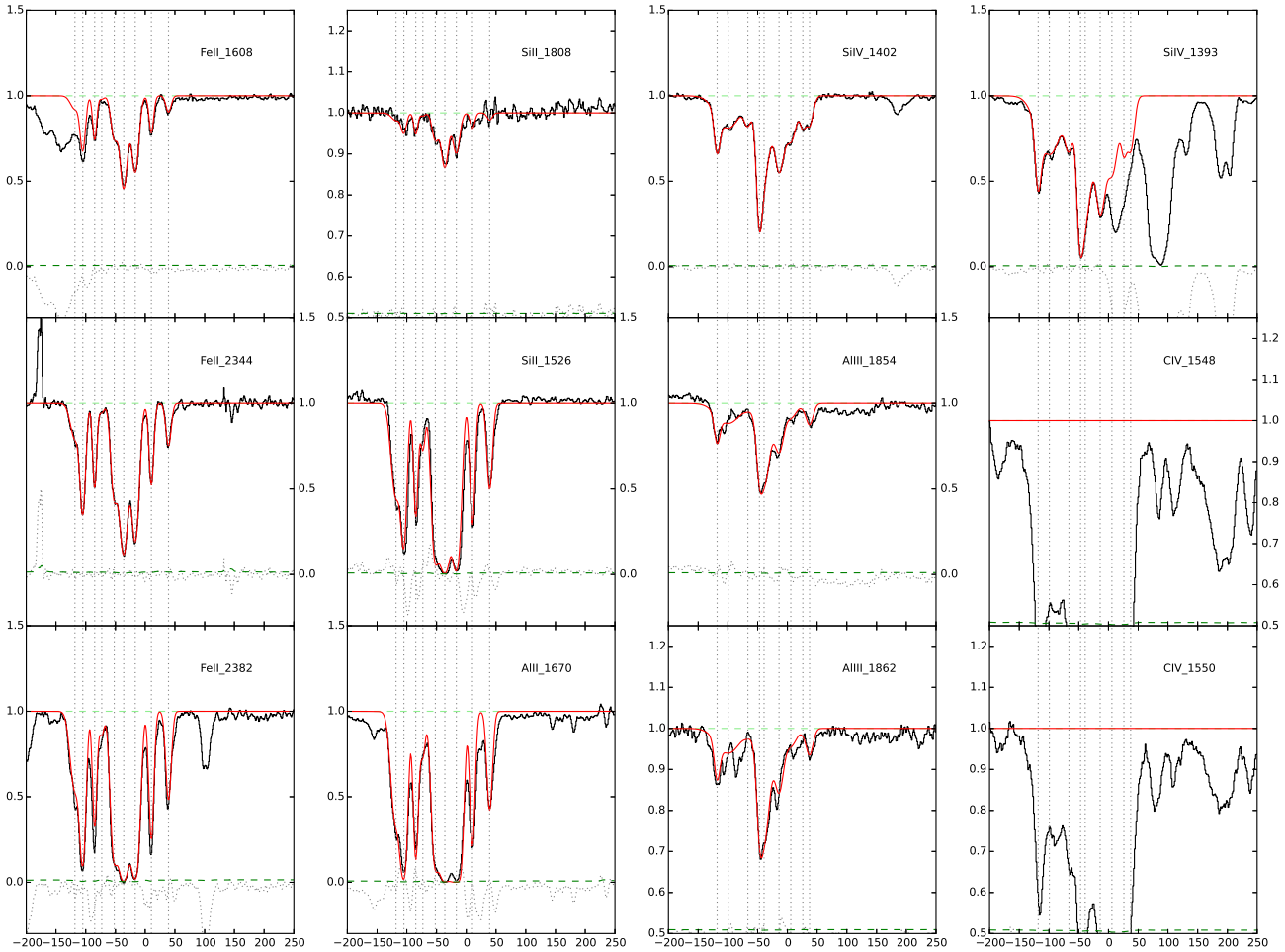

Figure C19. QSOB2126-15 $z_{abs} = 2.638$

Table C20. Voigt profile fit parameters to the low- and high- and intermediate-ionization species for the z_{abs}=2.769 log N(H I)=19.20 ± 0.15 absorber towards QSO B2126-15.

Comp.	z_{abs}	b km s^{-1}	Ion	log N cm^{-2}
1	2.76751	9.4 ± 0.8	FeII	12.78 ± 0.01
			SiII	13.52 ± 0.01
			AlII	12.40 ± 0.01
2	2.76768	4.4 ± 0.1	FeII	13.23 ± 0.01
			SiII	13.70 ± 0.01
			AlII	13.07 ± 0.01
3	2.76793	2.1 ± 0.2	FeII	13.06 ± 0.01
			SiII	13.64 ± 0.07
			AlII	13.42 ± 0.01
4	2.76808	3.7 ± 1.4	FeII	11.91 ± 0.05
			SiII	12.87 ± 0.01
			AlII	11.58 ± 0.01
5	2.76835	6.2 ± 0.2	FeII	13.19 ± 0.01
			SiII	13.94 ± 0.05
			AlII	12.65 ± 0.01
6	2.76855	7 ± 0.2	FeII	13.67 ± 0.01
			SiII	14.30 ± 0.02
			AlII	13.13 ± 0.01
7	2.76879	6.8 ± 0.1	FeII	13.54 ± 0.01
			SiII	14.15 ± 0.03
			AlII	13.70 ± 0.01
8	2.76913	3.2 ± 0.2	FeII	12.99 ± 0.01
			SiII	13.55 ± 0.09
			AlII	12.45 ± 0.01
9	2.76949	4.4 ± 0.3	FeII	12.65 ± 0.01
			SiII	13.26 ± 0.01
			AlII	12.10 ± 0.01
1	2.76751	4.9 ± 0.9	SiIV	12.55 ± 0.06
			AlIII	11.91 ± 0.02
2	2.76775	26.3 ± 2.5	SiIV	13.02 ± 0.04
			AlIII	12.33 ± 0.01
3	2.76816	7.3 ± 6.9	SiIV	12.37 ± 0.47
			AlIII	11.02 ± 0.11
4	2.76841	4.6 ± 2.9	SiIV	13.17 ± 0.38
			AlIII	12.01 ± 0.02
5	2.76851	12.0 ± 6.2	SiIV	13.18 ± 0.46
			AlIII	12.72 ± 0.01
6	2.76882	9.1 ± 1.7	SiIV	13.02 ± 0.10
			AlIII	12.32 ± 0.01
7	2.76907	12.4 ± 4.3	SiIV	12.88 ± 0.15
			AlIII	11.87 ± 0.02
8	2.76933	4.7 ± 3.9	SiIV	12.30 ± 0.36
			AlIII	10.70 ± 0.21
9	2.76947	7.0 ± 2.6	SiIV	12.47 ± 0.18
			AlIII	11.85 ± 0.02

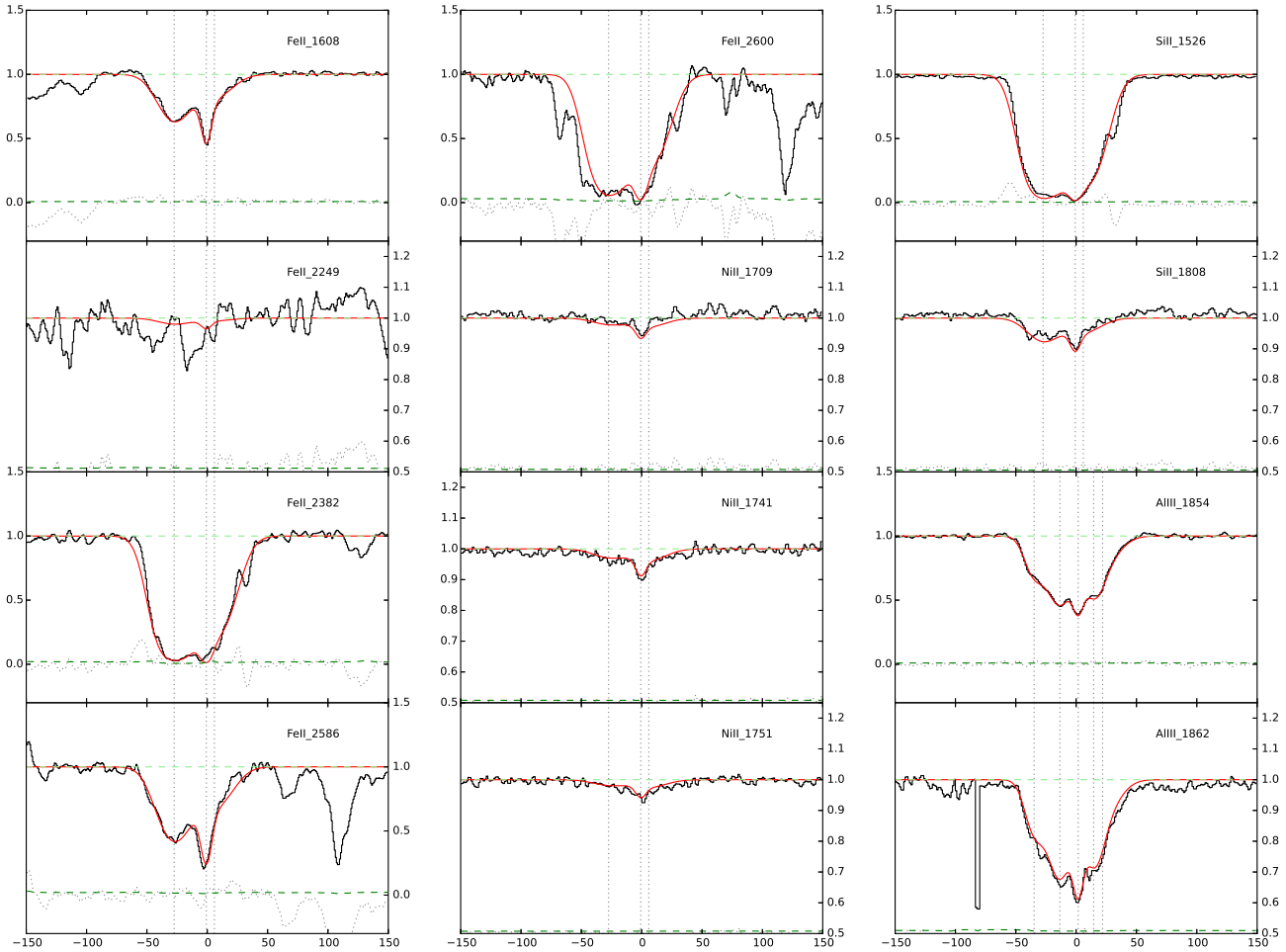

Figure C20. QSOB2126-15 z=2.769

C21 QSO LBQS2132-4321 $z_{em} = 2.42$, $z_{abs} = 1.916$, $\log N(HI) = 20.74 \pm 0.09$

This EUADP spectrum provides the coverage of many ions associated to the absorber, often free from blending and with a good SNR. The low-ionization ions detected are SiII $\lambda\lambda\lambda\lambda\lambda\lambda\lambda$ 1190 1304 1808 1253 1250 1260 1193, FeII $\lambda\lambda\lambda$ 1608 2260 2249, CrII λ 2056, NiII $\lambda\lambda$ 1741 1709, ZnII λ 2026 and SII $\lambda\lambda$ 1250 and 1253. The profile presents two distinct groups of components spread over about 300 km/s: the weak components, only detected in large oscillator strength ions and the strong components, detected in all low-ionization ions and saturated otherwise. Therefore, the column densities of the strongest components are measured from the small oscillator strength ions only. We fit SiII λ 1808, FeII λ 2260, CrII $\lambda\lambda$ 2056 2026, NiII $\lambda\lambda$ 1741 1709 and ZnII λ 2026 with four components. The intermediate ion AlIII λ 1854 which presents the same components (among others) is added to the fit. The remaining weak group is fitted with 3 components for SiII, AlIII and FeII. In this latter fit, some parameters such as the Doppler-parameter are fixed during the process because of a rather low SNR and/or blending. We detected a contamination in the third component of SiII λ 1808, based on SiII $\lambda\lambda$ 1526 and 1304, we therefore fitted the first three red components fixing the doppler parameter and column density of the third component of SiII. The fit results in the following column densities: $\log N(SiII) = 15.75 \pm 0.02$, $\log N(FeII) = 15.06 \pm 0.04$, $\log N(CrII) = 13.38 \pm 0.03$, $\log N(NiII) = 13.80 \pm 0.03$, $\log N(ZnII) = 12.69 \pm 0.02$ and $\log N(AlIII) = 13.18 \pm 0.03$. For SII $\lambda\lambda$ 1250 and 1253, a blend in the blue part of the absorption prevent from fitting the full profile. However, a lower limit is derived from the fit of the strong component in the red based on the other elements. The resulting column density is $\log N(SII) > 14.90$.

The spectrum cover several high-ionization ions: CIV $\lambda\lambda$ 1550, 1548 and SiIV $\lambda\lambda$ 1393 and 1402. However, no satisfactory fit could be found for the CIV doublet because of the low SNR in this portion of the spectrum. On the contrary, a 4-component profile is derived for the SiIV λ 1402. It is also interesting to note that the velocity components are quite similar to the low-ionization ions components. The SiIV λ 1393 line suffers from a blend and again a limited SNR, so that the fit is performed with fix parameters but for the second Doppler-parameter. This fit results in $\log N(SiIV) = 14.2 \pm 0.01$.

The parameter fits of the individual components are listed in Table C21 and the corresponding Voigt profile fits are shown in Fig. C21.

Table C21. Voigt profile fit parameters to the low- and high-ionization species for the z_{abs}=1.916 log N(H I)=20.74 ± 0.09 absorber towards QSO LBQS 2132-432.

Comp.	z_{abs}	b km s^{-1}	Ion	log N cm^{-2}
1	1.91433	15.60 ± 1.2	SiII	14.82 ± 0.04
			FeII	14.42 ± 0.06
			CrII	12.63 ± 0.05
			NiII	13.04 ± 0.08
			ZnII	11.43 ± 0.17
			AlIII	12.77 ± 0.02
2	1.91454	8.9 ± 0.4	SiII	15.03 ± 0.02
			FeII	14.57 ± 0.03
			CrII	12.81 ± 0.03
			NiII	13.30 ± 0.03
			ZnII	12.15 ± 0.03
			AlIII	12.58 ± 0.02
3	1.91478	7.00	SiII	14.80
			FeII	14.22 ± 0.06
			CrII	12.69 ± 0.03
			NiII	13.05 ± 0.05
			ZnII	12.00 ± 0.04
			AlIII	12.48 ± 0.02
4	1.91562	6.0	SiII	13.74 ± 0.02
			FeII	12.40 ± 0.32
			CrII	–
			NiII	–
			ZnII	–
			AlIII	12.15 ± 0.03
5	1.91585	7.0	SiII	13.9 ± 0.02
			FeII	13.26 ± 0.05
			CrII	–
			NiII	–
			ZnII	–
			AlIII	12.29 ± 0.03
6	1.91599	3.0	SiII	13.07 ± 0.06
			FeII	12.52 ± 0.22
			CrII	–
			NiII	–
			ZnII	–
			AlIII	11.60 ± 0.10
7	1.91647	5.2 ± 0.3	SiII	15.01 ± 0.02
			FeII	14.41 ± 0.05
			CrII	12.74 ± 0.04
			NiII	13.21 ± 0.04
			ZnII	12.28 ± 0.02
			AlIII	12.19 ± 0.03
1	1.91431	17.8 ± 0.3	SiV	13.90 ± 0.01
2	1.91474	16.5 ± 0.5	SiV	13.46 ± 0.01
3	1.91567	11.1 ± 0.8	SiV	13.40 ± 0.07
4	1.91582	19.4 ± 1.1	SiV	13.40 ± 0.05

C22 QSO B2318-1107 $z_{em} = 2.96$, $z_{abs} = 1.629$, $\log N(HI) = 20.52 \pm 0.14$

A broad variety of ions are covered in the EUADP spectrum of this low-redshift absorber. The low-ionization ions detected are FeII $\lambda\lambda\lambda$ 2260, 2249 2374, MnII λ 2576, AlII λ 1670, CII λ 1334, SiII $\lambda\lambda\lambda$ 1260, 1304 and 1526. The profile of the CII line appears to be saturated and blended from a comparison with other low-ionisation ions. This line is therefore not considered for a fit. Likewise, the SiII lines are saturated and are not fitted. The AlII λ 1670 line appears to be blended (strong absorption on the blue side of the line), and therefore only an upper limit is available: $\log N(AlII) < 14.93$. FeII and MnII are well fitted with 2 components (from the asymmetry of FeII λ 2249): resulting in $\log N(FeII) = 14.14 \pm 0.02$ and $\log N(MnII) = 11.78 \pm 0.04$. Also, we derive upper limits from non detection of SII λ 1250, $\log N(SII) < 14.54$, CrII λ 2062, $\log N(CrII) < 12.47$, ZnII λ 2026, $\log N(ZnII) < 11.74$, MgI λ 2026 and $\log N(MgI) < 12.37$.

The detected intermediate-ionization transitions are AlIII $\lambda\lambda$ 1854 and 1862. The absorption profiles differ significantly from the high- or the low-ionization ions (red component stronger than the blue one). The fit is thus performed

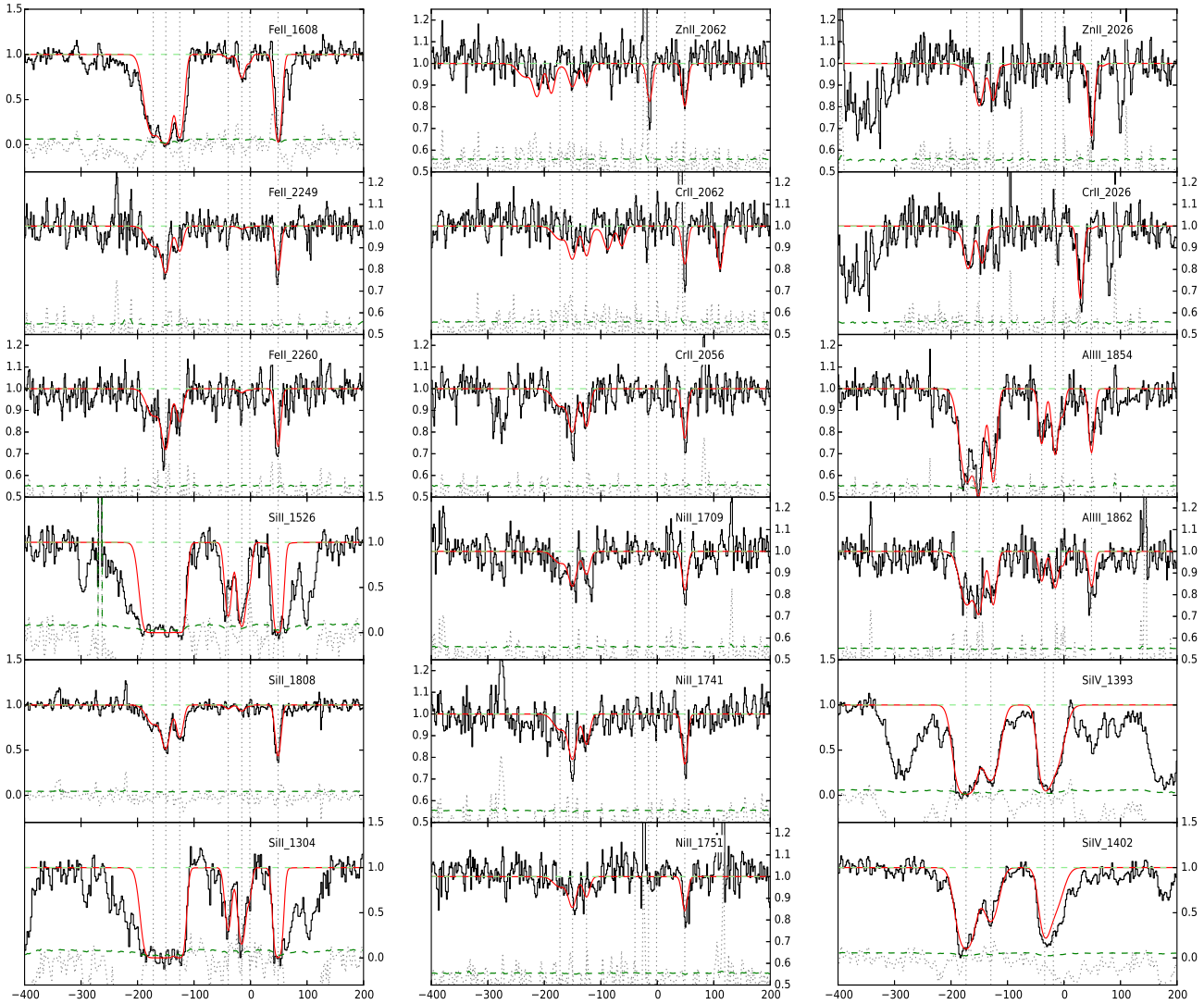

Figure C21. QSOLBQS2132-4321

separately with two components. The resulting column density is $\log \mathrm{N(AlIII)} = 12.17 \pm 0.02$.

The high-ionization ions detected are SiIV $\lambda\lambda$ 1393, 1402 and CIV $\lambda\lambda$ 1548 (saturated) and 1550. The position of the SiIV lines (on the red wing of the Lya absorber for λ 1393 and blended from the forest for λ 1402) prevents a robust fit for the SiIV lines. Similarly to the low-ionization ions, the asymmetry of CIV λ 1550 suggests a 2-component profile. We derive an upper limit for CIV from a 2-component fit of CIV λ 1550, as the saturated CIV λ 1548 brings no constraints on possible contamination of CIV λ 1550. We obtain $\log \mathrm{N(CIV)} < 14.10$.

The parameter fits of the individual components are listed in Table C22 and the corresponding Voigt profile fits are shown in Fig. C22.

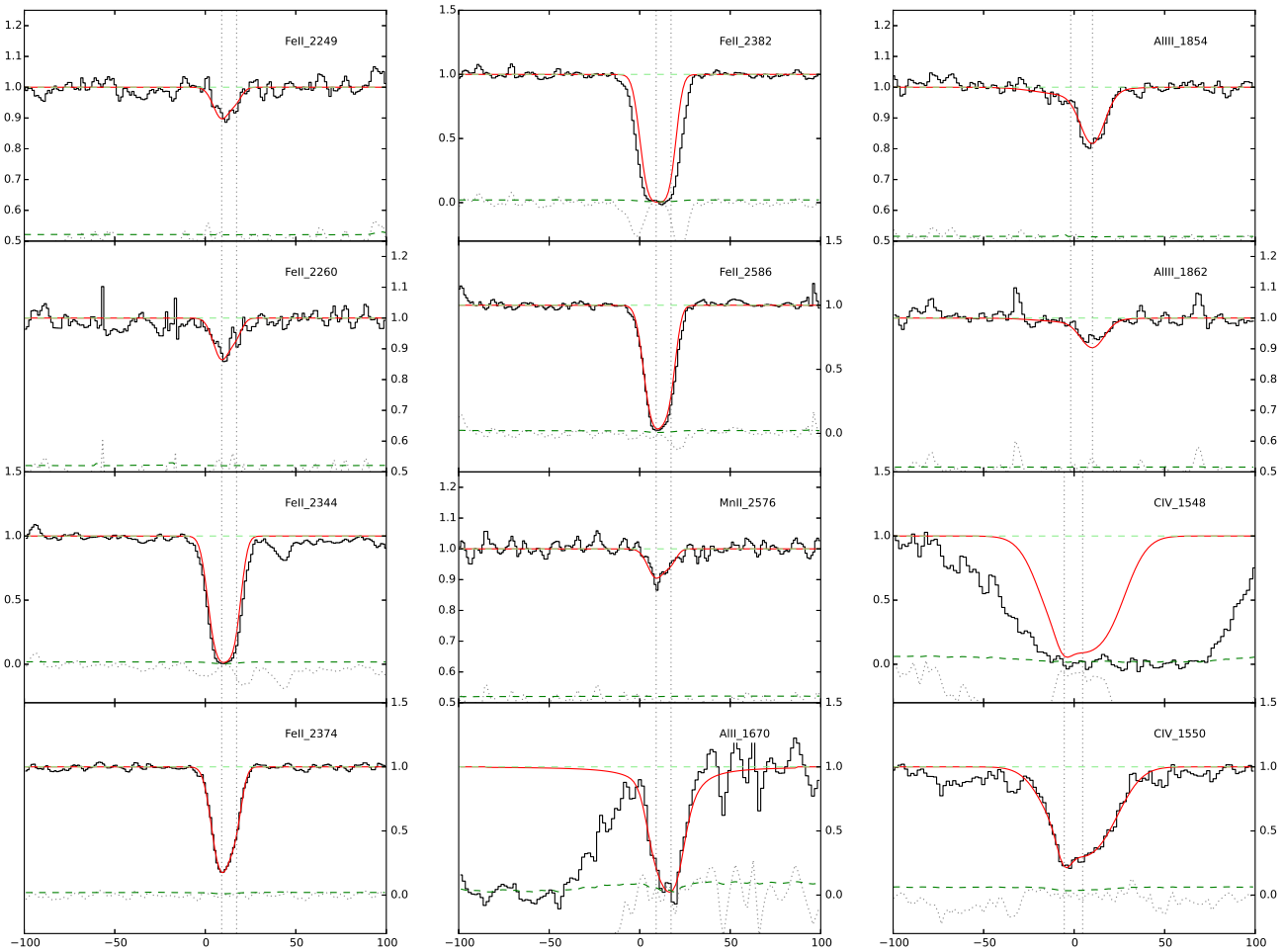

Figure C22. QSOB2318-1107

Table C22. Voigt profile fit parameters to the low- and high-ionization species for the z_{abs}=1.629 log N(H I)=20.52 ± 0.14 absorber towards QSO B2318-1107.

Comp.	z_{abs}	b km s^{-1}	Ion	log N cm^{-2}
1	1.62908	4.7 ± 0.3	FeII	14.05 ± 0.01
			MnII	11.67 ± 0.04
			AlII	12.06 ± 0.10
2	1.62915	1.4 ± 0.4	FeII	13.42 ± 0.08
			MnII	11.13 ± 0.12
			AlII	14.93 ± 0.40
1	1.62898	24.2 ± 15.0	AlIII	11.60 ± 0.35
2	1.62909	8.0 ± 1.4	AlIII	12.03 ± 0.11
1	1.62895	2.7 ± 3.2	CIV	13.21 ± 0.17
2	1.62904	19.8 ± 1.1	CIV	14.04 ± 0.03